Design and test of an apparatus for measuring the thermoelectric figure of merit ZT of solids

Dissertation

zur Erlangung des Doktorgrades
der Naturwissenschaften
(Dr. rer. nat.)

vorgelegt von

M.Sc. Florian Gather

Mai 2015

Betreuer:
Prof. Dr. P. J. Klar

Contents

Abstract **7**

Zusammenfassung **9**

1 Introduction **11**

2 Theoretical background **13**

2.1 Introduction to thermoelectrics 13

2.1.1 Historical background 13

2.1.2 Seebeck effect 16

2.1.3 Temperature measurements using thermocouples 16

2.1.4 Optimizing thermoelectric materials: figure of merit ZT . . . 17

2.2 Heat transport 19

2.2.1 Historical background 19

2.2.2 Heat conduction 20

2.2.3 Heat radiation 22

2.3 Methods for determining thermal conductivities 22

2.3.1 Steady-state methods 22

2.3.2 Transient methods 23

3 Low temperature *ZT*-meter **31**

3.1 Concept 31

3.2 Measurement set-up 34

3.3 Thermopower measurements 37

3.4 Thermal conductivity measurements 39

3.5 Transient heat conduction 42

3.5.1 Implementation of interface resistances between sample and sensors . . . 48
3.5.2 Implementation of heat radiation . . . 49
3.5.3 Uncertainty analysis . . . 50
3.5.4 Implementation of the model . . . 51
3.6 Testing of the model using Comsol Finite Element simulations . . . 52
3.6.1 Round-off, truncation, and interpolation error . . . 53
3.6.2 Influence of the pseudo-random number generator on the Monte-Carlo simulations . . . 54
3.6.3 Interpretation of the Monte-Carlo results . . . 54
3.6.4 Measurement duration, sampling rate and informative value . 58
3.6.5 Periodic heating . . . 61
3.6.6 Effect of the thermal properties of the sample on the measurement uncertainties . . . 71
3.6.7 Reduction of the temperature noise at the simulation boundaries 73
3.6.8 Considerations on the sample geometry . . . 74
3.6.9 Effect of heat radiation on the measurement . . . 77
3.6.10 Influence of the thermal contact resistance on the measurement 78
3.6.11 Transient measurements over large temperature ranges . . . 80

4 Calibration and first measurements 85
4.1 Thermocouples . . . 85
4.2 Heat flux sensors . . . 87
4.3 Seebeck coefficients of the measurement wires . . . 88
4.4 Measurements of the electric conductivity . . . 91
4.5 First κ measurements on glass samples . . . 92
4.5.1 Transient measurements . . . 95
4.6 Measurements on a BiSb sample . . . 97
4.7 Measurements on a POM sample . . . 97
4.8 Sources of measurement error . . . 99
4.8.1 Estimation of the error limits for selected error sources . . . 104
4.8.2 Strategies to enhance the measurement accuracy of the ZT-meter . . . 105

5 Conclusions 107

Bibliography **108**

Appendix **115**

A Solution of the heat equation for oscillating boundary conditions . . 115

B Parameters used in the numerical simulations 118

Danksagung **121**

Abstract

The aim of this work was the design and test of an apparatus for the measurement of the thermoelectric figure of merit ZT of solids. The thermal and the electric conductivity as well as the determination of the Seebeck coefficient of cylindrical bulk-samples can be determined using a newly designed and built set-up. Measurements of the different quantities are performed simultaneously to prevent deviations due to sample degradation during several temperature cycles. The focus is on the measurement of the thermal conductivity. Two different steady-state methods and one transient measurement method are used to determine the thermal conductivity. The first steady-state method is a comparative approach, where the heat flux through the sample is measured using sensors built from a known material. The second steady-state method is an absolute method, where the heat flux is determined from the electric power of the heater generating the heat flux. Since those measurement approaches show long measurement durations a transient method was developed and implemented. Here, the temperatures measured inside the set-up are fitted to a numerical model and then the thermal conductivity and the thermal diffusivity of the sample extracted from the fit. Since a numerical model was implemented the heater power can be an arbitrary function of time. The main benefit of the transient approach is the much higher measurement speed, since the waiting periods where the steady-state is approached are omitted. By increasing the base temperature of the set-up continuously a sample can be characterized quickly over a wide temperature range. The transient measurement method has been investigated further using Monte-Carlo simulations. With those simulations conclusions about the influence of certain measurement parameters like the heater waveform or measurement durations on the informative value of the measurement itself can be drawn. Furthermore, the effect of e.g. the sample geometry or heat radiation has been analyzed. First experimental results of the set-up confirm that the transient mode is working properly. Test samples have been investigated with the different modes of the set-up as well as with other set-ups and the results are found to agree within the error limits of the set-up. Also, the measurements of the Seebeck coefficient are working properly. However, the determination of the electric conductivity of the sample has to be revised, since the contact resistance to the electrical leads is too large, especially in combination with well conducting samples. Further sources of measurement error inside the set-up have been investigated and quantified. Different improvements of the set-up have been suggested for the future.

Zusammenfassung

Ziel dieser Arbeit war der Entwurf und die Umsetzung eines experimentellen Aufbaus zur Messung der thermoelektrischen Eigenschaften von Festkörpern. Dieser Aufbau ermöglicht es, die thermische und die elektrische Leitfähigkeit sowie den Seebeckkoeffizienten von zylindrischen Proben zu messen und somit deren thermoelektrische Gütezahl ZT zu bestimmen. Dies geschieht im gleichen Messzyklus, um Verfälschungen der Messergebnisse durch Veränderungen an der Probe nach mehreren Temperaturzyklen auszuschließen. Der Fokus in dieser Arbeit liegt auf der Messung der thermischen Leitfähigkeit. Diese kann sowohl mit zwei stationären Methoden als auch mit einem neuen transienten Verfahren bestimmt werden. Als stationäre Methoden dienen hierbei ein Vergleichsverfahren, bei dem der Wärmefluss durch die Probe mittels eines bekannten Materials bestimmt wird, und eine absolute Messung, bei der der Wärmefluss aus der elektrischen Leistung eines Heizers ermittelt wird. Da diese Messverfahren lange Messdauern erfordern, wurde zusätzlich eine transiente Methode entwickelt und implementiert. Hierbei werden die gemessenen Temperaturen innerhalb des Aufbaus an ein numerisches Modell angepasst und so die Wärmeleitfähigkeit sowie die Wärmekapazität der Probe bestimmt. Durch die Implementierung des eindimensionalen numerischen Modells können beliebige Signalformen für die Heizleistung vorgegeben werden. Der Vorteil des transienten Verfahrens gegenüber den stationären Methoden ist eine deutlich geringere Messdauer, insbesondere da das Warten auf den stationären Zustand nicht nötig ist. Durch kontinuierliches Erhöhen der Grundtemperatur des Aufbaus kann die Probe daher über größere Temperaturbereiche hinweg schnell charakterisiert werden.

Das transiente Messverfahren wurde weiterhin mittels Monte-Carlo-Simulationen untersucht. Diese ermöglichen es, Schlüsse über den Einfluss verschiedener Messparameter wie Heiz-Signalformen, Messraten oder Messdauern auf die Genauigkeit der Messung zu ziehen. Außerdem wurde der Einfluss der Probengeometrie und von Wärmestrahlung auf die Messergebnisse analysiert.

Erste experimentelle Ergebnisse zeigen, dass die transiente Messmethode funktioniert. Testproben wurden mit dem Aufbau und mit alternativen Verfahren untersucht und die Ergebnisse verglichen, wobei Übereinstimmungen innerhalb der Messtoleranzen gefunden wurden. Auch Messungen des Seebeckkoeffizienten waren erfolgreich. Bei den Untersuchungen des elektrischen Widerstands hingegen wurde festgestellt, dass, insbesondere bei gut leitenden Proben, der Kontaktwiderstand

zwischen Sensor und Probe zu hoch ist. Daher muss das Messverfahren für diese Größe überarbeitet werden. Weitere Quellen für Messfehler wurden untersucht, ihr Einfluss abgeschätzt und darauf aufbauend mögliche Verbesserungen an dem Aufbau vorgeschlagen.

1 Introduction

The term thermoelectrics covers a number of effects, linking the fields of electricity and heat. The most commonly known thermoelectric effects are the Seebeck effect and the Peltier effect, allowing for a direct conversion of a heat flux into an electric current and vice versa. Both effects are interesting for many applications like energy recovery from waste heat or electric power generation for spacecraft far away from the sun. The energy conversion in thermoelectric devices is done without moving parts, which makes it attractive for use in rough environments like space or in the automotive sector. Thermoelectric cooling is contemplated for use in electric cars for passenger acclimatization, since here the engine does not produce enough heat for this purpose. Small Peltier elements in the seats could pump heat from or to the passenger, which in case of the heating is even more efficient than Joule heating. Another field in which thermoelectric generators are already used is energy harvesting for sensor networks in remote locations.

However, despite their many advantages, the efficiency of thermoelectric devices is still too low for an application on a large scale outside their niches. Different strategies, like nano-structuring, doping or the introduction of scattering centres, have been used to improve the performance of the materials. A parameter determining the efficiency of a material is the thermoelectric figure of merit $ZT = S^2\sigma\kappa^{-1}$, where S is the Seebeck coefficient, σ is the electric conductivity and κ is the thermal conductivity. Numerous methods exist to determine these material properties for samples of different geometries and phases, e.g. solids, liquids or powders. However, in most cases, the parameters for ZT are determined in individual set-ups, so the samples have to endure several temperature cycles without showing ageing effects. Also, the different set-ups may have different requirements with respect to sample geometry and the sample needs to be reshaped e.g. by cutting or adding a new set of contacts. Sometimes even different samples have to be used to measure the different thermoelectric quantities determining ZT, further reducing the conclusiveness of the measurements.

The aim of this work was to develop a measurement system, which is able to simultaneously measure all properties of bulk samples determining their thermoelectric efficiency. The focus was on the determination of the thermal conductivity, as the measurement methods for this parameter are most sensitive to the sample geometry. Many of the commonly used transient measurements are not applicable for thick

samples. Thus, two steady-state methods have been combined in the set-up. Additionally, a transient measurement method, similar to the Ångström method, has been developed and implemented. This transient approach not only allows one a faster measurement of the thermal conductivity of the sample, but also enables one to determine its thermal heat capacity. The numerical model, required for the evaluation of the transient method, has also been used to investigate the optimum measurement conditions with respect to accuracy and measurement duration.

This work is structured as follows: chapter 2 contains the theoretical background of the thermoelectric effects and heat transport. Also, historical outlines on the two subjects are given. In chapter 3 the concept of the low temperature ZT-meter is shown and explained in detail. Additionally, the numerical model, needed for the evaluation of the transient measurement mode is derived and evaluated. In chapter 4 the results from the calibration and test measurements are shown and discussed. In addition, the error sources for the measurements are identified and improvement strategies, which may be implemented in the future, are shown.

2 Theoretical background

2.1 Introduction to thermoelectrics

2.1.1 Historical background

Inspired by Christian Ørsted's discovery of the magnetic effects of electric currents in 1820, Johann Seebeck started to carry out his own investigations on this subject. Eventually he found the first thermoelectric effect to be discovered, the now called Seebeck effect. It was observed for the first time around the year 1821 [1, 2] and explained by Seebeck as magnetic polarization due to a thermal current. Seebeck joined pieces of two different metals to form a closed ring and observed the magnetic field beneath them during the heating or cooling of the junctions. He also ranked several metals according to the strength of this thermoelectric effect, thus defining the thermoelectric potential series. Seebeck also observed that the field strengths were larger for greater temperature differences. In 1823 Ørsted explained the Seebeck effect as an electric current driven by the temperature difference. This current in turn caused the magnetic field [3]. Accordingly, Ørsted named it thermoelectric instead of thermomagnetic which in turn was heavily disputed by Seebeck.

The first thermopiles, a number of thermoelectric elements electrically connected in series, were built, investigated and compared to galvanic cells by Joseph Fourier and Ørsted in 1823 [4]. Examples of the material arrangements they used are depicted in figure 2.1a. Those thermogenerators showed a much smaller voltage compared to galvanic cells but a comparable short-circuit current. They also were found to be more stable when short-circuited. Thus, they were used by Georg Ohm in his torsion balance experiment to investigate the relationship between electric resistance, current, and voltage [5]. In Ohm's torsion balance a piece of bismuth (a-b-b'-a') and copper stripes (a-d) (a'-d) in addition to the sample under investigation formed the electric circuit (see figure 2.1b). The junctions (a) and (a') between copper and bismuth were being cooled by ice and heated by boiling water, respectively. This equipment enabled Ohm to conduct his investigations under stable voltage conditions.

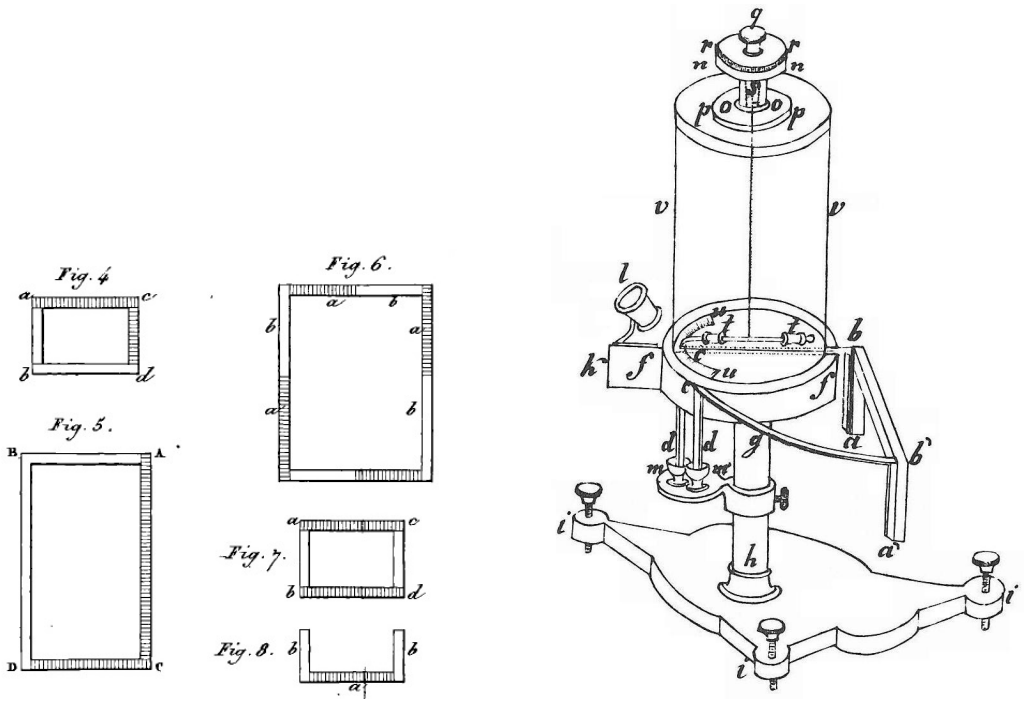

(a) (b)

Figure 2.1: (a) Experimental set-ups of Fourier and Ørsted to connect multiple thermoelectric junctions in series (from [4]) and (b) Ohm's torsion balance using a thermoelectric generator (a-b-b'-a') as source of electricity (from [5]).

In 1826 Antoine César Becquerel was the first to use the thermoelectric effect for temperature measurements using a platinum-palladium thermocouple [6]. This material combination is in use until today, and is known for its high temperature stability. With this set-up he was able to estimate the combustion temperature of an ethanol flame. By using this new method of temperature measurement Jean-Charles Peltier could investigate the influence of electric currents on the temperatures of a junction of two dissimilar metals. He published this discovery of the now called Peltier effect in 1834. This finding was amended four years later by Emil Lenz who discovered that heat absorption and production are proportional to the electric current. With his experiments on freezing water and melting ice he was able to explain the Peltier effect correctly [7].

James Prescott Joule discovered the effect of resistive heating and formulated in the now called Joule's first law [8]: the resistive heating of a conductor is proportional to the electric current squared times the conductor's resistance. However, at this time he stated that his findings were somewhat contradictory to the effect found by Peltier since cooling could not be explained by his law. This shows that Joule interpreted the Peltier effect not as transport of heat but rather heat creation as a result of an electric current.

At an annual meeting in 1847 William Thomson, later known as Lord Kelvin, learned about Joule's discovery regarding the conversion of mechanical work into heat, which was not compatible with the established caloric theory describing heat as a substance. Eventually Thomson began his work on the subject and developed the mechanical heat theory. In addition, he found relationships between the thermodynamically linked quantities Seebeck coefficient and Peltier coefficient: the so called Thomson or Kelvin relations. In 1929 these relations were generalised by Lars Onsager, who was awarded the Nobel Prize for this work. As a result of his thermodynamic investigations Thomson predicted and measured the Thomson effect as a third thermoelectric effect [9].

In 1851, Gustav Magnus, a German physicist, investigated the influence of the hardness of a metal wire on the magnitude of the thermoelectric effect and also presumed an influence of the surface oxidation. He thereby found that the thermovoltage is independent of the exact temperature distribution along the wire, but rather depends on the total temperature difference only, which is a prerequisite for the reliable use of thermocouples as temperature sensors [10].

The first to calculate the efficiency of thermoelectric devices was Edmund Altenkirch, who determined the efficiency of thermogenerators in 1909 [11] and of Peltier cooling devices in 1911 [12], and thus established the thermoelectric figure of merit ZT [13]. It is used for the classification of a material's suitability for thermoelectric applications. Since 1949 the Russian physicist Abram Ioffe began his scientific work in the area of thermoelectrics and used ZT to find efficient materials [14]. He developed a modern theory of thermoelectrics and promoted the use of semiconductors, considering them to be best suited for applications. Ioffe found proof that alloying may increase the thermoelectric performance by reducing the thermal lattice conductivity [15]. In the Western Hemisphere Julian Goldsmid used a material factor, the thermoelectric quality factor, which depends on the material's mobility, effective mass and thermal lattice conductivity. It enables an estimation of a semiconductor's potential for high ZT values without optimizing its carrier concentration [16]. He thereby predicted high figures of merit for semiconductors with a high effective mass, a high carrier mobility and a low thermal lattice conductivity.

At that time the first radioisotope thermal generators (RTGs) were used to provide power for spacecraft without employing moving parts or solar cells. The latter is especially important for missions far away from the sun where the power density of solar light is not sufficient to power the spacecraft's instruments by photovoltaics. Space exploration is one of the first niches where thermoelectric generators, despite their somewhat poor efficiency compared to other electric power sources, were used. Further applications are silent refrigerators, small cooling devices, e.g. for lasers, remote power generation for sensors etc. In the early 1990's new strategies in material science based on employing nanotechnology raised hopes to create new materials with higher ZT values and thus to improve the efficiency of thermoelectric generators to such an extent that they become competitive in a wide range of applications. Lyndon Hicks and Mildred Dresselhaus published two theoretical articles

showing that reducing dimensionality will radically enhance ZT [17, 18]. The field of thermoelectrics, stalled in the past, was revived and has advanced since then.

2.1.2 Seebeck effect

In a conductive solid exposed to a temperature gradient an electric field will build up due to thermodiffusion of mobile charge carriers. The thermodiffusion is basically a result of the temperature dependent and, thus, spatially varying carrier velocities in the solid.

The Seebeck coefficient is a material parameter relating the temperature difference ΔT and the resulting voltage U between two ends of the material as a proportionality factor. It is defined as:

$$S(T) = -\lim_{\Delta T \to 0} \frac{U}{\Delta T} \tag{2.1}$$

A direct measurement of the Seebeck coefficient is not possible, since every wire used for the measurement of the thermovoltage is also subject to the Seebeck effect. However, the coefficients can be determined by indirect measurements using the Thomson effect and the Kelvin relations or by using superconducting materials, which exhibit Seebeck coefficients of practically zero.

2.1.3 Temperature measurements using thermocouples

The Seebeck effect is often utilized to measure temperature differences by using a thermocouple consisting of two materials with different Seebeck coefficients S_1 and S_2. T_1 denotes the temperature at the junction of the two materials and T_2 is the temperature at the measurement instrument. The measured voltage U is given by:

$$U = -\int_{T_1}^{T_2} \left[S_1(T) - S_2(T)\right] dT. \tag{2.2}$$

When absolute temperatures of a thermocouple's junction are to be measured, an additional temperature measurement at a reference point is required. At the reference point the wires of the couple are connected to two wires of the same material, ensuring that no additional thermovoltage between the two lines is being built up. This material preferably has a low Seebeck coefficient to reduce errors due to possible material impurities. At the reference point it has to be ensured that the temperature of all wires is equal. However, this can be difficult, since simultaneously the electric insulation has to be preserved. For standard thermocouple types the voltage $U(T_1)$ with a fixed temperature at the reference point, mostly at $T_2 = 0\,^{\circ}\mathrm{C}$, are tabulated and can be used to obtain the junction temperature. Temperature measurements without a stable reference point can be evaluated by calculating:

$$T_1 = U^{-1}(U_{\text{measured}} + U(T_{\text{reference point}})). \tag{2.3}$$

Despite the higher effort necessary to establish a temperature measurement with thermocouples compared with the use of resistive techniques some advantages prevail. For one they can be used over a broad temperature range, which is superior to most resistive methods. Most important for the measurement method used here is the small thermal mass of the junction, leading only to short temporal delay and small alterations of the surrounding temperature distribution. Another advantage is the smaller volume of the sensor, thus, no temperature averaging effect will occur, possibly shifting the measurement results.

The disadvantages of thermocouples, next to the need for a reference-point, are potential inhomogeneities in their material composition, resulting in less accurate measurements if the corresponding device is not calibrated individually. Even by an individual calibration, this effect cannot be fully accounted for, since the thermovoltage of an inhomogeneous thermocouple depends on the exact temperature distribution along the wires. Furthermore, the handling is more complicated, since no contamination of the wires should occur and thus soldering is not always a good option. Very thin thermowires must not be bent too much, as strain on the wire may alter its Seebeck coefficient. In addition, most materials for thermocouples are prone to degradation due to ageing. Also, their thermovoltage can change during the lifetime of the thermocouple, making regular calibrations mandatory.

2.1.4 Optimizing thermoelectric materials: figure of merit ZT

The performance of a thermoelectric device is mainly determined by the dimensionless thermoelectric figure of merit, established by Altenkirch when he calculated the efficiency of thermogenerators and Peltier elements:

$$ZT = \frac{S^2\sigma}{\kappa}T. \tag{2.4}$$

Here σ is the electric conductivity and κ is the total thermal conductivity, which is the sum of the free carrier contribution κ_{carriers} and the lattice contribution κ_{lattice}. Additionally, the Wiedemann-Franz law states:

$$\frac{\kappa_{\text{carriers}}}{\sigma} = LT, \tag{2.5}$$

with L being the Lorenz number, a material constant. The Wiedemann-Franz law holds for materials with a band structure such that the Fermi surface is approximately a sphere. It is valid for many metals, and to a certain degree also for semiconductors.

As σ and κ_{carriers} cannot be changed independently from another, there are mainly two different routes for the optimization of ZT for different materials. The first

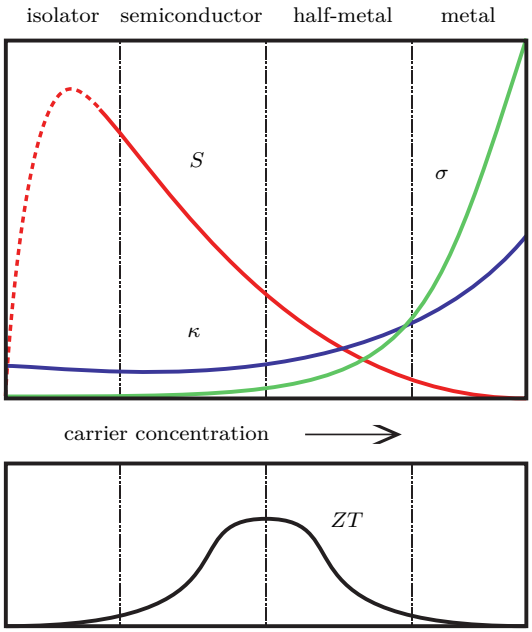

Figure 2.2: The thermoelectric material properties S, σ and κ, as well as the according ZT, plotted against the carrier concentration. For many material systems the largest ZT values are settled around the semiconductor half-metal transition (figure adapted by author from [19]).

one is to decrease κ_{lattice}, e.g. by alloying or introducing scattering centres. The second strategy, which is considered to be mostly independent from the first one, is to influence the material's electronic properties, e.g. by adjusting the carrier concentration or the dopant material. Nanostructuring can be used to improve materials even further by reducing the dimensionality, amplifying surface effects or introducing additional thermal boundaries. However, by adding new thermal boundaries the electronic properties might also be changed such that the overall ZT is not improved. The interplay between the different thermoelectric quantities is illustrated exemplarily for varying carrier concentration in figure 2.2.

When testing the success of a material's optimization, it is important to account for the transport direction as the thermoelectric material properties might be anisotropic. For example, wire-like nanostructures may be aligned within a composite material, resulting in largely different properties for different spatial directions. Thus, it must be ensured that all thermoelectric properties are measured in the same transport direction to yield a consistent interpretation of the data.

2.2 Heat transport

2.2.1 Historical background

With the beginning of the 18th century the phenomenon of heat conduction was more and more investigated. In 1701 Isaac Newton anonymously published his experiments about heat [20]. From these experiments especially Newton's cooling law, a solution of the heat equation, became publicly known. In 1750 Georg Wilhelm Richmann conducted an experiment where he compared the heat conductivity of different metal bars by heating the bars on one side and measuring the temperature on the other side [21]. Johann Heinrich Lambert also investigated heat phenomena on a metal bar by heating a bar on one side and measuring the temperatures on different positions along the bar. He found that the temperature decreases logarithmically with the distance from the heat source, which is correct when the phenomenon of convection is considered [22]. Inspired by Benjamin Franklin, Jan Ingenhousz published the results of his experiments in 1789. He heated different wax-coated metal bars on one side and observed the positions where a phase transition of the wax occurred, as well as the speed of the melting process [23]. However, only a ranking of the heat conductivities of the metals could be derived with these experiments and the phenomenon of heat conduction could still not be quantified.

A first mathematical description of the problem was published by Jean-Baptiste Biot in 1804 [24]. Based on the findings from Newton's cooling law Biot derived a differential equation, which is identical to the one-dimensional heat equation. He also successfully conducted experiments to test his formula. However, Biot was not able to explain external heat effects, such as convection and heat radiation with his model. Joseph Fourier published his first works on the subject in 1807 [25]. He continued his work on heat conduction and published his 'Théorie analytique de la chaleur' in 1822, in which he presented a general method of solving the heat equation for different boundary conditions [26]. Fourier's law, describing the heat transport in the steady state, is also formulated in this publication.

Until then thermal conductivities could only be measured in relation to one another. In his book Fourier suggested three different approaches to determine absolute thermal conductivities. The first was implemented by Jean Claude Péclet around 1841, by measuring the temperature profile along a metal bar mounted between an ice block and a steam container [27]. He approximated the amount of heat flowing through the bar by determining the quantities of condensed steam and melted ice. This approach turned out to be very imprecise and other methods had to be found.

The next method, proposed and also previously implemented by Fourier, was to combine the experiment performed by Lambert with an additional cooling experiment to cancel out convection effects. A corresponding experiment was conducted by James David Forbes and the results were published in 1862 [28]. In contrast to Fourier he used graphical evaluation methods to fit the cooling function as well as

the temperature distribution to the measurement data. With this experiment Forbes was able to show that the thermal conductivity of iron is temperature dependent.

Fourier's third idea for the determination of absolute thermal conductivities employed a sinusoidal heating as a boundary condition on one side of the sample. By solving the heat equation for this boundary condition one is able to determine the thermal diffusivity and, with an additional measurement of the heat capacity, the thermal conductivity. Fourier himself performed first measurements using this method, which were widely unknown to the scientific community. In 1860, William Thomson, later known as Lord Kelvin, published values of the thermal conductivities of different soil types calculated from measurements of Forbes [29, 30]. Here the periodic heat source was the seasonal change of the atmosphere temperature. The soil temperatures were measured at different times, depths and locations. By analyzing the decrease of the temperature amplitudes and the phase shifts at different positions he could deduce the thermal diffusivity. A similar approach had been used by Anders Jonas Ångström in 1861 to obtain the thermal diffusivities of different metals [31, 32]. In contrast to Thomson he did allow for general periodic functions as boundary conditions and used a more or less rectangular heat input realized by alternating application of steam and ice water at one of the boundaries of the sample. His experimental results turned out to be the most accurate values of thermal conductivities until then.

Subsequently, numerous experiments were published, all following the designs which were previously proposed by Fourier differing only in minor details. One significant improvement, however, was made by Charles Lees in 1898 when he used an electric heater as a heat source and therefore could measure the heat flux directly [33]. This steady-state method was further improved by Richard Poensgen in the year 1912 by adding a heated guard ring and thus eliminating heat losses in the lateral direction. Revised versions of these hot-plate methods are still being used for the characterization of insulation materials. In the following years the different measurement methods were improved for different sample geometries, sizes and parameters. New heat sources like laser- or xenon-light as well as lock-in techniques and new data logging methods enabled more sophisticated transient measurement approaches. The most important ones will be discussed in one of the next sections.

2.2.2 Heat conduction

In the following the one-dimensional heat equation for nonisotropic solids will be derived from Fourier's law and the principle of conservation of heat. The derivation is based on a deduction for isotropic materials found in Ref. 34. The differential form of Fourier's law states that the heat flux density $\dot{q}$ is equal to the negative product of the temperature gradient $\frac{\partial T}{\partial x}$ and the thermal conductivity κ:

$$\dot{q} = -\kappa\left(x\right)\frac{\partial T}{\partial x}. \tag{2.6}$$

Also, the energy density ΔQ required to heat a solid with the specific heat capacity c and the mass density ρ is given as:

$$\Delta Q = c\,(x)\,\rho\,(x)\,\Delta T. \tag{2.7}$$

In the region $x - \Delta x \leq \chi \leq x + \Delta x$ during $t - \Delta t \leq \tau \leq t + \Delta t$ a temperature change of $\Delta T = T\,(\chi, t + \Delta t) - T\,(\chi, t - \Delta t)$ leads, by integration of Eq. (2.7), to the change in internal energy:

$$\Delta Q = \int_{x-\Delta x}^{x+\Delta x} c\,(\chi)\,\rho\,(\chi)\,[T\,(\chi, t + \Delta t) - T\,(\chi, t - \Delta t)]\,d\chi \tag{2.8}$$

$$= \int_{t-\Delta t}^{t+\Delta t} \int_{x-\Delta x}^{x+\Delta x} c\,(\chi)\,\rho\,(\chi)\,\frac{\partial T}{\partial \tau} d\chi d\tau. \tag{2.9}$$

For Eq. (2.9) the fundamental theorem of calculus was used. Without heat sinks or heat sources inside the space region itself, the change of heat is only caused by the conduction through the boundaries. This conduction follows Fourier's law given in Eq. (2.6):

$$\Delta Q = \int_{t-\Delta t}^{t+\Delta t} \left[\kappa\,(x + \Delta x)\,\frac{\partial T\,(x + \Delta x, \tau)}{\partial x} - \kappa\,(x - \Delta x)\,\frac{\partial T\,(x - \Delta x, \tau)}{\partial x}\right] d\tau \tag{2.10}$$

$$= \int_{t-\Delta t}^{t+\Delta t} \int_{x-\Delta x}^{x+\Delta x} \frac{\partial}{\partial \chi}\left[\kappa\,(\chi)\,\frac{\partial T}{\partial \chi}\right] d\chi d\tau, \tag{2.11}$$

where the fundamental theorem of calculus has been applied a second time. The consideration of the energy conservation leads to:

$$\int_{t-\Delta t}^{t+\Delta t} \int_{x-\Delta x}^{x+\Delta x} \left[c\,(\chi)\,\rho\,(\chi)\,\frac{\partial T}{\partial \tau} - \frac{\partial}{\partial \chi}\kappa\,(\chi)\,\frac{\partial T}{\partial \chi}\right] d\chi d\tau = 0. \tag{2.12}$$

Using the fundamental lemma of calculus of variations, one obtains the heat equation:

$$c\,(x)\,\rho\,(x)\,\frac{\partial T}{\partial t} - \frac{\partial}{\partial x}\kappa\,(x)\,\frac{\partial T}{\partial x} = 0. \tag{2.13}$$

This form of the heat equation will be used later in the numerical model, since here non-isotropic materials have to be considered. However, for isotropic materials the heat equation can be simplified to its more common form:

$$\frac{\partial T}{\partial t} = \frac{\kappa}{c\rho}\frac{\partial^2 T}{\partial x^2}. \tag{2.14}$$

The coefficient $D = \frac{\kappa(x)}{c(x)\rho(x)}$ is also known as thermal diffusivity.

2.2.3 Heat radiation

Heat is not only carried by the heat conduction mechanisms in solids, but can also be transported between two isolated solids by means of radiation. The power P being emitted by a surface of area A at temperature T to the ambient is given by the Stefan-Boltzmann law:

$$P = A\epsilon\Sigma T^4. \tag{2.15}$$

The parameter ϵ is the emissivity of the surface and Σ is the Stefan-Boltzmann constant. If the radiation exchange towards the ambient is perfect, and the heat emitted by the surface is absorbed totally by the environment, the radiative power between the surface and the ambient at temperature T_{ambient} is:

$$P = A\epsilon\Sigma\left(T^4 - T_{\text{ambient}}^4\right). \tag{2.16}$$

For the calculation of the heat transport between two surfaces with arbitrary orientation form factors have to be used, which describe the fraction of the radiation from one body reaching the other, taking into account the geometry of the problem. As specular surfaces must be treated differently than diffuse surfaces, and as most real surfaces have a mix of specular as well as diffuse properties, the exact description of heat radiation is difficult. Thus, in thermal conductivity measurements, in which heat radiation plays a substantial role as it constitutes one possible path of parasitic heat currents, it is recommended to minimize the heat radiation rather than trying to correct for it in the analysis of the data. However, especially at higher temperatures the minimization of radiation errors may become very complex.

2.3 Methods for determining thermal conductivities

2.3.1 Steady-state methods

The steady-state methods for measuring thermal conductivities may be divided into absolute and comparative methods. Both kinds make use of Fourier's law, Eq. (2.6), and in both the temperature gradient induced by a heat flux is measured. The methods differ in the way the heat flux is determined. In absolute methods the heat flux is obtained directly by measuring the power provided for the heat source or the power arriving at the heat sink respectively. The difficulty with this approach is to ensure that the whole heat is transported through the sample and not across electrical or mechanical connections of the measurement set-up. Furthermore, radiation, especially at the hot surfaces of a heater, might lead to measurement errors if no precautions are taken. One way of avoiding errors due to radiation and parasitic heat currents from the sample heater to the mechanical connections of the set-up is to use a guard heater. This is an additional heater set to the same temperature as

the sample heater. As both heaters are in thermal equilibrium, no heat conduction or radiation between the two of them occurs. Furthermore, radiation shields may reduce radiative parasitic heat transport from the sample to the environment by reflecting the radiated heat back to the sample surface.

In comparative methods materials with known thermal conductivities are inserted between heat source and sample and are used as heat flux sensors. The temperature gradients along the heat flux sensor and the sample are measured and the thermal conductivity can then be obtained using:

$$\kappa_{\text{sample}} = \left(\frac{\partial T}{\partial x}\right)_{\text{sensor}} \cdot \kappa_{\text{sensor}} \cdot \left(\frac{\partial T}{\partial x}\right)^{-1}_{\text{sample}}. \tag{2.17}$$

The effect of parasitic or radiative heat conduction from the sample to the environment may be estimated by using a heat flux sensor on each side of the sample. Without heat radiation both should yield the same heat flux. However, due to radiation and heat conduction over wires used for temperature measurements the heat flux through the sensors will differ and pose a lower and upper limit for the heat flux through the sample. In order to minimize these deviations heat shields may be used whose use is obligatory in absolute methods. Also, the wirings have to be thermally well connected to a point which has a temperature near the sample temperature.

2.3.2 Transient methods

A number of methods does not use the steady-state heat equation (Eq. (2.6)), but instead the general heat equation (Eq. (2.13)). In such a transient thermal conductivity measurement technique the sample is thermally excited and its temperature is recorded time-dependently. Using a physical model this information is then converted into physical values of thermal conductivity, heat capacity or thermal diffusivity. The advantage of such an approach is that it can be faster than most steady-state methods, as the steady state does not need to be approached and reached during the measurement. Also, the thermal excitation can be kept very small, leading only to small errors due to radiation and parasitic conduction. In addition, there may be fewer boundary conditions resulting in less complicated experimental designs and thus smaller errors. An example for this is the Ångström method, introduced by Ångström to determine the thermal conductivity of metal rods. His results turned out to be significantly more precise than those of previous experiments. One disadvantage of transient methods is that they often depend on complex models and require approximations or numerical evaluations, if no analytic solutions can be found, making implementations extensive and less accurate.

Since a large number of transient methods exists, only the most important ones will be discussed in detail in what follows.

Flash analysis

The flash method, also laser flash analysis, was proposed in 1961 by Parker et al. [35]. A light pulse heats the front-end of a bulk sample while the temperature of the backside is measured time-dependently. If the boundary conditions correspond to an adiabatic coupling of the sample to the environment, the thermal diffusivity D can be determined as follows:

$$D = 1.388 \cdot \frac{d^2}{\pi^2 t_{1/2}}, \tag{2.18}$$

where d is the sample thickness and $t_{1/2}$ is the time difference between the moment in time when the flash impinges on the sample and the moment in time when the temperature on the backside has reached half its maximum value ([35]). This formula does not account for radiation effects, surface convection or the finite lengths of heat pulses. These effects are taken into account by the more advanced Carpe-Lehman-model [36]. The flash analysis method has the advantage of being very fast compared to steady-state methods. However, often the samples have to be prepared using graphite to increase the optical absorption of the surface, sometimes leading to contamination effects in further measurements of other properties. Also, the mass density and the heat capacity of the samples must be known for the determination of the thermal conductivity and therefore additional measurement methods such as the differential scanning calorimetry have to be employed. This, however, may lead to additional uncertainties.

3ω-method

The 3ω-method was proposed by David Cahill and can be used to determine the thermal conductivity and the thermal diffusivity of bulk and thin-film samples [37–39]. Modifications also allow one to characterize nanowires or to spatially scan the thermal conductivity of surfaces [40, 41]. The original method uses a metal stripe which is attached atop the sample to act as heater and thermometer simultaneously. This stripe is heated with an alternating current of the frequency ω, leading to a temperature oscillation with the amplitude ΔT and frequency 2ω. The temperature amplitude strongly depends on the thermal properties of the sample as well as on the sample geometry. Since the heater resistance is temperature dependent, it is also subject to an oscillation of frequency 2ω. The modulation of the oscillations of the current and of the resistance leads to a small component of frequency 3ω that is directly related to ΔT. The frequency dependence of ΔT is then used to calculate the thermal properties of the sample employing an appropriate model. As only a single metal stripe is employed as thermometer and heater, the experimental conditions and the boundary conditions are simpler and less error-prone than those of other methods. Using small excitation amplitudes the radiation errors can be kept low and with lock-in techniques the signal acquisition is immune to offset voltages.

In Ref. 38 a model for the amplitude of the temperature oscillation ΔT of a heater on a semi-infinite substrate is presented. With $1/q = \sqrt{D/i2\omega}$ the temperature oscillation is given by:

$$\Delta T = \frac{P}{l\pi\kappa} \int_0^\infty \frac{\sin^2(kb)}{(kb)^2\sqrt{k^2+q^2}} dk. \tag{2.19}$$

Here b is the half heater width, P the heater power, l the heater length and κ the thermal conductivity of the sample. The absolute value of $1/q$ is a measure for the penetration depth of the thermal waves into the sample. The integral can only be evaluated analytically if the finite heater width is neglected and the out-of-phase information for the determination of D is discarded. Furthermore, the heat capacity of the heater is neglected in the model. To account for the heater's finite width, in this work, the integral is evaluated numerically. Additionally, the model has been adapted similarly to the approach described in Ref. 42, in order to take the heat capacity of the heater into account. The thermal impedance Z of the sample can be used to calculate ΔT according to:

$$\Delta T = Z \cdot P. \tag{2.20}$$

By adding the thermal capacitance of the heater in series to Z, the total impedance Z^* is given by:

$$Z^* = \left(\frac{1}{Z} + i2\omega 2bl\rho_\mathrm{h} c_\mathrm{h} d_\mathrm{h} \right)^{-1}, \tag{2.21}$$

where ρ_h, c_h, and d_h are the density, the heat capacity, and the thickness of the heater, respectively. An illustration of an electrical equivalent circuit is shown in figure 2.3. When, in order to improve the adhesion on the sample, two heater layers are used, a second capacitance can be added:

$$Z^* = \left(\frac{1}{Z} + i2\omega 2bl \left(\rho_{\mathrm{h}1} c_{\mathrm{h}1} d_{\mathrm{h}1} + \rho_{\mathrm{h}2} c_{\mathrm{h}2} d_{\mathrm{h}2} \right) \right)^{-1}. \tag{2.22}$$

The temperature amplitude for a one-layer heater is then obtained using:

$$\Delta T^* = \frac{\Delta T}{1 + i2\omega \left(\rho_{\mathrm{h}1} c_{\mathrm{h}1} d_{\mathrm{h}1} + \rho_{\mathrm{h}2} c_{\mathrm{h}2} d_{\mathrm{h}2} \right) \Delta T 2bl/P}. \tag{2.23}$$

The thermal interfaces between the layers of the heater and between heater and sample are still neglected. However, they are expected to be very small for thermally evaporated heaters. To obtain κ and D, the Eqs. (2.19) and (2.23) are evaluated numerically using the Romberg method in a modification for open intervals for the integration. This numerical model is then used in a fitting routine to obtain the parameters which agree best with the measured ΔT^* values.

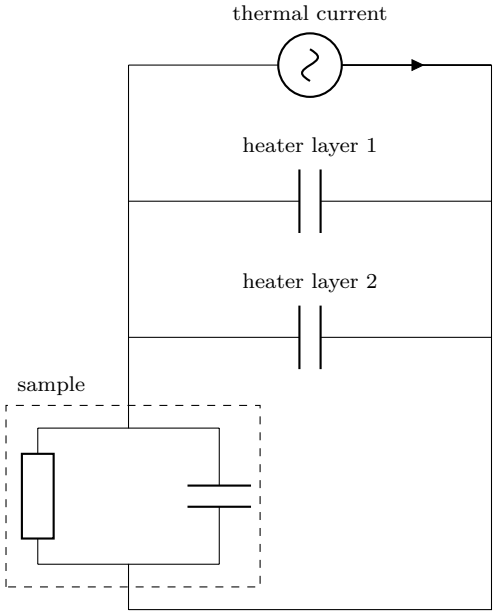

Figure 2.3: Electric equivalent circuit diagram used for the implementation of the heater's thermal capacitance in the 3ω-model.

Ångström method

The Ångström method was the first transient measurement method for obtaining D and is still used today, although to some extent superseded by flash methods. The original set-up of Ångström is depicted in figure 2.4. On one end of a long metal bar under test (a), which extends in the direction perpendicular to the figure plane, he periodically applied 0 °C and 100 °C using ice water (B) and boiling water (A), respectively. Thermometers were inserted into the metal bar and monitored at constant time intervals. After some cycles the temperatures at the thermometers followed a periodic function with the same frequency as that of the input heat flux. Heat waves propagating through the sample are attenuated according to the material's thermal diffusivity D. Also, the temperatures at the thermometers showed a phase shift in time with respect to the exciting heat flux. Furthermore, this phase shift also depends on D.

A derivation of the mathematics behind the method can be found in Ref. 43 and will be briefly summarized here. The differential equation which needs to be solved is:

$$\frac{\partial T}{\partial t} = D\frac{\partial^2 T}{\partial x^2} - \mu T, \tag{2.24}$$

where μT is a term accounting for the heat losses from the sample to the environment due to heat radiation and convection. When the experiment is conducted in a vacuum

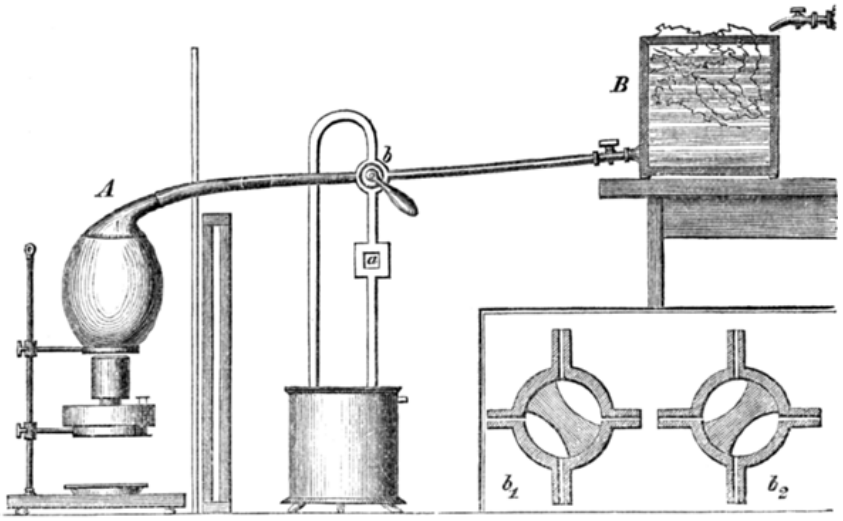

Figure 2.4: Schematic of Ångström's measurement set-up taken from his original publication [31]. The sample (a) is a bar with its long axis perpendicular to the figure plane. It can be cooled or heated periodically by ice water from tank B and steam from tank A, respectively.

where no convection occurs, μ can be approximated by a radiation constant. It is roughly equal to $4A\epsilon\Sigma T_{\text{avg}}^3$ if the average sample temperature T_{avg} can be assumed to be much larger than the amplitude of the temperature oscillations and A is the surface area of the sample. Furthermore, the temperature difference to the ambient has to be small, which can be achieved by using a heat shielding around the measurement chamber. The heat radiating from the environment towards the sample is supposed to be distributed homogeneously along the sample and, thus, does not need to be considered. As the temperature at any position of the sample bar x is expected to be periodic in time it can be expressed as a Fourier sum:

$$T(x,t) = \sum_{n=0}^{\infty} P_n(x)\cos(n\omega t) + Q_n(x)\sin(n\omega t), \tag{2.25}$$

with coefficients

$$P_n(x) = A_n \exp(\alpha_n x)\cos(\beta_n x - \chi_n) \tag{2.26}$$
$$Q_n(x) = A_n \exp(\alpha_n x)\sin(\beta_n x - \chi_n) \tag{2.27}$$

and

$$\alpha_n = \left\{ \left(\frac{1}{2} D \right) \left[\left(\mu^2 + n^2 \omega^2 \right)^{\frac{1}{2}} + \mu \right] \right\}^{\frac{1}{2}} \tag{2.28}$$

$$\beta_n = \left\{ \left(\frac{1}{2} D \right) \left[\left(\mu^2 + n^2 \omega^2 \right)^{\frac{1}{2}} - \mu \right] \right\}^{\frac{1}{2}} . \tag{2.29}$$

By inserting Eqs. (2.26) and (2.27) into Eq. (2.25) one obtains finally:

$$T(x,t) = \sum_{n=0}^{\infty} A_n(x) \exp(-\alpha_n x) \cos(n\omega t - \beta_n x + \chi_n). \tag{2.30}$$

Here A_n and χ_n are arbitrary constants depending on the boundary conditions. Additionally, it was assumed that the sample bar is semi-infinite and thus, the thermal wave is neither reflected nor dissipated at the end of the bar. Due to the need of different Fourier transformations the evaluation of the measurement data using the original method is very time consuming and sometimes even induces additional uncertainty.

Different simplifications for the case of a sinusoidal heater input were introduced by King [44] and Starr [45]. Under optimized experimental conditions only first harmonic frequencies are found in the sample temperatures and the thermal diffusivity can be calculated using the temperature curve parameters at two points of the sample for two different frequencies each. These two methods were later combined in Ref. 43 such that the measurement has to be conducted only at one frequency. Thus, sample alterations during longer measurements have a smaller impact on the measurement results. With the restriction to a sinusoidal boundary condition at $x = 0$ as a result of a sinusoidal heater input

$$T(0,t) = A_0 + A_1 \cos(\omega t + \chi_1), \tag{2.31}$$

the Fourier sum in Eq. (2.30) is reduced to the two terms with $n = 0$ and $n = 1$:

$$T(x,t) = A_0 \exp(-\alpha_0 x) + A_1 \exp(-\alpha_1 x) \cos(\omega t - \beta_1 x + \chi_1). \tag{2.32}$$

The propagation velocity of the heat waves through the bar is given by

$$v = \frac{\omega}{\beta_1} = 2\pi f \left[\frac{2D}{(\mu^2 + 4\pi^2 / f^{-2})^{\frac{1}{2}} + \mu} \right]^{\frac{1}{2}} , \tag{2.33}$$

and the amplitude decrement between two points x_1 and x_2 is

$$q = \exp(-\alpha_1 x_1) / \exp(-\alpha_1 x_2). \tag{2.34}$$

The variables v and q can be read off directly from the measured temperature charts. By using two sets of measurements with different heater frequencies the thermal diffusivity can be calculated using the velocity method [44]

$$D = \frac{v_1 v_2}{4\pi f_1 f_2} \left[\frac{v_1^2 v_2^2}{\frac{v_2^2}{f_2^2} - \frac{v_1^2}{f_1^2}} \right], \tag{2.35}$$

where f_1 and f_2 are the two excitation frequencies, respectively, and v_1 and v_2 are the corresponding propagation velocities of the heat waves. Employing the amplitude method [45]:

$$D = \frac{\pi (x_1 - x_2)^2 f_1}{\ln q_1 \ln q_2} \left[\frac{a^2 - b^2}{b^2 - 1} \right]^{\frac{1}{2}}, \tag{2.36}$$

with $a = \frac{f_2}{f_1}$ and $b = \frac{\ln q_1}{\ln q_2}$ leads to another expression of D. In both cases the radiation constant μ, which is usually unknown, has been eliminated. By combining the two methods one obtains the expression of the thermal diffusivity for only one frequency [43]:

$$D = \frac{(x_1 - x_2) v}{2 \ln q}. \tag{2.37}$$

Further extensions of this method have been introduced which, for example, make use of the Seebeck voltage as indirect temperature measurement as it shows a smaller temporal delay than thermocouples [46]. Another improvement is to use two Peltier elements for periodical heating and cooling at both ends simultaneously [47]. One disadvantage of the Ångström method is that multiple thermocouples have to be connected directly to the sample which is, however, not always possible. Also, the sample has to be long enough for the thermal wave to be attenuated before being reflected at the sample end, because the reflection is not taken into account in the derivation of the original evaluation method. An approach for the estimation of thermal diffusivities of short samples using the Ångström method is presented in Ref. 48.

3 Low temperature ZT-meter

3.1 Concept

The main idea behind the low temperature ZT-meter was to build a device which enables one to measure all thermoelectric properties needed for the calculation of ZT, all done simultaneously on the same bulk sample during the same measurement and in the same transport direction. In many publications different dedicated measurement set-ups, often requiring different sample geometries, are used for determining the transport parameters needed to calculate ZT. As a result different samples are used, which, despite identical synthesis, may vary by chance.

The focus is on the measurement of the thermal conductivity κ, since the electric conductivity as well as the Seebeck coefficient, mainly electric quantities, can be measured directly with high accuracy using a voltmeter and a current source. The measurement of κ is much more involved, as, for example, no perfect insulator for heat exists and a vacuum has to be used to prevent convection. Apart from the fact that the measurement system cannot completely consist of vacuum and some fixtures have to be used the problem of heat radiation still exists in vacuum. Thus, a set-up for thermal conductivity measurements has to be designed carefully to minimize radiation effects and also to achieve an almost perfect thermal insulation of the sample where it is required.

Figure 3.1 depicts the main components of the ZT-meter, while in figure 3.2 the supplementing devices and the wiring are shown schematically. The sample is embedded between two heat flux sensors, each consisting of a glass cylinder with three embedded thermocouples which measure the temperatures along the axis of the glass cylinder. The innermost thermocouples of both cylinders are also in direct electric and thermal contact with the sample and thus can be used to measure σ and S. With the heat flux sensors the set-up is suitable to determine κ in a comparative mode. The two sensors are each connected to a separate heater, whose power can be measured directly in a 4-contact mode. The heaters 1 and 2 allow one to apply temperature gradients along the measurement bar. Heater 1 is also used in the guarded heater mode in which only the temperature difference along the sample and the power of the heater are measured under the assumption that all heat produced

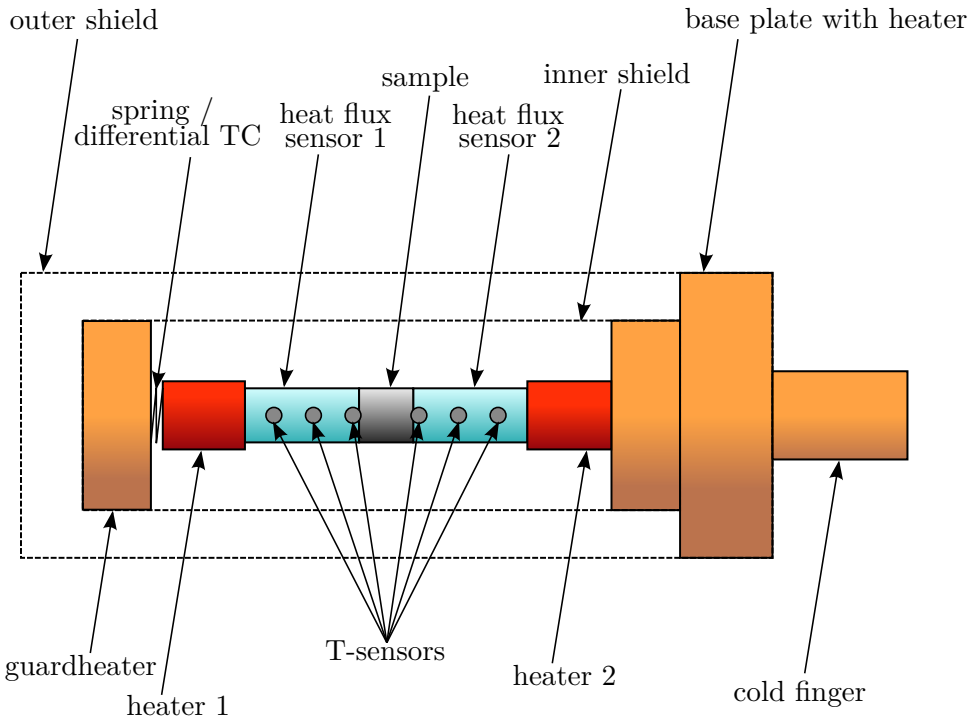

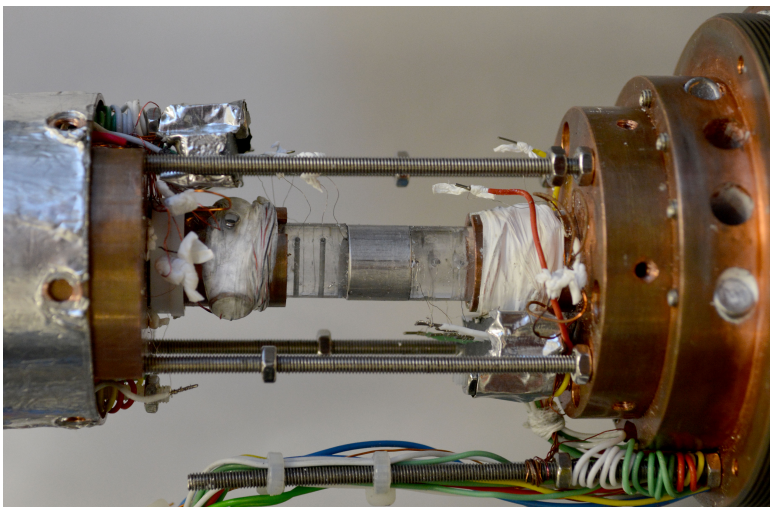

Figure 3.1: Schematical overview and photograph of the ZT-meter measurement system for low temperatures.

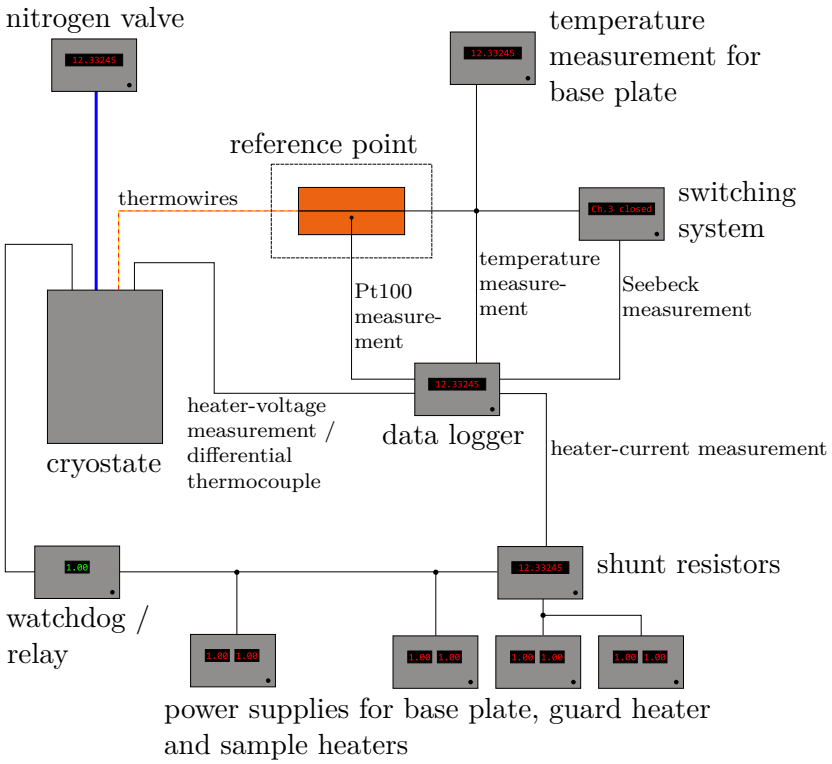

Figure 3.2: Schematical overview of the devices used in the ZT-meter measurement system for low temperatures. Copper wires are shown in black, the red-yellow line depicts the thermowires and the coolant pipe is shown in blue.

by the heater is flowing through the sample. Thus, on the one hand heater 1 has to be thermally insulated from its environment, on the other hand it needs to be mounted mechanically stable onto the sensor. This is realized by using an additional heater as a guard heater mirroring the temperature of heater 1. Both are connected using Teflon plates and a spring, allowing for the compensation of thermal expansion as well as serving as thermal insulation. The temperature difference between the guard heater and the heater is measured by a thermocouple and serves as the input signal for the guard heater control.

In order to minimize radiation effects the whole measurement bar is surrounded by a copper shield which reflects thermal radiation of the sample back onto the sample and thus keeps radiative heat transport at a minimum level. Moreover, in the optimum case the temperature distributions of the shield and the measurement bar are equal so that both are in thermal equilibrium. Only radiative transport not perpendicular to the shield would influence the measurement. As the temperature distribution along the sample and along the heat flux sensors is only linear if both have the same thermal conductivities, this ideal state is rarely achieved in a measurement. Furthermore, the shield transports heat from the guard towards the cooled base allowing for a better temperature control of the guard. The whole measurement device is mounted on top of a base plate holding a heater system as well as a cold finger. It can be cooled by liquid nitrogen or helium allowing a temperature control of the sample-holder. A second radiation shield further minimizes the heat radiation to the environment which is at room temperature.

3.2 Measurement set-up

Most voltage and resistance measurements of the set-up are carried out using a data-logger system utilizing relays for the channel switching. This has the advantage that the voltage offset of the measurement is almost equal for all channels and that this solution is comparatively inexpensive. Disadvantages are a slower measurement process, as well as time offsets between the channels which have to be accounted for. Also, relays are prone to wear and the lifetime of the instrument is constrained by the number of switching cycles. For the temperature measurements carried out with the thermocouples a copper reference point with an embedded Pt100 resistive thermometer, connected in 4-contact technique to the data-logger, is used. The whole copper block is embedded in insulating material to shield it from changes of the ambient temperature. The temperature difference between heater 1 and guard needs to be determined very accurately. It is measured directly with a thermocouple between them, with one measurement point on the guard and the other on heater 1. The thermocouple is connected by copper wires of equal length to a voltmeter. This has proven to be more accurate than using two independent thermocouples measuring the temperatures at the two points of measurements and the reference point and then calculating the difference. The disadvantage is that no absolute temperatures can be determined at the two points.

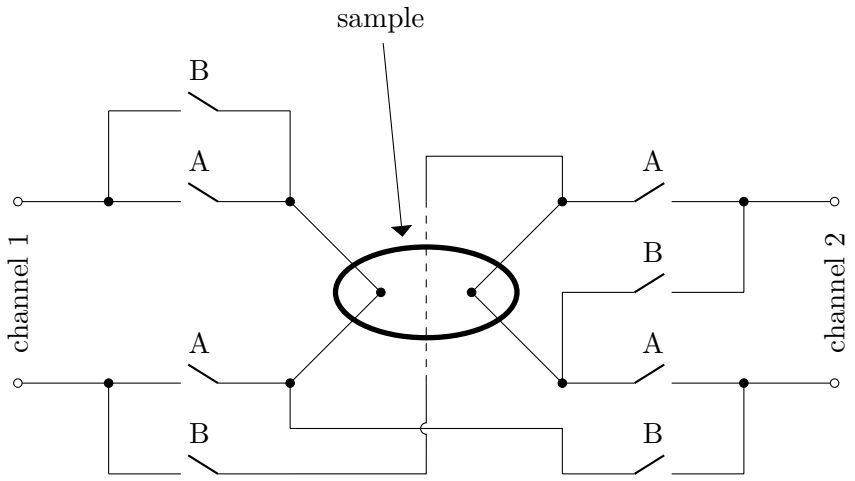

Figure 3.3: Switching circuit for the Seebeck coefficient measurements. The relays A are closed during temperature measurements while the B relays are closed for the measurements of the Seebeck voltages or the electric resistances.

The two thermocouples being in contact with the sample are also used as electric contacts in addition to serving as temperature sensors. Thus, a switching system has to be employed. Figure 3.3 depicts the relay circuit utilized to switch between the temperature measurement mode and the mode for measuring the electric transport properties of the sample. The latter is done in a quasi 4-contact configuration, in which one wire pair is used to induce a current through the sample and the resulting voltage is measured with the other pair. With this measurement configuration the resistance of the wire is eliminated. However, the measured values still depend on the contact resistance between the thermocouple junction and the sample. To account for the heat production of the coils inside the relays of the switching circuit, which may lead to unintentional thermovoltages, the circuit layout is kept strictly symmetrical for both measurement configurations. As a consequence two, for the switching function unnecessary, relays are also in use. During the measurements all four relays corresponding to a configuration are switched at the same time to yield the best possible cancellation of thermovoltages. Another result of the circuit layout being strictly symmetrical is that in configuration B the sign of the measured voltage of channel 2 needs to be reversed to correspond to the correct sign with respect to the current direction. This is accounted for in the evaluation.

The measurement of the electric resistance is carried out in a quasi 4-contact mode. The current and the voltage branches are connected to the inner thermocouples each to two wires of equal material type. As the material of the thermocouple exhibits a large Seebeck coefficient it is necessary to account for the resulting thermovoltages either by recording a complete current voltage curve or by measuring at least two points of the curve. The data logger utilized within the set-up is able to do the latter. In addition, a source meter may be used to perform fast voltage sweeps and to take

the C-V data. The resistance can then be determined by evaluating $R = \partial U/\partial I$ instead of $R = U/I$.

To reduce parasitic heat transport through the wires their diameters are chosen as small as possible. For the minimization of Joule heating of the wires, the heater resistances are chosen such that they can be driven with larger voltages and thus smaller currents while keeping the power output at the same level. Furthermore, the wires of the upper section near the guard are thermally connected to the guard, whereas the wires of the lower section are connected to the base plate.

The two sample heaters and the guard heater consist of resistors tightly inserted into copper cylinders. A common problem with Joule heaters is that the wires transport much heat as they are in direct contact with the heat source. If the wiring is not done carefully, those parasitic heat currents can be larger in magnitude than the intended heat current through the sample. The thermal resistance between the resistor and the copper has been kept small and the thin wires, serving as leads to the resistor, are wound around the copper cylinder so that the temperatures can equilibrate. However, the electric insulation has to be conserved.

The heater powers are obtained by using the data logger to determine the current through the heater as well as the voltage drop across the heater. The voltage is measured with separate wires to minimize errors due to the wire resistances. It is not possible to directly measure currents with the data logger without interrupting them during the switching of the channels. Therefore, the currents are determined by measuring the voltage over high precision shunt resistors, located outside the cryostat. All power supplies are computer controlled which may lead to safety issues if for some reason the temperature control loops fail. As a precaution relays are inserted between all heaters and their respective power supplies. All relays in the set-up are connected to a microcontroller, which sets all relays into open state if a failure is detected.

To achieve a steady base temperature as well as fast temperature changes a motorized valve controls the flux rates of the cooling liquid. The power applied for the heating of the base plate is used as input parameter for the valve's control mechanism which is parametrized for slow flux reductions if the heater power is above a certain limit. Below this limit the valve is opened very quickly, since in such situations the sample temperature cannot be cooled down further by reducing the heater power. The electronic valve has many advantages: it reduces the amount of coolant needed for a measurement and also leads to a steadier temperature at the base plate at low temperatures. With increasing heater power boiling effects of the coolant play a larger role and temperature oscillations may occur, especially at low temperatures.

All devices are controlled by a computer running a LabView program which controls the measurement instruments, the switching relays, the heaters and the coolant valve. The program handles the data acquisition by the instruments as well as the data storage. Furthermore, it provides a first evaluation of the measurement data. Moreover, digital PID control-loops can be established flexibly for all sensor-heater configurations so that the measurements take place under stable boundary

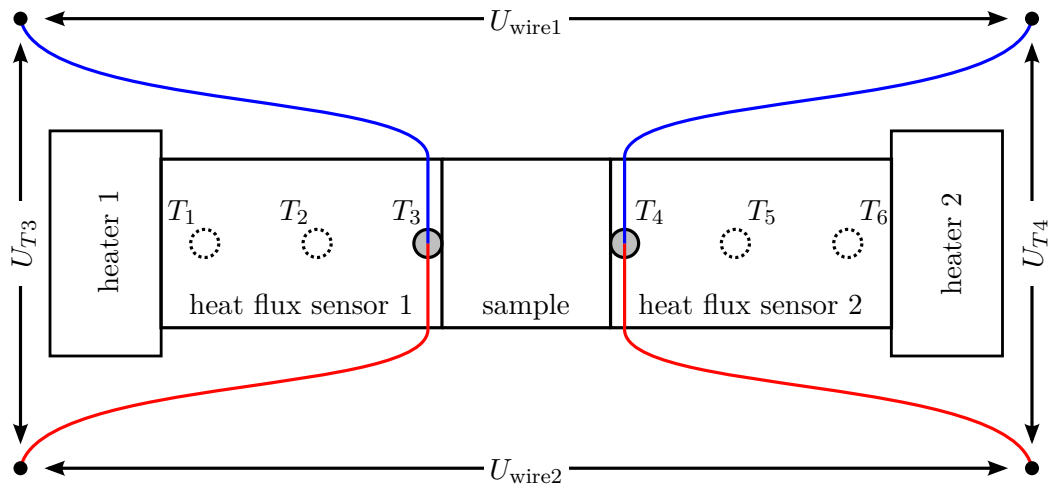

Figure 3.4: Overview of the parts of the set-up which are relevant for the measurements of the Seebeck coefficient.

conditions. Multiple heating and PID configurations can be saved as setpoints and then be executed sequentially and automatically. This takes place under the consideration of freely adjustable temperature constraints which are checked before the next setpoint is initiated. These constraints are for example temperature limits or the stability of the temperature readings of certain thermocouples.

3.3 Thermopower measurements

The measured Seebeck voltages need to be evaluated and corrected for the thermovoltages of the measurement wires. A good guidance for the analysis of Seebeck measurements can be found in Ref. 49, giving hints at the typical mistakes which can be made. The derivations and considerations discussed here are mainly following this publication. An overview of the measured quantities and the relevant parts of the set-up is shown in figure 3.4.

The first condition for valid measurements is a sufficiently small temperature difference along the sample for the assumption of a constant Seebeck coefficient S to hold. Then U, the voltage along the sample, measured at T_3 and T_4, is proportional to the applied temperature difference $\Delta T = T_4 - T_3$:

$$U = -\int_{T_3}^{T_4} S\left(T\right) dT \tag{3.1}$$

$$\approx -\left(T_4 - T_3\right) \cdot S\left(\overline{T}\right), \overline{T} = \frac{T_3 + T_4}{2}. \tag{3.2}$$

The voltage measured by the voltmeter is the sum of the thermovoltage of the sample and the contributions of the two measurement wires. S_{sample} and S_{wire} denote the Seebeck coefficients of the sample and the wires, respectively. The voltmeter is at temperature T_{ref}. The measured voltage U_{measured} is then given by:

$$\begin{aligned} U_{\text{measured}} = &- (T_3 - T_{\text{ref}}) \cdot S_{\text{wire}}\left(\overline{T}\right) && (3.3)\\ &- (T_4 - T_3) \cdot S_{\text{sample}}\left(\overline{T}\right) && (3.4)\\ &- (T_{\text{ref}} - T_4) \cdot S_{\text{wire}}\left(\overline{T}\right) && (3.5)\\ = &- (T_4 - T_3) \cdot \left[S_{\text{sample}}\left(\overline{T}\right) - S_{\text{wire}}\left(\overline{T}\right)\right]. && (3.6) \end{aligned}$$

As a result S_{sample} can be calculated using:

$$S_{\text{sample}}\left(\overline{T}\right) = -\frac{U_{\text{measured}}}{T_4 - T_3} + S_{\text{wire}}\left(\overline{T}\right). \tag{3.7}$$

However, as the thermovoltage is comparatively small, even small offset voltages at the measurement instrument may lead to large deviations. Therefore, it is advisable to conduct the measurement with different temperature gradients and thus eliminate possible offsets in U_{measured}:

$$S_{\text{sample}}\left(\overline{T}\right) = -\frac{\partial U_{\text{measured}}}{\partial \Delta T} + S_{\text{wire}}\left(\overline{T}\right). \tag{3.8}$$

Two values for S_{sample} can be obtained by evaluating Eq. (3.8) for both wire material types of the thermocouple. One problem of this method is the temporal delay between the temperature and voltage measurements due to the switching, especially if the measurements are not performed under steady-state conditions. The evaluation software for the present set-up accounts for this by performing a temporal linear interpolation of the measurements. This approach, however, is not always successful in the case of fast and nonlinear temperature changes. A further improvement is realized by the calculation of the temperatures using a numerical model presented later in this work.

In Ref. 49 another evaluation process is proposed where the Seebeck coefficient is calculated without using the temperatures at the sample boundaries T_3 and T_4. The new approach combines the equations for both wires from Eq. (3.8) to cancel out the applied temperature difference ΔT. S_{sample} can then be calculated using:

$$S_{\text{sample}}\left(\overline{T}\right) = \frac{S_{\text{TC}}\left(\overline{T}\right)}{1 - \frac{\partial U_{\text{wire1}}}{\partial U_{\text{wire2}}}} + S_{\text{wire2}}\left(\overline{T}\right), S_{\text{TC}} = S_{\text{wire1}} - S_{\text{wire2}} \tag{3.9}$$

with S_{wire1} and S_{wire2} being the Seebeck coefficients of the respective thermocouple's materials. The method does not need to directly rely on interpolated temperature

values. Only for the assignment of the resulting values to a temperature an absolute temperature measurement is required. Just the Seebeck voltages along the sample need to be acquired simultaneously. As a consequence, this approach is suitable for usage in dynamic measurement modes, in which no steady state is realized. Also, the uncertainty of the resulting values is supposed to be considerably smaller, since only two voltage measurements have to be conducted.

Both evaluation types rely on the knowledge of the absolute Seebeck coefficients S_{wire1} and S_{wire2} of the wires which need to be determined carefully. Three values for S_{sample} can be obtained by Eqs. (3.8) and (3.9), and it should be noted that the match of all three values is no suitable verification of the values for S_{wire1} and S_{wire2}.

In some of the dynamic measurement procedures, in which no steady state is reached, the Seebeck voltages are determined during changes of the base temperature using a high sampling rate. For the evaluation the measurements are assigned to groups of the same average sample temperatures and the measurements with too large temperature differences are rejected. Reversing the temperature gradient by activating the respective heater on the opposite side of the sample at the right moment in time leads to more measurements being considered and thus a smaller uncertainty.

Figure 3.5 shows a typical temperature curve of the sensors at both sides of the sample during the steps of the base temperature which are used for the Seebeck measurements. By employing heater 2 the reversed gradient is generated. Also, the corresponding Seebeck voltages of the first T-crossing of the sensors are shown and plotted against ΔT, showing a linear voltage behaviour for both branches.

3.4 Thermal conductivity measurements

With the ZT-meter the thermal conductivity of a sample can be measured in different ways. The most intuitive ones are the two steady-state modes, either using the guarded heater method or the comparative method, both presented before. A third way, the transient mode, is a mix of the Ångström method for the thermal conductivity and a heat-flow meter method for the heat capacity using arbitrary waveforms. This method will be presented in the next section. All three methods rely on the parts and the sensors of the set-up depicted in figure 3.6.

The disadvantage of the two steady-state methods are the comparatively long times needed to equilibrate the system. In particular, this holds for the guarded heater method as it employs a control loop to minimize the temperature between heater 1 and guard which adds an additional delay before reaching the steady state. Also, radiation effects have a considerable effect on the measurement quality at higher temperatures.

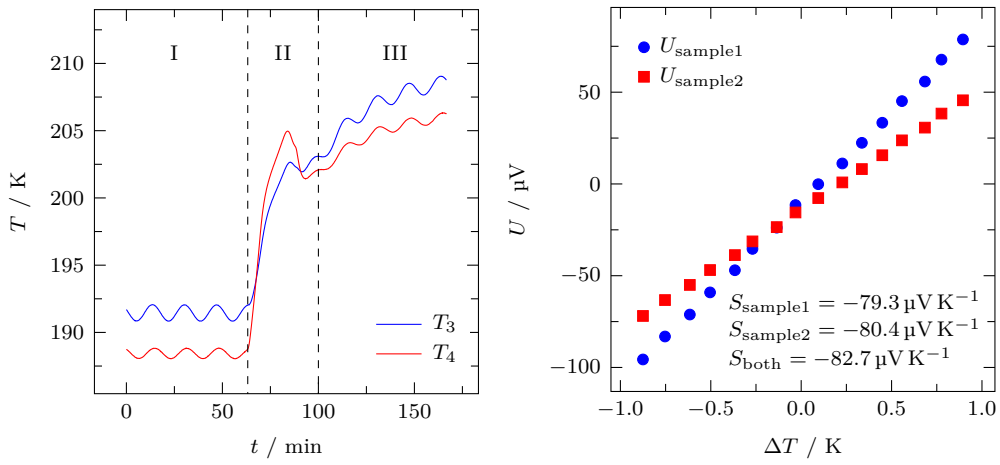

Figure 3.5: Sample temperatures (a) and corresponding Seebeck voltages (b) during a typical measurement with the set-up. In phase I measurements of the thermal conductivity κ and of the thermal diffusivity D, here at an average sample temperature of 190 K, are conducted. During phase II the base temperature of the sample is increased and the thermovoltages are measured. The sign reversal of the temperature gradient at 195 K is achieved by using heater 2 for a certain amount of time. In the third phase the measurements of the thermal properties are started at the next base temperature. The thermovoltages, shown on the right, were recorded during the first crossing of the two sample temperatures and are in a linear relationship to ΔT. They are not corrected for the contribution due to the Seebeck coefficient of the wire used in the measurement. The corrected Seebeck coefficients of the sample, S_{sample1} and S_{sample2}, are shown in the corresponding legend. Additionally S_{both}, calculated from Eq. (3.9) is depicted.

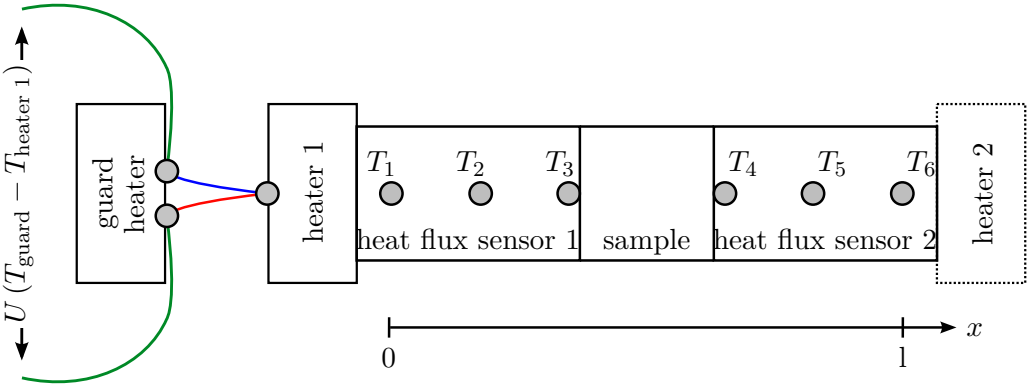

Figure 3.6: Overview of the parts of the set-up used for the measurements of the thermal conductivity κ of the sample. T_1–T_6 are thermocouples which determine the heat flux through the sample as well as the temperature gradient along the sample. With an additional thermocouple (blue and red) between heater 1 and the guard a voltage which is proportional to the temperature difference between the two is determined. The temperature can be minimized by controlling the guard heater to minimize the heat flux between guard and heater 1.

Both available steady-state methods can be combined and carried out in the same measurement cycle. This allows one to easily compare the corresponding results. When both measurement methods are used simultaneously, the procedure is the following: In a first step, after changing the base temperature by employing the base plate heater, the power of heater 1 is controlled for the upper side of the sample to reach a certain temperature. At the same time, the guard heater is utilized to minimize the voltage of the differential thermocouple between heater 1 and the guard and thereby minimizing the heat-flow between the two. Here the control loop for the minimization is configured with quite aggressive PID parameters, compared with the conservative values used for the control of heater 1. Both heaters interact with each other and the coupling constants of the two control loops are not known precisely enough to use a more sophisticated control method. After the temperatures T_1 to T_6 have reached a certain degree of stability, the control loop for heater 1 is disabled and the heater power is kept constant. The control loop of the guard heater stays enabled until a steady state is reached and finally the measurements are performed. In order to save time the heater powers of both heaters are saved and used as start values at the next base temperature step.

The evaluation of the measurement data is done using Fourier's law, as written in Eq. (2.6), in case of the guarded heater mode and with Eq. (2.17) in case of the comparative mode. For the calculation of the temperature gradient in the heat flux sensors, needed in Eq. (2.17), a least-squares fit of the three temperatures in each sensor is used. Following the least squares approach for linear functions and inserting it into Eq. (2.17), leads to an expression for κ_{sample}:

$$\kappa_{\text{sample}} = -\frac{\kappa_{\text{sensor}} l_{\text{sample}}}{2\Delta T_{\text{sample}}} \cdot \frac{T_1\,(x_2 + x_3 - 2x_1)\,T_2\,(x_1 + x_3 - 2x_2)\,T_3\,(x_1 + x_2 - 2x_3)}{x_1^2 + x_2^2 + x_3^2 - x_1x_2 - x_2x_3 - x_1x_3}. \tag{3.10}$$

Here T_1, T_2 and T_3 are the temperatures of the thermocouples inside the sensor, x_1, x_2 and x_3 are the respective positions of the sensors, ΔT_{sample} is the temperature difference along the sample and l_{sample} the sample length.

3.5 Transient heat conduction

In the following an additional method enabling one to determine not only the heat conductivity of a sample but in addition also its heat capacity with the *ZT*-meter set-up, will be presented. As source for the extra information about the heat capacities the time dependence of the temperatures T_1 to T_6 is used. It combines the direct measurement of κ as in the steady-state methods with the speed of transient methods, at the cost of a much more complicated evaluation.

The sensors and the samples have to be in a known state at the beginning of the measurement. An easy way to achieve that is to bring the sample in a defined steady state along the measurement bar as the starting point of a transient measurement. However, it is also possible to use periodic oscillations as a start condition. During the measurement heat fluxes from both sides of the sensor-sample arrangement will change the temperatures of the sensors. These temperature variations are determined by the heat conductivities and heat capacities of both, sample and heat flux sensors. Unfortunately, the heat flux cannot be determined directly by using the heater's power, since a guarding method might be too slow to handle fast temperature changes. Thus, the heat fluxes cannot be used as a boundary condition in the modelling required to extract the sample's heat conductivity and heat capacity. The temperature at the sensors are recorded as a function of time until no further information about the sample properties can be gained from the measurements. A method to estimate the effect of prolonged measurement duration on the reduction of the measurement uncertainties will be presented and may be used in real-time during the measurements if further optimized for speed.

The heat capacity and heat conductivity of the sample are extracted by fitting the measurement data to a numerical model of the heat flux sensors and the sample. The model is based on the method of finite differences and uses the time-dependent temperatures measured at the two outermost thermocouples (T_1 and T_6) and the respective material parameters heat conductivity κ and the volumetric heat capacity $c \cdot \rho$ of the heat flux sensors and the sample as input parameters (figure 3.7). In the fitting procedure the temperatures are calculated for discrete time steps on discrete grid points, are interpolated temporally and spatially to match the measurement conditions, and are compared with the measured values. The sum of the differences

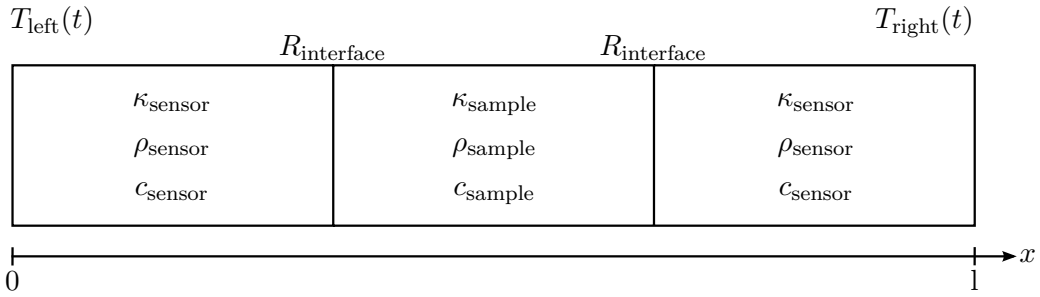

Figure 3.7: Diagram of all physical parameters used as input parameters in the numerical model for the transient heat conduction in the heat flux sensors and the sample.

among all measurement points and the simulation results is defined as the cost function for an optimization algorithm and is being minimized to obtain $c\rho$ and κ of the sample.

In the following the numerical model, employed to calculate the temperatures in the sample, will be discussed. A number of methods exists to calculate the temperatures inside a one-dimensional homogeneous bar for different boundary conditions, both analytically and numerically in the form of finite differences. As a consequence of using the measurement data for the outermost sensors as an input parameter of the model, the boundary condition is not an analytic expression, thus, a numerical model has to be employed. The measurement bar can consist of at least two different materials for sensors and the sample and therefore cannot be regarded as homogeneous. Some modifications of standard numerical methods have to be made to allow for inhomogeneous material parameters as well as non-uniform spatial discretizations. The latter is needed to enable one to perform calculations for arbitrary sample and sensor sizes. Starting point of the derivation of the model is the heat conduction equation (Eq. 2.13):

$$c(x) \cdot \rho(x) \cdot \frac{\partial}{\partial t} T(x,t) = \nabla \left[\kappa(x) \cdot \nabla T(x,t) \right]. \tag{3.11}$$

By separating the spatial and temporal parameters one obtains an expression which can be discretized in two steps:

$$\frac{\partial}{\partial t} T(x,t) = \frac{1}{c(x) \cdot \rho(x)} \cdot \nabla \left[\kappa(x) \cdot \nabla T(x,t) \right] \tag{3.12}$$

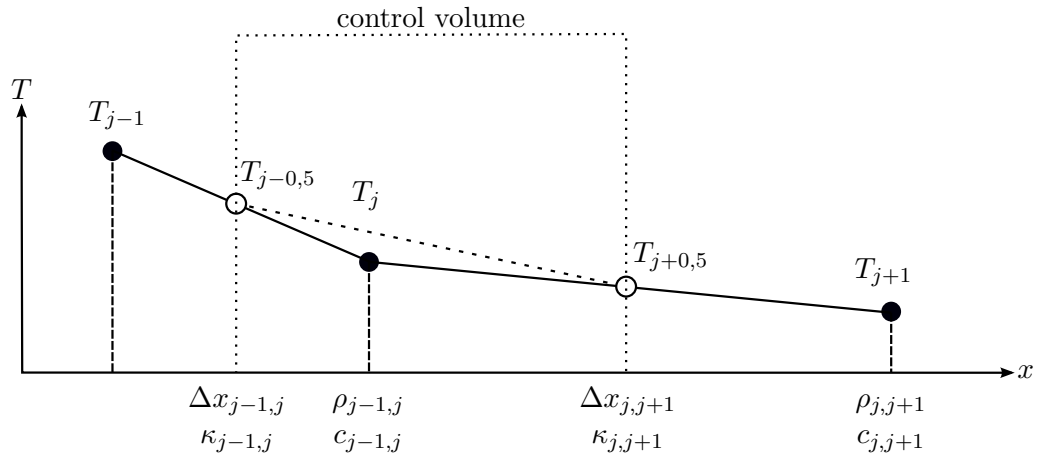

Figure 3.8: Scheme of the finite differences model used to solve the transient heat equation. Temperatures T, heat capacities c and densities ρ are defined at the grid points, thermal conductivities κ are defined in between. Δx resembles the distances between the points.

$$\frac{T_j^{m+1} - T_j^m}{\Delta t} = \frac{1}{c_j \cdot \rho_j} \cdot \nabla \left[\kappa(x) \cdot \frac{T_{j+0,5}^m - T_{j-0,5}^m}{(\Delta x_{j,j+1} + \Delta x_{j-1,j})/2} \right] \tag{3.13}$$

$$= \frac{1}{c_j \cdot \rho_j} \cdot \left[\frac{2\kappa_{j,j+1} \cdot (T_{j+1}^m - T_j^m)}{\Delta x_{j,j+1} \cdot (\Delta x_{j,j+1} + \Delta x_{j-1,j})} - \frac{2\kappa_{j-1,j} \cdot (T_j^m - T_{j-1}^m)}{\Delta x_{j-1,j} \cdot (\Delta x_{j-1,j} + \Delta x_{j,j+1})} \right] \tag{3.14}$$

$$=: f\left(t_m, T^m\right). \tag{3.15}$$

In Eq. (3.13) the temporal discretization was carried out by using the forward difference quotient whereas in case of the spatial discretization a central difference quotient has been applied. This constellation is often known as the Forward-Time Central-Space-scheme (FTCS), the temporal discretization is identical to the explicit Euler method. The continuous variables for the spatial coordinate x and the time t have been replaced by discrete positions j and points in time m. The distance between two neighbouring grid points k, l is given by $\Delta x_{k,l}$ and the difference between two consecutive time steps by Δt. In case of the spatial discretization two temporary grid points were introduced which are only used in the first derivation step. The definition of the variables and grid points is depicted in figure 3.8. By approximating the second derivative with respect to position one obtains Eq. (3.14). The additional grid points cancel out and solving for T_j^{m+1} leads to the conditional equation for the temperature at the grid point j at the next time step $m + 1$.

The temperatures are then calculated for all grid points and all time steps. As stated before the starting conditions need to be known and the easiest way is to assume stationary conditions and obtain the starting temperatures by solving the

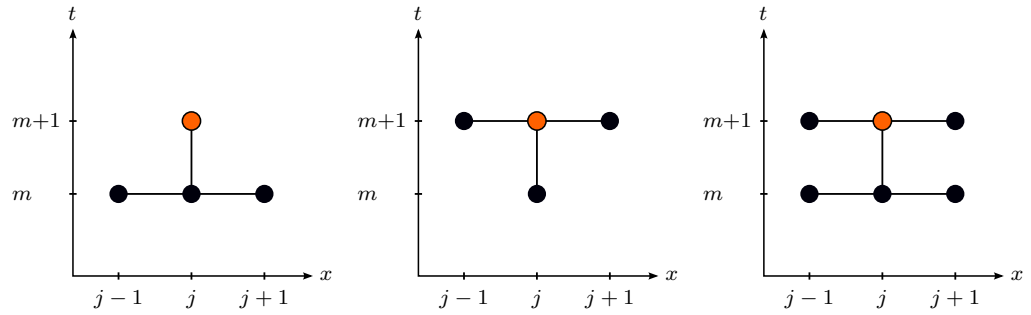

(a) FTCS (b) BTCS (c) Crank-Nicolson

Figure 3.9: The stencils for the FTCS, the BTCS and the Crank-Nicolson schemes show the spatial and temporal relationships of the grid points which are implemented by the respective equation. The yellow points indicate the grid points under calculation.

stationary heat equation 2.6. Hereby the two outermost temperatures are used again as boundary conditions. For time steps small enough the method is numerically stable. As an indication for the required time step length serves the following relationship [50]:

$$\frac{\kappa(x) \cdot \Delta t}{c(x) \cdot \rho(x) \cdot \Delta x^2} < \frac{1}{2}. \tag{3.16}$$

If this condition is not fulfilled, the FTCS-scheme may yield unstable and oscillating solutions.

If the backward differences were applied on the left hand side of Eq. (3.14), this would result in the implicit Backward-Time Central-Space-scheme (BTCS). Regarding the heat equation this method is stable and shows no oscillations for large time steps. The global truncation errors are $\mathcal{O}(\Delta x^2)$ and $\mathcal{O}(\Delta t)$, and are identical to those of the FTCS. However, due to the implicit nature of the equation the numerical and the implementation efforts are significantly larger. A similarly numerically costly combination of both schemes is the Crank-Nicolson-scheme, which is also stable if applied to the heat equation. The truncation error in time is of the order $\mathcal{O}(\Delta t^2)$ [51, 52]. Figure 3.9 illustrates the stencils for the different schemes.

One way to improve the temporal truncation error of the explicit Euler method without using the more complex implicit methods is the implementation of a predictor-corrector method like the Heun's-method [53], also known as improved Euler's method. This second order Runge-Kutta method is shown in the following:

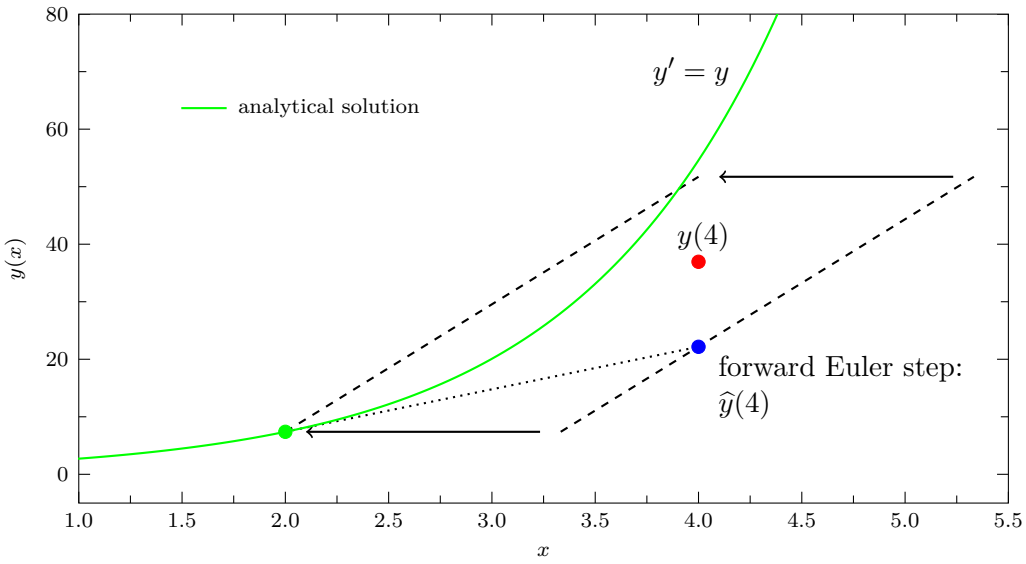

Figure 3.10: Heun's method illustrated for the differential equation $y' = y$ with $y_0 = y(2)$ as startpoint: the blue circle shows the result of the predictor step $\widehat{y}(4)$, the red circle the result of the corrector step $y(4)$. The step size of 2 has been exaggerated for illustration purposes.

$$\widehat{T}_j^{m+1} = T_j^m + \Delta t \cdot f\left(t_m, T^m\right) \tag{3.17}$$

$$T_j^{m+1} = T_j^m + \frac{\Delta t}{2} \cdot \left[f\left(t_m, T^m\right) + f\left(t_{m+1}, \widehat{T}_j^{m+1}\right) \right], \tag{3.18}$$

where the function $f\left(t_m, T^m\right)$ is defined by the right-hand-side of Eq. (3.14), which is the approximation of the partial derivative of the temperature with respect to t at the m^{th} time step. The first step (Eq. 3.17) is the original forward Euler step, the so called predictor. Its result $\widehat{T}_j^{m+1}$ is used as an argument for f in the second step (Eq. 3.18), which is called corrector step. The results of f in both steps are averaged and carried into the next iteration. Figure 3.10 shows the principle of the method graphically.

The predictor step has an order of accuracy of $O(\Delta t)$ while the corrector step shows a global truncation error of $O(\Delta t^2)$ [54]. A downside of this approach is the roughly doubling of the computation time, as the function f has to be evaluated twice for each time step. The stability condition stays the same as for the original Euler method. Figure 3.11 depicts a comparison between the forward Euler method and Heun's method, showing the improved convergence rate of the latter method regarding Δt.

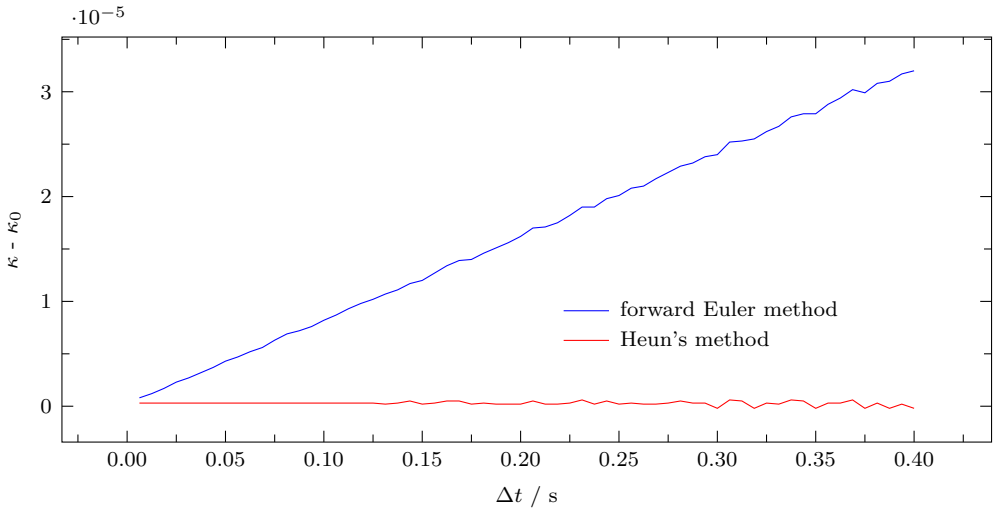

Figure 3.11: Comparison of the forward Euler method with the Heun's method: fit-results using the Euler method converge linearly with Δt while the results using Heun's method show quadratic behaviour.

With this procedure the simulation provides the time-dependent temperatures at the grid points. To enable a comparison between the simulation and the measurement the simulation results are interpolated quadratically in time and space. The position of the two outermost and the two innermost grid points are always chosen to be on the exact position of the respective thermocouples T_1, T_3, T_4 and T_6. Having the temperature data in a continuous form the following cost function can be calculated and minimized:

$$\chi^2 = \sum_n \sum_i \left[T(x(i), t(n)) - T_i(t(n)) \right]^2 , \tag{3.19}$$

where i is the index labelling all thermocouples and n is the measurement index. The cost function can be minimized for the desired parameters κ_{Sample}, κ_{Sensor}, $c\rho_{\text{Sample}}$ or $c\rho_{\text{Sensor}}$. The specific heat capacity c and the density ρ cannot be determined independently. Also, only three of the four parameters above can be evaluated simultaneously without knowledge of the exact heat-flows into the sample. However, if the parameters of the sensors are known, the system becomes over-determined and the additional parameter may be used for error estimation. Figure 3.12 shows a plot of χ^2 with varying values of κ and $c\rho$. It shows a single minimum which can be found easily with an appropriate algorithm and also reveals that the sensitivity towards $c\rho$ is much smaller compared to that towards κ. The sensitivity ratio can be shifted by changing measurement parameters such as the thermal diffusivity of the sensors or the waveform of the heater input.

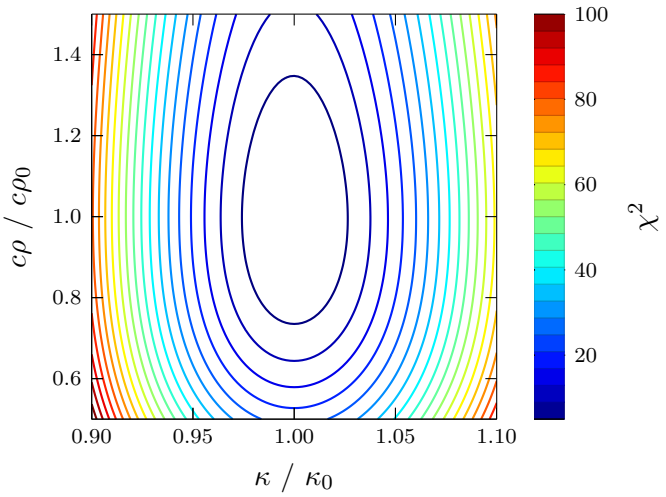

Figure 3.12: The contour plot of χ^2 for variations of κ and $c\rho$ shows a simple structure with a single minimum. For all simulation cases only single minima have been observed, resulting in short convergence times for the optimization algorithm. The contour plot shows that χ^2 is much more sensitive towards changes of the κ than towards changes of $c\rho$.

3.5.1 Implementation of interface resistances between sample and sensors

In order to handle interface resistances between the two sensors and the sample in the transient simulations a new set of equations has to be derived, accounting for the thermal transport across the material boundaries. As shown in figure 3.13 additional grid points are introduced so that each boundary is now enclosed directly by two grid points.

The relation between the thermal interface resistance $R_{\text{Interface}}$, the temperatures of the two grid points on the two material surfaces, T_j and T_{j+1} and the thermal current through the interface q is given by:

$$R_{\text{Interface}} = \frac{T_j - T_{j+1}}{q}. \tag{3.20}$$

By applying the control-volume-method [55] to the problem an equation for the heat transport via the left grid point at T_j can be obtained:

$$A \cdot c_j \cdot \rho_j \cdot \Delta x_{j-1,j} \cdot \frac{T_j^{n+1} - T_j^n}{2\Delta t} = A \cdot \kappa_{j-1,j} \cdot \left.\frac{\partial T}{\partial x}\right|_{j-0,5} - A \cdot q, \tag{3.21}$$

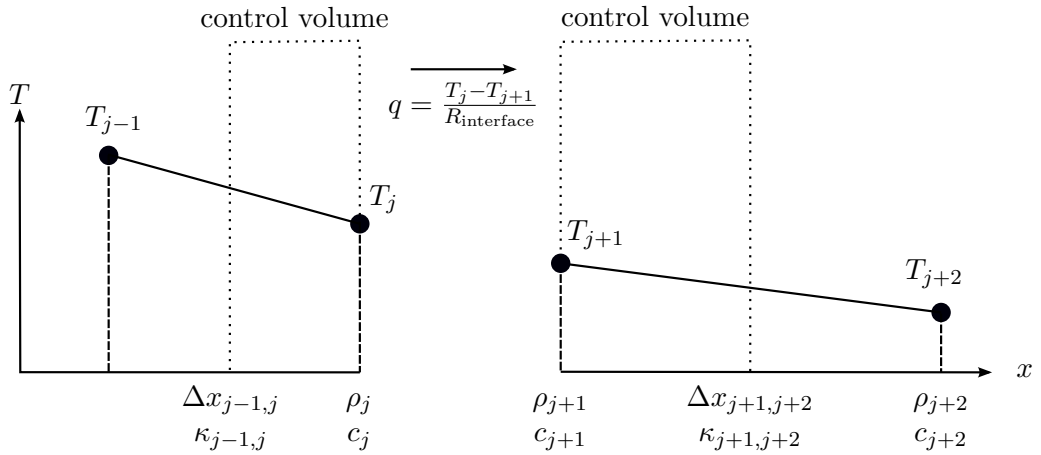

Figure 3.13: Illustration of the implementation of interface resistances by using the control volume method.

where A denotes the area of the heat flux sensors and the sample. By expressing the partial derivative by a difference quotient and reordering the spatial and temporal terms the following equation is derived:

$$\frac{T_j^{n+1} - T_j^n}{\Delta t} = \frac{2\kappa_{j-1,j}}{\rho_j \cdot c_j} \frac{T_{j-1}^n - T_j^n}{\Delta x_{j-1,j}^2} - \frac{2q}{\rho_j \cdot c_j \cdot \Delta x_{j-1,j}^2}. \tag{3.22}$$

In both equations the minuends on the right sides treat the normal bulk transport while the subtrahends treat the thermal current across the interface.

In a similar manner one obtains for the right grid point T_{j+1}:

$$A \cdot c_{j+1} \cdot \rho_{j+1} \cdot \Delta x_{j+1,j+2} \cdot \frac{T_{j+1}^{n+1} - T_{j+1}^n}{2\Delta t} = A \cdot \kappa_{j+1,j+2} \cdot \left.\frac{\partial T}{\partial x}\right|_{j+1,5} - A \cdot q \tag{3.23}$$

and

$$\frac{T_{j+1}^{n+1} - T_{j+1}^n}{\Delta t} = \frac{2\kappa_{j+1,j+2}}{\rho_j \cdot c_j} \frac{T_{j+2}^n - T_{j+1}^n}{\Delta x_{j+1,j+2}^2} - \frac{2q}{\rho_{j+1} \cdot c_{j+1} \cdot \Delta x_{j+1,j+2}^2}. \tag{3.24}$$

In the system of Eqs. (3.20), (3.22), (3.24) the variable q may now be eliminated and solutions for T_j^{n+1} and T_{j+1}^{n+1} may be found.

3.5.2 Implementation of heat radiation

To account for effects of heat radiation in the simulation a simple model is derived, where the ambient temperature is assumed to be constant. This corresponds to

the situation where the inner shield, despite all precautions, does not mirror the temperature distribution of the measurement column and, on the contrary, is at a constant temperature.

The net-heat exchange between two bodies at different temperatures is given by the Stefan-Boltzmann-law in Eq. (2.15). To obtain an expression for a cylindrical column this can be inserted as an external heat source into the heat equation given in Eq. (3.12):

$$c(x) \cdot \rho(x) \cdot \frac{\partial}{\partial t} T(x,t) = \nabla \left[\kappa(x) \cdot \nabla T(x,t)\right] + \frac{2\pi r h}{\pi r^2 h} \epsilon \Sigma \left(T^4 - T^4_{\text{ambient}}\right), \qquad (3.25)$$

where r is the radius and h is the height of the cylinder.

It should be noted that this is only an approximation, as the thermal conduction is calculated in one dimension only. In reality the radiation leads to a heat-flow perpendicular to the direction of the heat conduction. For wider cylinders a two-dimensional calculation is required. However, in the geometries used in this work, other sources of error, such as the unknown ambient temperatures and emissivities, are expected to have a larger impact than the approximation made in Eq. (3.25).

3.5.3 Uncertainty analysis

As the temperature values acquired by the sensors are experimentally measured quantities they possess a certain degree of uncertainty due to limited accuracy and limited precision of the set-up and its instrumentation. Those uncertainties influence the thermal conductivities and diffusivities, obtained by the fit algorithm introduced in the previous section. In this section a method [56] for estimating the uncertainties of the derived quantities is presented.

The standard procedure to propagate the uncertainty from the measured to the derived quantities is to calculate the covariance matrix which might already be determined during the χ^2 minimization. However, if the function or the physical model is non-linear, the uncertainties of the derived quantities may deviate from a Gaussian distribution and the conclusions drawn from the covariance matrix may be invalid. Moreover, the fitting algorithm itself and the numerical model describing the experiment might lead to additional uncertainty which is also not accounted for by the covariance method.

The method employed in this work is a Monte-Carlo simulation and circumvents these problems. The principle of this approach is shown in figure 3.14. First the χ^2 minimization is applied to the data measured and a set of parameters a_0 is obtained. In the next step, the measurement data are used to create a synthetic data set with an additional normal-distributed uncertainty. Unfortunately, as the measurement data is not an independent set of data-points, the bootstrap method, shown in Ref. 56, cannot be applied and the uncertainty in the temperature measurement

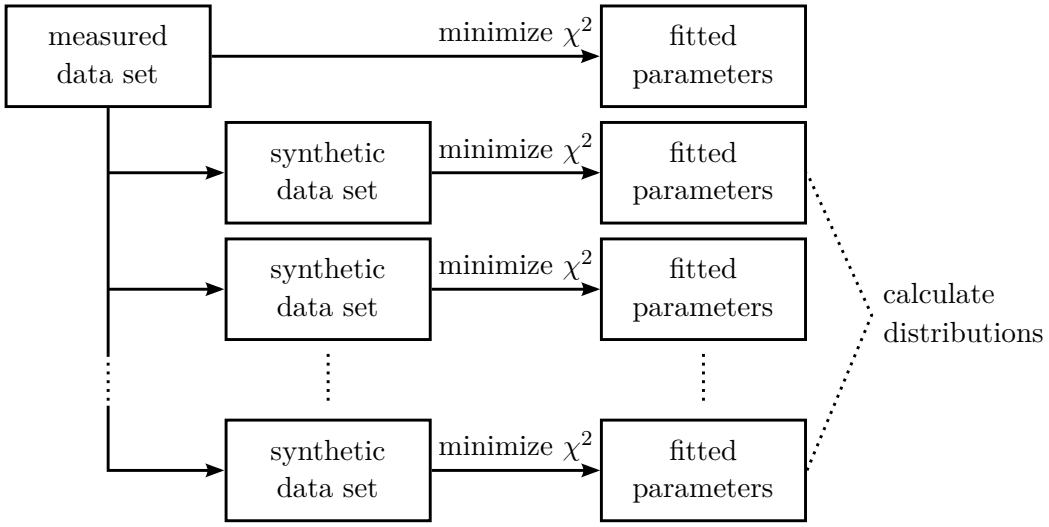

Figure 3.14: Flow-chart of the Monte-Carlo simulation used to estimate the uncertainty of the derived parameters.

has to be estimated. As an approximation the noise and its standard deviation in the temperature measurement can be determined and used for the generation of the synthetic data sets by adding the noise to the measured values:

$$T_{\text{synthetic}} = T_{\text{measured}} + \Delta T. \tag{3.26}$$

The absolute statistical measurement uncertainty for thermocouples ΔT is, by assuming a linear $U - T$ relationship, approximately given by:

$$\Delta T = \sqrt{\Delta T^2_{\text{reference point}} + \left(S_{\text{thermocouple}} \cdot \Delta U\right)^2}, \tag{3.27}$$

with $\Delta T_{\text{reference point}}$ being the absolute uncertainty of the temperature of the reference point, $S_{\text{thermocouple}}$ being the Seebeck coefficient of the thermocouple and ΔU the absolute uncertainty of the voltage measurement. As ΔU is larger for lower temperatures, the statistical uncertainty for the temperatures is usually higher at low temperatures.

The fitting process is then applied to a number of synthetic data sets. The statistical distribution of the obtained parameters contains information on the uncertainty of the derived parameters. Based on these results conclusions on the efficiency of different measurement modes may be drawn.

3.5.4 Implementation of the model

The model was completely implemented as a C++ program and is able to load the measurement data, to interpolate the temperature data of the outer thermocouples

and to simulate the temperature distribution in the measurement bar for given material parameters. Eventually the results are compared with the input data using Eq. (3.19) and χ^2 is shown as output. As most of the processing time is spent inside the simulation loop, and in particular for the repeated calculation using Eq. (3.14), the loop was optimized to utilize the SSE/AVX SIMD extensions of modern processors. In theory a performance gain of up to 400 % on an AVX processor in double precision can be achieved. However, it was not optimized for the use of multiple processor cores in the simulation loops, since the synchronization overhead would be too large in comparison with the relatively short computations in a single time step. The Monte-Carlo simulation, employing multiple single fits, can be run in parallel.

A first program mode only calculates χ^2 for a given set of parameters and measurement data. In a second program mode χ^2 is minimized by varying the material parameters of the sample and running the simulation of the first program mode several times. The optimization is done using PRAXIS, a C implementation of Powell's method by Karl Gegenfurtner [57–59]. Powell's method is a modification of the conjugated gradients method which does not rely on calculated gradients. As in some cases PRAXIS uses random steps to overcome small local minima, the fitting results may not always be the same for different runs. Consequently, the optimization routine can be run multiple times on the same data set to obtain the optimal fitting results.

A third program mode implements the Monte-Carlo simulation presented in section 3.5.3. The routine of the second program mode is run multiple times on an identical measurement data set, modified for each run with a simulated error. This was implemented by adding pseudo-random numbers following a normal distribution with a given standard deviation to each measurement value. The program is able to use the pseudo-random number generators SHR3, CONG and MWC as well as KISS the latter being a combination of the other three. The uniform distribution of these pseudo-random numbers is then converted into a normal distribution using a C implementation of the Ziggurat algorithm [60–62].

3.6 Testing of the model using Comsol Finite Element simulations

The first tests of the implemented model were performed by taking data generated with the Finite Elements tool *Comsol Multiphysics 4.4* as input parameters. With Comsol the heat transport in a segmented bar was simulated very precisely for different heating parameters and material parameters. The simulated, time-dependent temperature data could then be used as input parameters for the fit-program described above. This enables one to study the influence of different parameter-sets and boundary conditions on the fit-routine itself, while excluding experimental issues. The results of these investigations are presented in the following.

If not stated otherwise, the Comsol simulations used cylindrical heat flux sensors and samples with a length of 10 mm and a radius of 6 mm, which is close to the geometries used in the actual set-up. The volumetric heat capacity for samples and heat flux sensors was $c\rho_0 = 2\,\mathrm{MJ\,K^{-1}\,m^{-3}}$ and the thermal conductivities of the heat flux sensors were $\kappa_{\mathrm{sensor}} = 2\,\mathrm{W\,m^{-1}\,K^{-1}}$ and $\kappa_0 = 1\,\mathrm{W\,m^{-1}\,K^{-1}}$ for the sample. On one side of the sensor-sample-sensor combination a constant temperature of 273.15 K has been assumed, on the other side a time dependent heat flux was injected. Time frames of $10,000\,\mathrm{s} \approx 2.77\,\mathrm{h}$ were considered in the simulations. This simulation parameters are tabulated in table B.1.

3.6.1 Round-off, truncation, and interpolation error

The presented numerical method for the calculation of the temperatures in the measurement bar is prone to three primary sources of error. The first type of error arises because the data types used for numerical calculations in computers cannot represent values with infinite precision. Most calculation results need to be rounded. This leads to minor round-off errors at every calculation step which might sum up to larger errors, especially in large simulations with small time steps. However, in the implementation the usage of both single and double data types for floating-point calculations were compared and no quantitative differences could be found.

A second source of error are truncation errors, which occur due to the spatial and temporal discretization. Eq. (3.14) is exactly equal to Eq. (3.12) for infinitely small time steps and infinitely small Δx only. For the calculations performed here a trade-off between small time steps and high spatial resolution (i.e. the resulting large accuracy and long computation time) has to be found. As Heun's method is used in the implementation, the global truncation errors are $O(\Delta t^2)$ and $O(\Delta x^2)$.

In addition to the previous error sources, appearing in most numerical simulations, spatial and temporal interpolations are another source of uncertainty in the simulations carried out in this work. The interpolations are applied to the input temperatures prior to the simulation as well as to the output temperatures and the grid positions during the calculation of χ^2. In figure 3.15, which depicts the fit-results for $c\rho$ for an increasing number of grid points, one can observe that every second data point shows a larger difference to the original value $c\rho_0$. These deviations originate from the fact that in every second simulation the grid points do not coincide with the positions of the thermocouples being in the middle of the heat flux sensors. Thus, their temperatures have to be linearly interpolated in the calculation of χ^2, leading to larger deviations from the true values. The usage of smaller Δx steps is, however, limited by the stability criterion valid for the forward Euler method, given by Eq. (3.16).

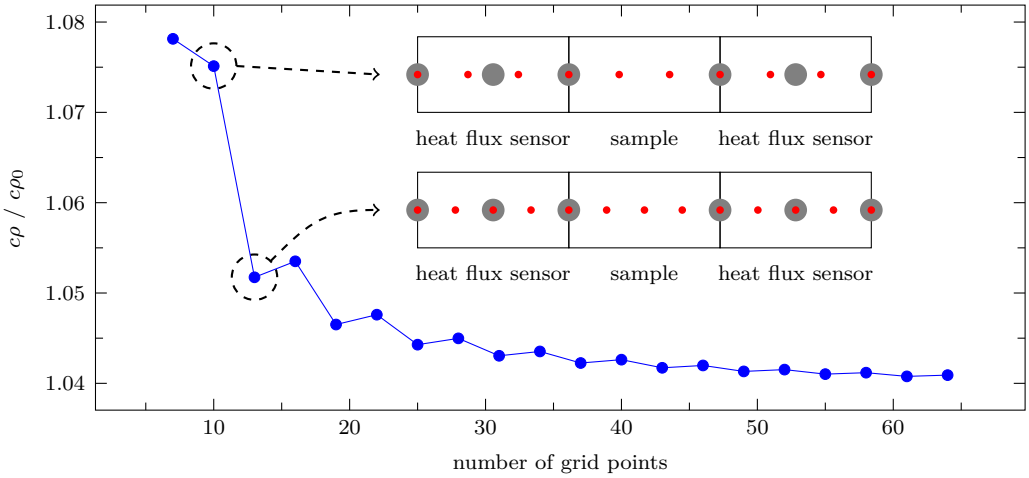

Figure 3.15: For finer spatial grid resolution the fit-results converge towards a fixed value as the spatial truncation error is reduced. One can observe that every second refinement step shows a larger deviation which is due to linear interpolation of the temperatures at the probe points (gray circles) if the probes are not located directly on a grid point (red circles).

3.6.2 Influence of the pseudo-random number generator on the Monte-Carlo simulations

Although the pseudo-random number generators (PRNG) implemented for the Monte-Carlo simulations pass several statistical tests on the randomness they are not suited for generating true random numbers. To test whether the algorithm of the PRNG has a direct influence on the simulation results, a set of Monte-Carlo simulations has been carried out using different PRNGs and two different standard deviations for the input temperatures. The results, plotted in figure 3.16, show no obvious dependence of the calculated standard deviations of the fit-results on the chosen PRNG. This, however, can never be totally excluded.

3.6.3 Interpretation of the Monte-Carlo results

In figure 3.17 the fit-results of 10,000 Monte-Carlo runs with a standard deviation σ of 0.1 K for the input temperature error distribution are shown as well as the corresponding 99^{th} percentile ellipse. It can be observed that the ellipse is not skewed and the distributions regarding both parameters follow a Gaussian distribution. Also, it can be seen that the $c\rho$ parameter seems to be more sensitive to error than κ, since its standard deviation in relation to its absolute value is larger.

However, in this plot the average of the parameters obtained using the Monte-Carlo simulations deviates from the fit-results on undisturbed data. As this deviation shows

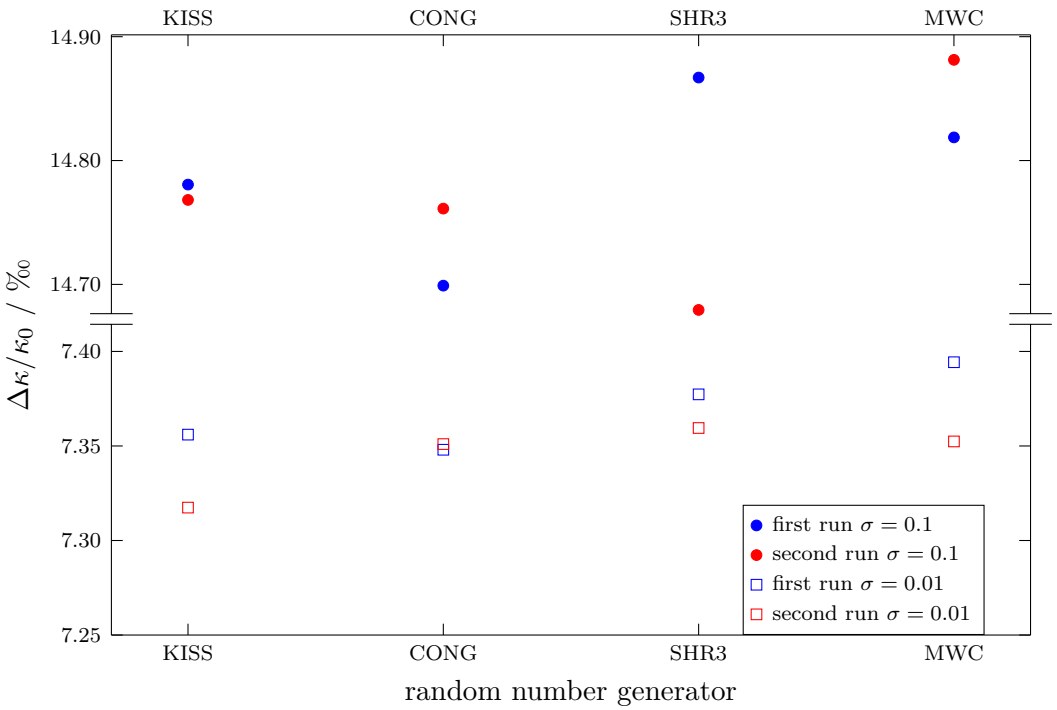

Figure 3.16: The comparison of the four different pseudo-random number generators used to obtained synthetic data sets shows no clear dependence of the choice of the PRNG on the results. Each data point was determined using 10,000 Monte-Carlo iterations.

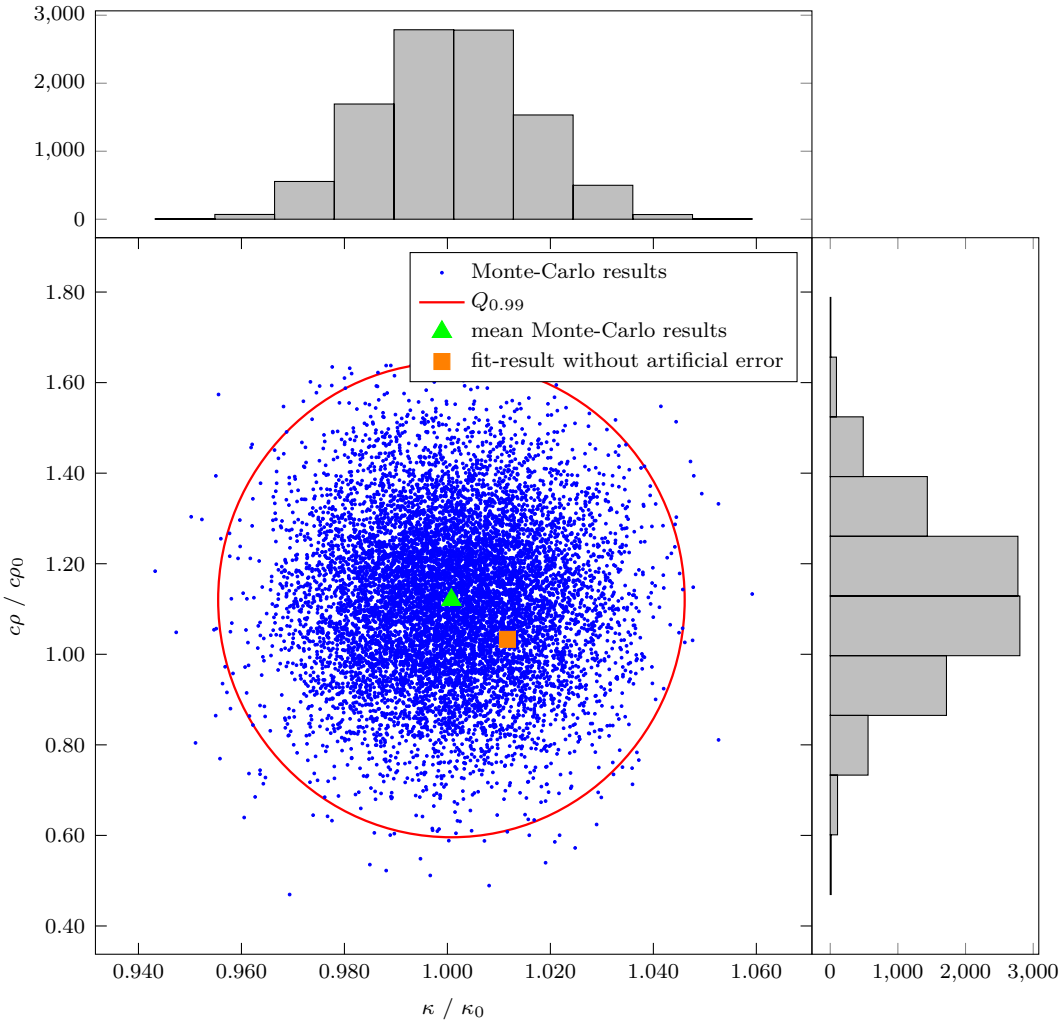

Figure 3.17: Data set of a Monte-Carlo simulation including 10,000 points with κ and $c\rho$ of a sample as free parameters. The histograms show Gaussian distributions and the mean value of the data points from the Monte-Carlo simulation deviates from the fit values of the undisturbed simulation.

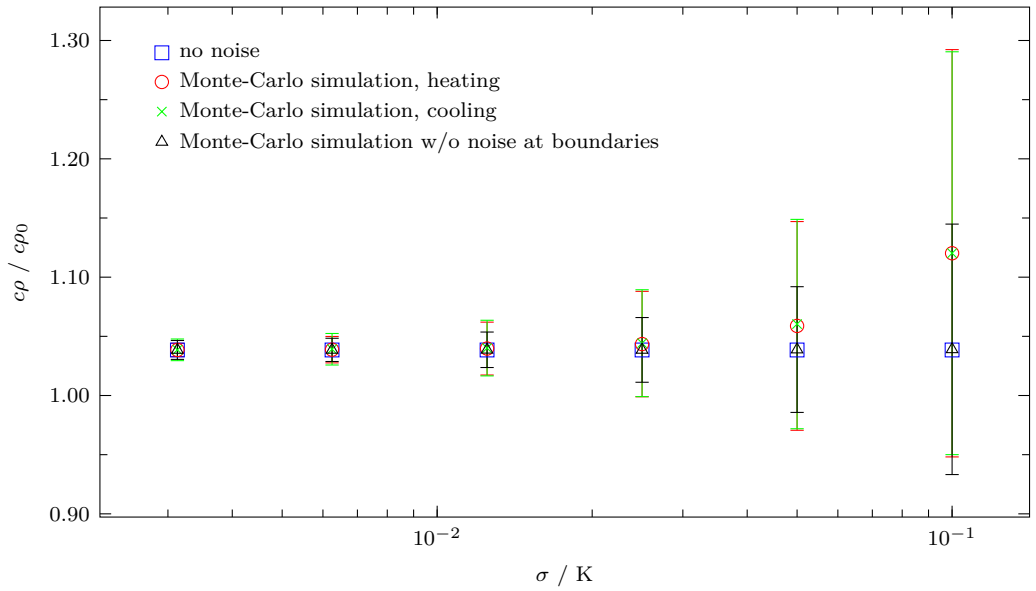

Figure 3.18: Monte-Carlo results for the $c\rho$ parameter at different standard deviations σ, obtained with 10,000 fits per data-point: the mean values of the Monte-Carlo simulation show the previously mentioned deviation from the fit-results on the undisturbed data. The deviation is increasing for larger σ irrespective of whether the sample is being heated up or cooled. If the temperature values of the outermost thermocouples are left unchanged, the differences are almost zero.

a characteristic behaviour in all simulations, statistical reasons cannot explain the shift. This leads to the conclusion that input data with a statistical error may yield shifted fit-results, which will be an issue as the measurement data always includes some statistical error. Thus, the effect will be investigated further in what follows.

Figure 3.18 depicts results for the $c\rho$ parameter of three different sets of Monte-Carlo simulations as well as the fit without artificial noise. During the simulations the standard deviation σ of the artificial noise added to the input temperatures has been varied. In the first set of simulations a single heat-pulse was used as signal for the heater power and in the second set of simulations the sample was cooled instead of being heated. In the third simulation set the heat pulse was used again, but the artificial noise was not applied to the temperatures assigned to the two outermost sensors T_1 and T_6.

As expected, it can be observed that the standard deviation of $c\rho$ is proportional to σ for all simulation sets. Furthermore, the results of the case where the sample is cooled and the case where the sample is heated do not differ significantly. The difference between the Monte-Carlo average and the fit-result from the simulation without noise rises with σ^2 for the first two sets of Monte-Carlo simulations. This difference is nearly the same for the first two simulation sets and becomes almost

zero in the third set of simulations, in which the artificial error was not applied to the two outermost temperature sensors. Also, the standard deviations of $c\rho$ are somewhat smaller as less input parameters are modified in this case.

The fact that the deviation will disappear if the thermocouples at the outer boundaries do not show noise explains why the fit-results for an actual measurement deviate from the real values due to noise. If the data for the boundary thermocouples is carefully smoothed using a moving average filter or another suitable method without changing the characteristics of the temperature development, the fitted parameters will not be shifted.

3.6.4 Measurement duration, sampling rate and informative value

Conclusions regarding the validity of the extracted fitting parameters may be deduced using the Monte-Carlo method. The waveform and the length of a heat pulse or cool pulse into the measurement bar has an influence on the accuracy achievable in a transient measurement with a fixed number of data points. Further knowledge about these effects may allow one to define an optimized measurement strategy which will minimize the number of measurements and therefore reduces measurement duration as well as wear effects of the relays used in the set-up.

The uncertainties of the fit-results are directly influenced by the maximum heater power. As the temperature differences along the sample increase linearly with the heater power, the corresponding standard deviations of the fitting parameters decrease. For a valid comparison throughout a simulation series this effect has to be considered. In an actual experiment the amplitude of the temperature must not be chosen too large as this may lead to errors due to radiation or non-constant material parameters. Thus, a compromise has to be made.

In a first step the influence of the steepness of a heat ramp was tested. The maximum power of the ramp was kept constant as well as the temperature sampling rate and the total number of samples. The heater powers and the results of the simulations are depicted in figure 3.19. If the ramp is very steep, the temperatures do not follow this increase due to the finite thermal diffusivity of the heat flux sensors and the sample. Thus, in these cases, the fit-results and the Monte-Carlo results are nearly constant. For less steep ramps the uncertainties begin to increase, because then the average temperature differences begin to decrease. If the slope is too low for the sample to reach a steady state, the standard deviations are further increasing until the errors are too large to allow the fitting algorithm to converge. This leads to the conclusion that if a single heat step is being used as input waveform for the heater power, the step should be as steep as possible. Additionally, the thermal diffusivity of the heat flux sensors should be small enough to not significantly limit the speed of the temperature rise.

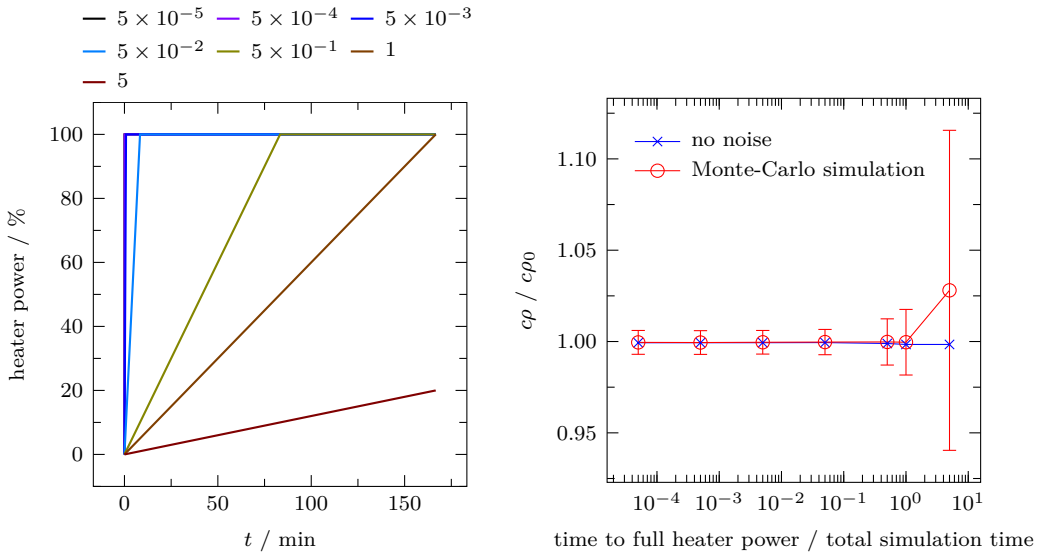

(a) (b)

Figure 3.19: The results of a Monte-Carlo simulation for single steps of the heater power with different steepnesses: the heater powers are depicted in (a). (b) shows the corresponding mean values and the standard deviations of the extracted $c\rho$ normalized to $c\rho_0$ as a function of the ratio of rise time to full heater power and total simulation time. For fast heat steps the simulation results are almost constant, as the system hardly follows the temperature excitation. An increase of the uncertainty of $c\rho$ can be observed only for lower steepnesses.

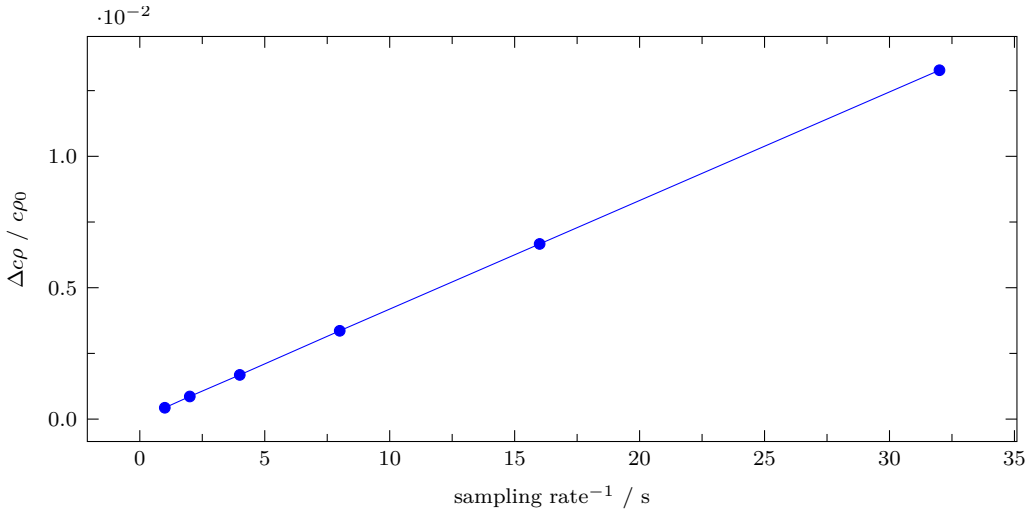

Figure 3.20: The Monte-Carlo simulations for a single heat step suggest a reciprocal relationship between the uncertainty of all fit parameters and the sampling rate. This relationship is here shown for $\Delta c\rho$.

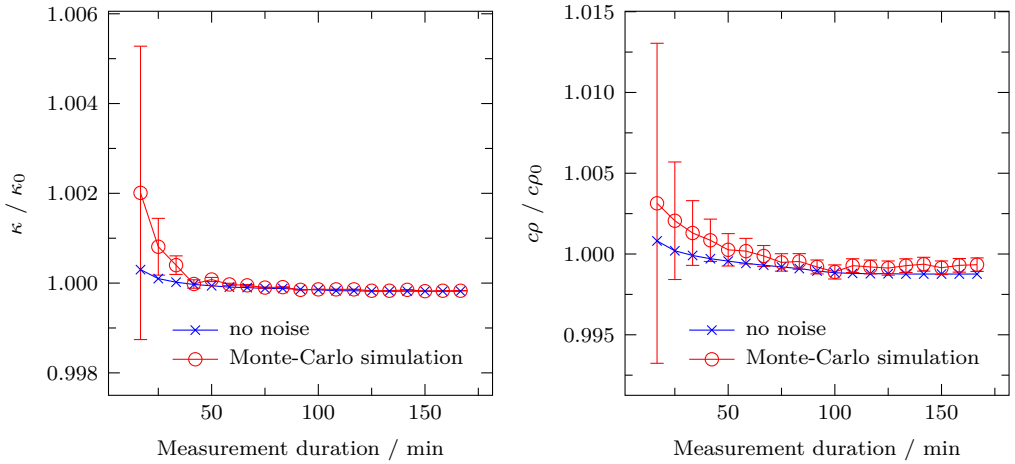

(a) (b)

Figure 3.21: The results of the Monte-Carlo simulations for different simulation durations using a single heat step show a steep decrease of the uncertainty of κ which after 6,000 s is nearly constant. This shows that after a certain time nearly no additional information can by gained, as a steady state has been established. The uncertainty in $c\rho$ shows almost the same behaviour.

Figure 3.20 depicts the influence of the measurement sampling rate on the standard deviation of the $c\rho$ parameter. $\Delta c\rho$ shows a reciprocal relation to the sampling rate and the same relation holds for the uncertainty of the κ parameter of the sample. For the simulation the input data, generated with Comsol in a high time resolution, was reduced by deleting evenly distributed sets of data.

Since there is no need for further sampling if no additional information can be obtained, the measurement time following a single heat step is also of interest. The simulations for different measurement durations, shown in figure 3.21, demonstrate that there are only very small changes of the standard deviations of the parameters $c\rho$ and κ after an equilibrium state is reached. The same holds for the deviations between Monte-Carlo simulations and the fits on the undisturbed data. This might seem contradictory to the fact that the total number of data points is still rising. However, as only the steady-state data is remeasured, only the steady-state information is duplicated and less disturbed by the artificial noise. This results in very slightly decreasing standard deviations for κ, as κ is mainly derived from the steady-state information. $c\rho$ instead is almost entirely determined by the dynamic part and should hardly be influenced if the steady-state data become more precise. However, the information for $c\rho$ also depends on the thermal diffusivity of the sample, thus, a more accurate measurement of κ subsequently leads to slightly more precise values of $c\rho$.

The findings that measurements in different states of the experiments have different informative value per data-point may be used for decreasing the sampling rate and thus reducing measurement data as well as minimizing stress on the relays in the set-up while preserving the accuracy of the measurement. The strategy to optimize the informative value per data-point comprises sampling at a high rate when the temperatures change fast and at a low rate for slowly changing temperatures.

3.6.5 Periodic heating

The results of the previous investigations show that mostly heat flux changes lead to informative gain in transient measurements. Since the maximum heat flux cannot be increased arbitrarily due to radiation issues a periodic heating, very similar to the Ångström method, may turn out to be advantageous. The Ångström method, however, relies only on the temperatures along the sample and does not employ heat flux sensors. Thus, only the thermal diffusivity of a sample can be determined. In contrast to the Ångström method the heat flux sensors surrounding the sample in our method enable the measurement of both, thermal conductivity κ and volumetric heat capacity $c\rho$ simultaneously.

Apart from the larger informative value an additional difference between non-periodic and periodic transient measurements with the ZT-meter is that the steady state as starting point is not a prerequisite. Instead, the measurement already may be started after a settling time, when the temperature oscillations behave uniformly. The numerical simulation requires the temperature distribution throughout both, the sample and the heat flux sensors, at the time of the initialization. Thus, for such measurements, the temperature data is extended periodically in a first evaluation step. A steady-state is assumed at the initialization and the simulation is executed several times on the same periodic input data, until the temperature oscillations become uniform. Eventually, a correct starting point for the simulation is established and the usual calculation procedure as described in the previous section can commence. The periodic extension of the input data has to be carried out very carefully, as the measurement sampling rate is not always constant and the length of a measurement is not necessarily a multiple of the cycle length. In this case the data has to be interpolated. Otherwise, the oscillations are not uniform.

First the influence of the waveform on the measurement efficiency was tested by comparing a simulation with a square wave as heater power signal and one using a sine wave. The standard deviations obtained for the two different signal forms did not differ significantly for κ as well as for $c\rho$, when the same power amplitude was used. However, in the real set-up the waveform at the sensor blocks tends to be sine-like due to the heat capacity of the heater and the resulting damping of the higher frequencies of the excitation. Only the sinusoidal waveform is discussed and used in the experiments with periodic excitation in what follows.

In contrast to measurements with a single switching of the heater power in which the information gain tends to zero when the steady state is approached, periodic

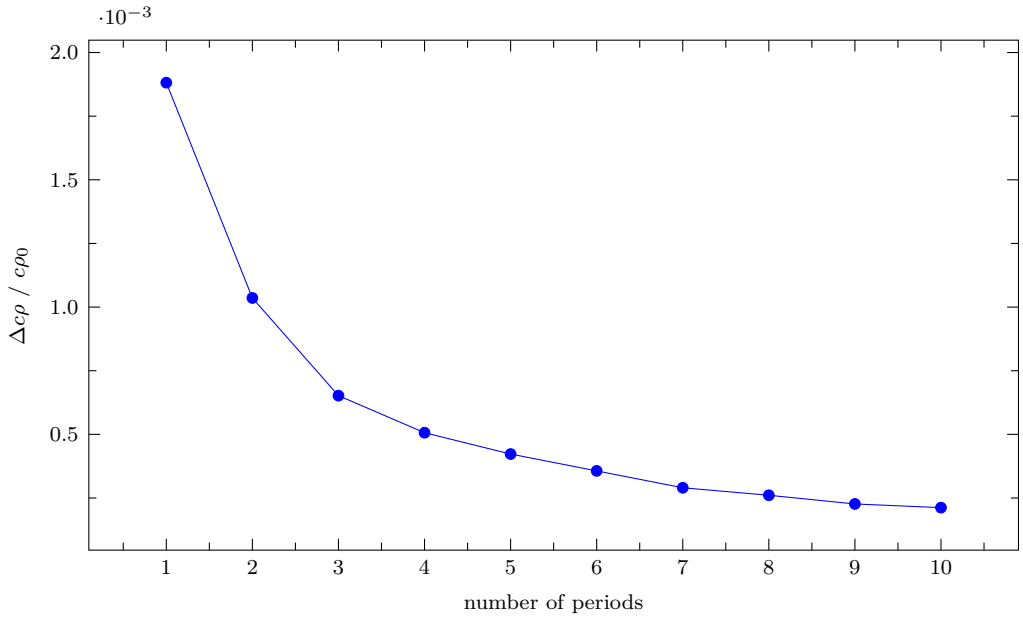

Figure 3.22: In contrast to measurements with only a single switching of the heater power the periodic excitations lead to a continuous gain of information. This results in a smaller uncertainty of the deduced variables for larger measurement durations, here shown for the $c\rho$ parameter. The same applies for κ.

measurements yield a continuous refinement of the results with increasing duration of the measurement. The heat flux alternation is particularly beneficial for the determination of $c\rho$. The κ parameter benefits indirectly from this. Figure 3.22 shows the reciprocal relationship between the standard deviation of $c\rho$, obtained from Monte-Carlo simulations, and the number of periods which had been simulated.

An example for temperature distributions in the sample and the heat flux sensors during a periodic measurement is shown for different phases of the heat excitation in figure 3.23. The waveform of the heat excitation at the left boundary is a sine function, the temperature at the right boundary was fixed at 273.15 K. The decreasing distance between the maximal and minimal temperatures (dotted lines) visualizes that the amplitudes of the oscillation are increasingly attenuated with larger distances from the heater. In order to obtain information from the measurement by phase and attenuation evaluations, the penetration depth of the thermal waves has to be large enough to reach the end of the set-up. The average temperatures (dashed line) follow an equivalent steady-state distribution, thus the value of κ could be evaluated without the finite difference model by employing a steady-state evaluation method. However, the thermal diffusivity cannot be obtained with a simple analytic model. The evaluation methods for the Ångström method are also not suitable, as the sample geometry does not fulfil the requirement of being thin and long enough

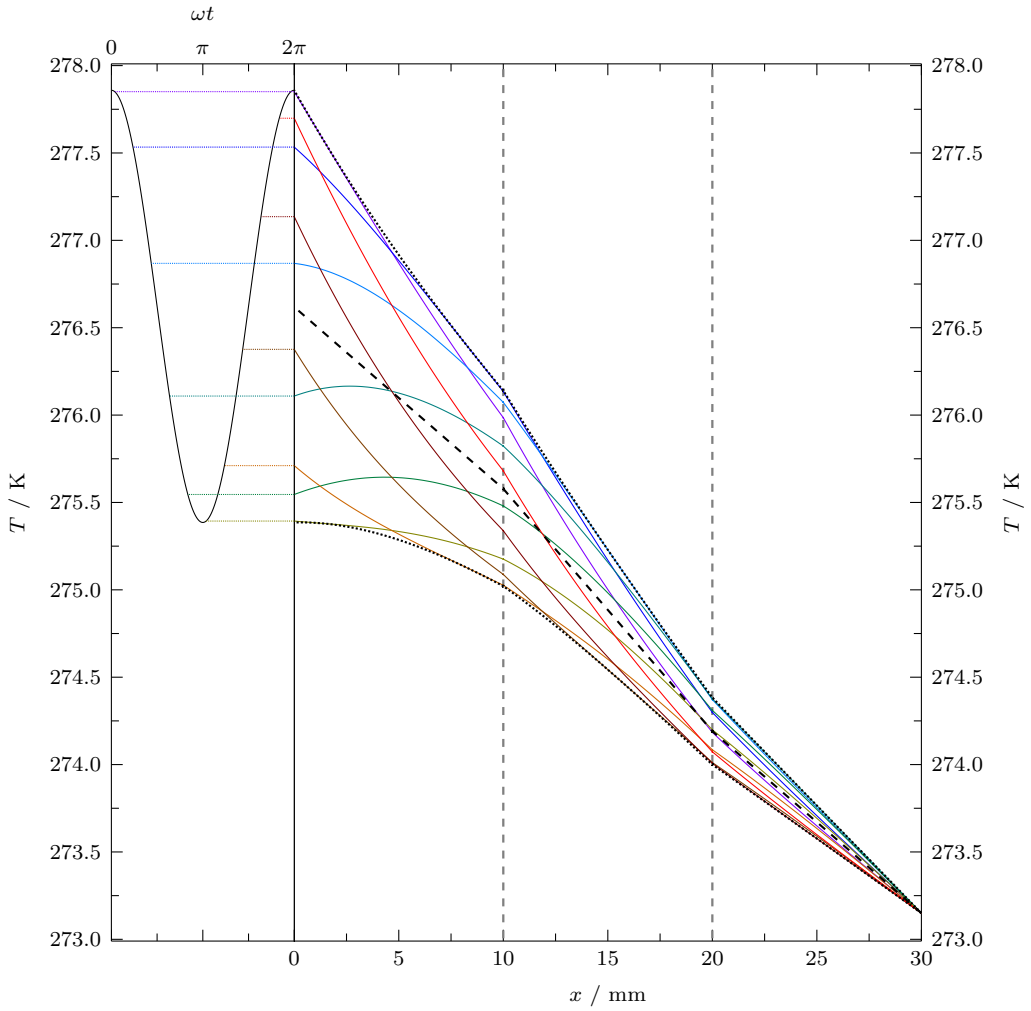

Figure 3.23: The figure shows the temperatures of the heat flux sensors and the sample, plotted as a function of position for different times in a simulation with periodic heating. The heater is placed on the left side while the temperature of the right side is kept constant. On the left side the time dependence of the temperature of the boundary between heat flux sensor and the heater is plotted. The dashed lines show the average temperatures, resulting in a position dependence which can be evaluated in a similar fashion than those obtained by the steady-state methods. The minimum and maximum temperatures are plotted as dotted lines visualizing the amplitudes of the oscillation. Their difference decreases exponentially in their respective material regime.

for the thermal waves not to be reflected or dissipated at the end of the bar or at the interfaces between sample and sensors. A modification of a more advanced evaluation method such as the one presented in Ref. 48, which takes reflections into account, might lead to correct results. Furthermore, no evaluation approach for Ångström's method is suitable for inhomogeneous bars such as the sample-sensor arrangements in the ZT-meter.

The attenuation of the thermal waves in the heat flux sensors and the sample strongly influences the accuracy of a measurement. However, the attenuation itself depends on the boundary conditions of the experiment. As the analytic investigation of the whole heat flux sensor–sample arrangement is very complicated, a simpler model will be employed in the following. The heat equation is solved for a homogenous one-dimensional bar, which is heated and cooled at $x = 0$ to reach a periodic boundary temperature of $T(x = 0, t) = \cos(\omega t)$, with ω being the angular frequency of the oscillation. For the boundary condition of the other side of the medium three different cases are analyzed. Detailed derivations of the solutions can be found in appendix A.

In the first case the medium is assumed to be semi-infinite leading to the boundary condition

$$\lim_{x\to\infty} T(x,t) = 0. \tag{3.28}$$

The solution for $T(x,t)$ in this case is given by:

$$T(x,t) = e^{-x\sqrt{\frac{\omega}{2D}}} \cdot \cos\left(\omega t - x\sqrt{\frac{\omega}{2D}}\right). \tag{3.29}$$

This shows that the amplitude of the thermal wave is attenuated exponentially with increasing distance to the heated boundary. The inverse of the decay constant $x_0 = \sqrt{\frac{2D}{\omega}}$ is called thermal penetration depth. Furthermore, $2\pi x_0$ denotes the wavelength of the wave.

The other two boundary conditions both consider a finite medium of length l. In one of them a Dirichlet boundary condition is applied with $T(l,t) = 0$. For the other case the medium is considered to be thermally isolated from the environment at $x = l$, leading to the Neumann boundary condition

$$\left.\frac{\partial T}{\partial x}\right|_{x=l} = 0. \tag{3.30}$$

For $l >> x_0$ the solution for the Dirichlet as well as the Neumann boundary conditions are equal to the case of the semi-infinite medium. If the thermal penetration depth, however, approaches l, the wave will be reflected in case of the Neumann boundary condition and dissipated in case of the Dirichlet boundary condition, leading to differences of the three temperature distributions at the boundary close to $x = l$. For all three types of boundary conditions, the temperature distribution

becomes a linear function between the temperatures at the boundaries, if x_0 is large compared with l. However, the slopes are very different. Figure 3.24 depicts the temperature maximum as function of x for the three sets of boundary conditions and different values of x_0.

As mentioned earlier an analytic description of the complete arrangement of heat flux sensors and the sample is rather complicated. One of the reasons is that reflections of the thermal waves at each boundary have to be considered. The approximation using a uniform medium shows the importance of the type of boundary for the measurement especially for large x_0 as a result of low frequencies or high thermal diffusivities. Due to the large diffusivity of the copper around heater 2 and the good coupling to the coolant the boundary condition at the end of the heat flux sensor in the real set-up is considered to be mostly of Dirichlet type. However, a small reflection of the wave cannot be excluded entirely.

As in the ZT-meter the sample is only heated, the temperature excitation at the heated boundary has an offset leading to a steady-state temperature distribution being added to the periodic one. This offset enables the measurement of κ, whereas the dynamic component of the temperature excitation allows one to determine D. As the maximum temperature differences inside the set-up are constrained due to radiation effects, it is essential to understand the interplay between the dynamic component and the static component of the temperature signal. Furthermore, the boundary temperature at the interface between the heater and the heat flux sensor is not controlled directly during the measurements but rather the heat flux density at the boundary. When using periodic heating, the heat flux density q from the heater into the heat flux sensor can be described by:

$$q(t) = A_{\text{q, periodic}} \left(\cos(\omega t + \phi)\right) + A_{\text{q, steady}}, \tag{3.31}$$

where $A_{\text{q, periodic}}$ is the amplitude of the heat flux oscillation, $A_{\text{q, steady}}$ is an offset value equal to or larger than $A_{\text{q, periodic}}$ and ϕ is a phase shift. If the heater were replaced by a Peltier element, $A_{\text{q, steady}}$ would assume lower values and q would take negative values. The heat flux density is proportional to the gradient of the temperature at the boundary:

$$q(t) = -\kappa \frac{\partial T(x,t)}{\partial x}\Big|_{x=0}. \tag{3.32}$$

As the exact analytic expression for $T(x,t)$ is unknown, the solution of the heat-equation for the uniform medium will be used as an approximation. For small thermal penetration depths the solution for the Dirichlet boundary condition, which is expected to be present in the set-up, is equal to the solution for the semi-infinite medium in Eq. (3.29). The offset of the heat flux will be considered by an additional term, interpolating linearly between the temperatures of the boundaries. For small

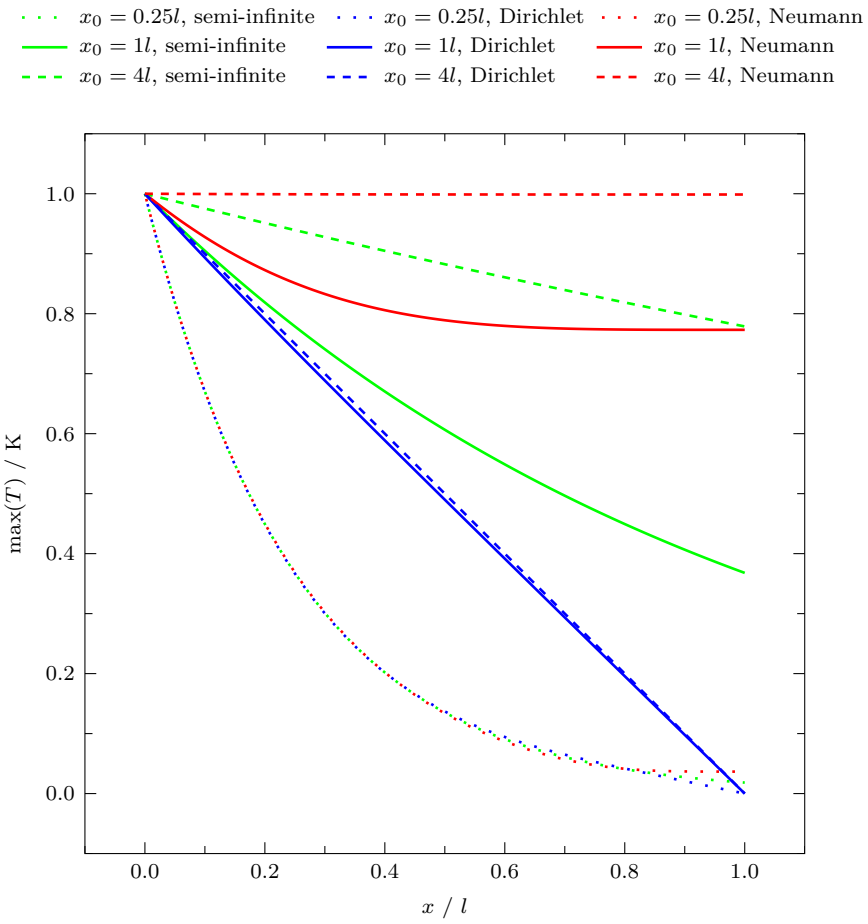

Figure 3.24: Temperature distribution along a one-dimensional, uniform medium with a periodic temperature excitation on the left side and three different boundary types on the right side. If the thermal penetration depth x_0 of the thermal waves, introduced on the left side, is small compared to the length of the medium l, all three boundary conditions lead to the same temperature distribution. For larger x_0 the solutions split up at $x = l$ and begin to diverge.

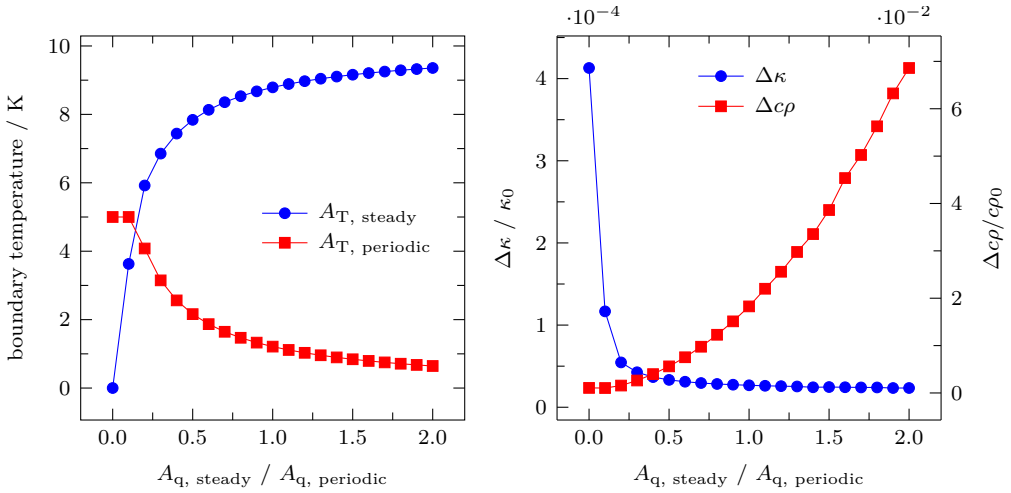

Figure 3.25: Figure (a) depicts the static offset $A_{\mathrm{T,\ steady}}$, as well as the amplitude of the oscillation $A_{\mathrm{T,\ periodic}}$ of the temperature at T_1 for different ratios of the heater power's amplitude and the heater power's offset. The absolute powers were chosen such that the maximum temperature difference in the input data is 10 K. The corresponding uncertainties for κ and $c\rho$, shown in (b), illustrate the opposing relationships between $A_{\mathrm{q,\ steady}}$ and $\Delta\kappa$ as well as $A_{\mathrm{q,\ periodic}}$ and $\Delta c\rho$ respectively.

thermal penetration depth x_0, the temperatures inside the uniform medium of length l are then expressed by:

$$T(x,t) = A_{\mathrm{T,\ periodic}} e^{-x\sqrt{\frac{\omega}{2D}}} \cdot \cos\left(\omega t - x\sqrt{\frac{\omega}{2D}}\right) + A_{\mathrm{T,\ steady}}(l-x) + T_0. \quad (3.33)$$

$A_{\mathrm{T,\ periodic}}$ is the temperature amplitude of the oscillation and $A_{\mathrm{T,\ steady}}$ the difference between the average temperatures at both boundaries. T_0 states the temperature at $x = l$. Inserting Eq. (3.33) into Eq. (3.32) leads to:

$$q(t) = \underbrace{-\kappa A_{\mathrm{T,\ steady}}}_{=A_{\mathrm{q,\ steady}}} \underbrace{-\frac{\sqrt{2}}{x_0}\kappa A_{\mathrm{T,\ periodic}}}_{=A_{\mathrm{q,\ periodic}}} \cdot \cos\left(\omega t \underbrace{-\frac{3}{4}\pi}_{\phi}\right). \quad (3.34)$$

Thus, a given ratio $A_{\mathrm{q,\ steady}}/A_{\mathrm{q,\ periodic}}$ results in a ratio of $A_{\mathrm{T,\ steady}}/A_{\mathrm{T,\ periodic}}$ which depends on the measurement frequency and the thermal properties of the sample. The absolute values of $A_{\mathrm{T,\ steady}}$ and $A_{\mathrm{T,\ periodic}}$ strongly influence the uncertainty of a measurement with regard to κ and $c\rho$ respectively. The interplay between the parameters is shown in figure 3.25. Simulations for various $A_{\mathrm{q,\ steady}}/A_{\mathrm{q,\ periodic}}$ ratios have been conducted and the resulting boundary temperatures T_1 at $x = 0$

have been obtained. The heater powers were chosen such that the difference between the minimum temperature and the maximum temperature in the input data was 10 K. Additionally, a Monte-Carlo simulation yielded the corresponding uncertainties for the κ and the $c\rho$ parameters, which behave inversely to the respective amplitudes $A_{\mathrm{q,\ steady}}$ and $A_{\mathrm{q,\ periodic}}$. The resulting uncertainties show that it might be beneficial to implement a Peltier element for sample cooling to achieve $A_{\mathrm{q,\ steady}}/A_{\mathrm{q,\ periodic}}$ ratios of below one.

During a measurement the penetration depth can be controlled by adjusting the frequency of the periodic excitation. For constant amplitude of the heater power and varying frequency, low frequencies f lead to higher amplitudes and larger penetration depths of the thermal waves. On the other hand at high f the thermal penetration depths may become too small for the thermal wave to reach the second heat flux sensor. At low frequencies the heater oscillation period increases as does the time required for the temperature oscillation throughout the sensor-sample-sensor arrangement to become uniform. Furthermore, since at low frequencies the temperature amplitude increases, uncertainties due to radiation become larger. A compromise between the two extremes which yields a maximum of information has to be found. To further investigate the influence of the heater frequency a set of Comsol simulations was used as input parameters for Monte-Carlo simulations. To remove the effect of rising amplitudes the heater power was adapted such that the upper sensor always reaches the same maximum temperature. The simulation results are shown in figure 3.26.

The material parameters κ and $c\rho$ are shown as a function of $\sqrt{1/\omega}$, which is roughly proportional to the thermal penetration depth x_0, defined above. The exact thermal penetration depth, however, is difficult to calculate, since the thermal diffusivities D change at the interface between the heat flux sensor and the sample. At low penetration depths, and thus high frequencies, the situation is comparable to a steady-state condition. The thermal waves do not propagate very deep into the sample and mainly the steady state component, arising due to the offset of the temperature excitation, is being measured. Thus, the informative gain regarding $c\rho$ is low while it is high for κ. With larger oscillation period the amplitude of the dynamic component rises and the mean temperatures are decreasing in relation as a result of the 10 K limitation. Since the uncertainty of κ also influences the determination of $c\rho$, at a certain point $\Delta c\rho$ starts also to rise for higher penetration depth. Other reasons for the increase of $\Delta c\rho$ at very low frequencies are the decreasing phase differences between the temperatures of the thermocouples and that the heat oscillation only penetrates into heat flux sensor 1 and does not reach the actual sample.

To conclude the discussion of the influence of the heat waveform on the measurement results of the ZT-meter a number of different input signal combinations will be presented and their performance compared. All simulations were run over the same time-frame of 10,000 s and with the same sampling rate of 1 Hz for the temperature input data. Also, the differences between the minimum temperature and the maximum temperature were normalized to an equal range of 10 K to permit a

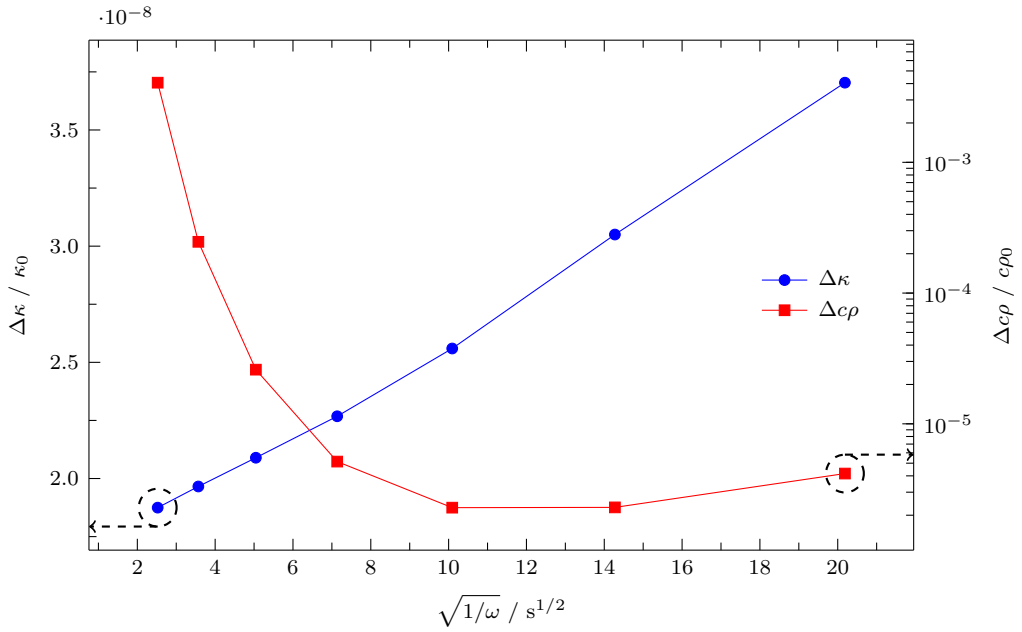

Figure 3.26: κ and $c\rho$ as a function of $\sqrt{1/\omega}$ for a sinusoidal heat stimulation. The frequency of the input signal changes the amplitude of the temperature oscillation and the thermal penetration depth of the thermal wave, and thus has a large influence on the measurement uncertainty.

valid comparison between the different waveforms. The first waveform is a simple step function (fig. 3.27a), whereas the second waveform consists of two steps with a break in between (fig. 3.27b). This is followed by a simulation with a sinusoidal heater power, starting after the temperature oscillations became uniform (fig. 3.27c). The next two waveforms used sinusoidal heating and cooling at both ends of the measurement bar, one with both ends in anti-phase (fig. 3.27e) and the other in-phase (fig. 3.27d). Finally, a sine function was applied as heater input but this time a steady state had been used as starting point (fig. 3.27f).

The results of the fits for κ and $c\rho$ are shown in figures 3.27g and 3.27h. For most types of input waveforms the standard deviations and the deviations of the Monte-Carlo averages from the exact value are relatively small for κ. In the case of $c\rho$ the periodic sine heating exhibits the smallest standard deviations while the step-wise heating shows larger standard deviations and absolute deviations. This is expected as the measurement takes mostly place in the steady-state regime.

The simulations in which both ends were heated and cooled show large deviations between the average results of the Monte-Carlo simulations, the fit-results for the undistorted data, and the original values for κ_0 and $c\rho_0$. If both ends of the sample are heated in-phase, no net-heat flow through the sample occurs resulting in a constant average temperature along the sample. As the gradient of the average

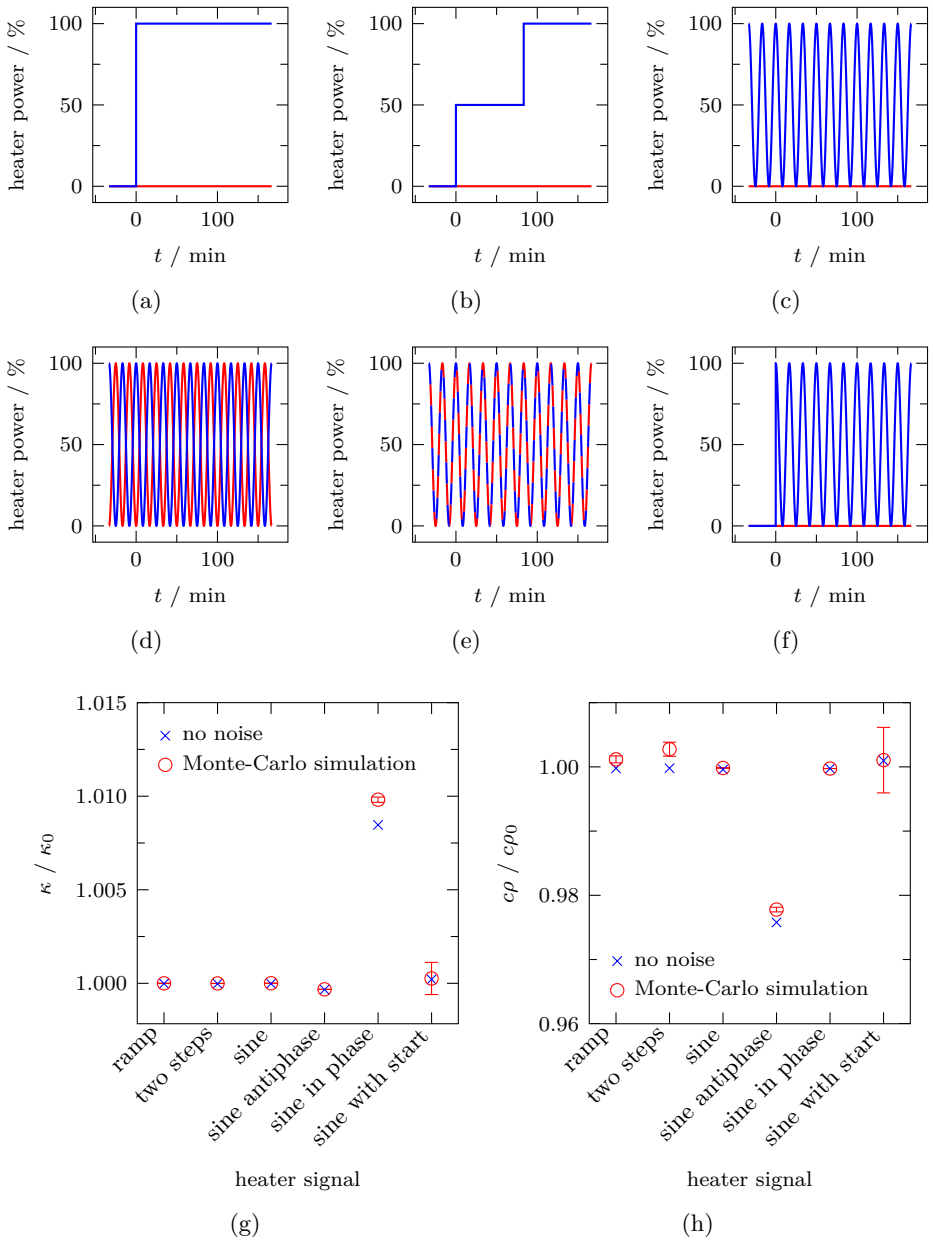

Figure 3.27: Comparison of different waveforms as heater inputs for the transient measurement mode: (a) ramp; (b) two steps; (c) sine; (d) sine antiphase; (e) sine in phase and (f) sine with start. The uncertainties were determined with Monte-Carlo simulations and the simulations using the sine waveform as heater input show the smallest errors for both κ and $c\rho$ in (g) and (f), respectively.

temperatures is important for the determination of κ, the in-phase heating mode results in a less certain knowledge of κ. When using the opposite mode, heating in anti-phase manner, the heat flow through the sample is maximized but the phase shifts between the thermocouples are significantly smaller. As the phase shift is an important parameter for the determination of $c\rho$ this measurement mode leads to larger deviations from $c\rho_0$.

For the sine waveform with a steady state as starting point the uncertainty in both parameters is higher compared to the pure sine function. This behaviour is expected as the average temperature amplitudes over the whole time-frame are smaller in this case. The comparison between all waveform shows that the periodic measurement mode "sine" is favourable when using the transient mode to determine κ and $c\rho$ as it shows the lowest uncertainties and deviations from the original parameters κ_0 and $c\rho_0$.

3.6.6 Effect of the thermal properties of the sample on the measurement uncertainties

The thermal properties of the sample and the heat flux sensors have direct influence on the quality of the measurement results. As stated before, low thermal diffusivities lead to small penetration depths of the thermal waves. Also, the equilibration times needed to reach a steady state will be longer if the sample or the sensors show low heat conductivities and large heat capacities. Furthermore, the thermal conductivities of the components should be within the same order of magnitude. If the thermal conductivity of the sample is much lower than κ_{Sensor}, most of the temperature gradient along the measurement bar will be located inside the sample and vice versa. Thus, for very low ratios $\kappa_{\mathrm{Sensor}}/\kappa_{\mathrm{Sample}}$ the temperature difference along the sample cannot be measured, for very large ratios the determination of the heat flux by the sensors does not work properly.

Figure 3.28 shows the results of a series of Monte-Carlo simulations where a sine-like excitation has been used. The thermal properties of the sample were changed in two different ways. At first only the $c\rho$ parameter of the sample has been varied and, thus, the penetration depth of the thermal waves. In a second series, again the $c\rho$ parameter of the sample was varied while altering its κ parameter such that the thermal diffusivity D is kept constant. With the first series the impact of a change in the thermal penetration depth is investigated, while with the second series mainly the influence of different κ values for the heat flux sensors and the sample is studied. The results for the standard deviation of the κ parameter show that the change of only $c\rho$ does not lead to a change of the uncertainty of κ. However, if in addition κ of the sample itself is varied a minimum in the uncertainty is found for intermediate ratios of $c\rho$ to $c\rho_0$ and thus of intermediate ratios κ to κ_0 and κ_{sensor}. If the ratio between κ and κ_{sensor} is very small, the temperature gradient along the sample will be small and will be measured with a larger uncertainty. This is reflected by the larger standard deviations in this case. The same holds for large

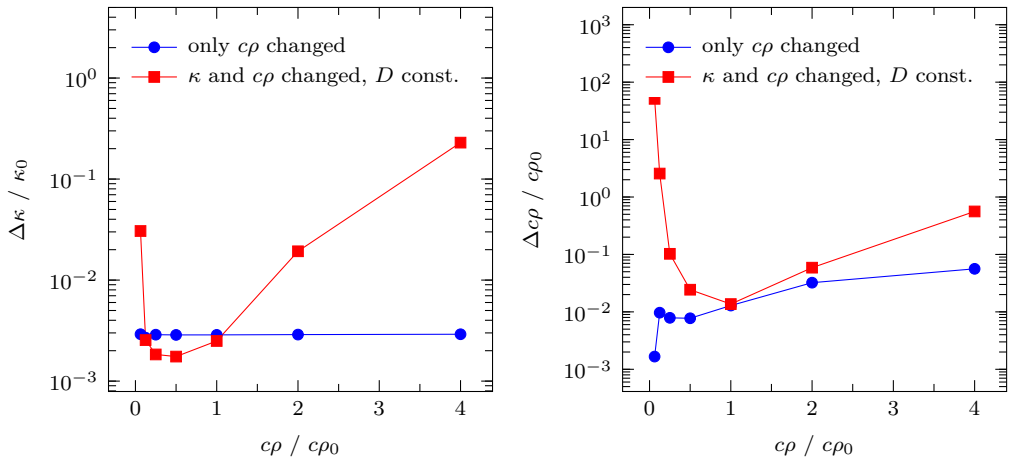

Figure 3.28: Standard deviations of κ and $c\rho$ for different ratios of $c\rho$ to $c\rho_0$ of the sample during periodic excitation. In one simulation series κ of the sample was kept constant at κ_0, in the other, the κ value was changed such, that the thermal diffusivity is constant. In the latter series, both uncertainties show a minimum, for the case where the thermal properties of the sample and the heat flux sensors are comparable.

ratios between κ and κ_{sensor}, where the temperature gradient along the heat flux sensors is small. The results for the standard deviation of $c\rho$ show a small decrease of the uncertainties if only the $c\rho$ parameter is decreased, probably due to the larger penetration depth. However, if the $c\rho$ parameter gets too small or too large, the simulations themselves will take more time, since the stability criterion in Eq. (3.16) needs to be fulfilled using smaller time steps. When both parameters, $c\rho$ and κ are varied while keeping D constant, a minimum for the standard deviation of $c\rho$ is found, again at intermediate values of $c\rho$. For low as well as large values the uncertainties increase strongly, since here the heat fluxes cannot be determined accurately. This also applies to the uncertainties of the κ value.

Thus, in order to achieve optimum measurement results, the thermal conductivities of the sample and the heat flux sensors should not differ too much. The ratios of the thermal heat capacities also show an influence on the results. This impact, however, is smaller and probably a result of the change of thermal penetration depth. The thermal penetration depth can be adjusted by changing the frequency of the exciting waveform. Thereby, a mismatch between the heat capacities of the sample and the sensors can be compensated.

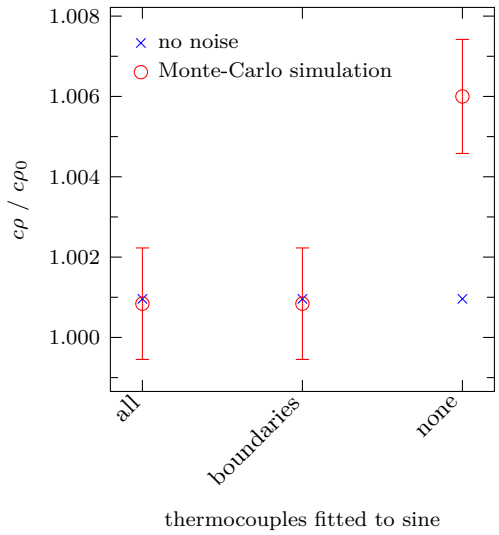

Figure 3.29: Comparison of the Monte-Carlo simulations using a sine function fitted to the input data of none, of the boundary thermocouples or of all thermocouples. The method reduces the deviation between the Monte-Carlo averages and the original values greatly as long as the boundary sensors are fitted. The standard deviations of the results are not changed.

3.6.7 Reduction of the temperature noise at the simulation boundaries

The absolute deviation which is seen in the results as a deviation of the average of the Monte-Carlo results from the fit of the undisturbed measurement, is also present in measurements with a periodic excitation. A simple moving average filtering of the boundary temperatures will improve the results, but can lead to a reduction of the temperature maxima and minima. In case of the sine heating a more suitable method is to make use of the condition that the temperatures at the thermocouples always evolve sinusoidally in time, by fitting a sine function to the temperature data of the thermocouples. The fit-data can then be used in the simulation. Figure 3.29 shows a set of Monte-Carlo simulations, in which the data of all thermocouples, only of the outer thermocouples, and none of the thermocouples, respectively, was fitted to a sine and then used as input in the numerical model. The plot shows that neither standard deviation nor bias are different for the first two cases. However, both fit methods show a greatly reduced deviation compared to the third case, where the distorted data was used in the simulation directly. Thus, the method of fitting the known waveform function to the measurement data of the thermocouples prior to conducting the rest of the evaluation appears to be a good way to reduce the deviation of the fit-results, which is introduced by noise on the boundary temperatures.

3.6.8 Considerations on the sample geometry

In the following the influence of the sample geometry on the measurement accuracy will be discussed. The arrangement will be optimum if the cross-sections of the heat flux sensors are identical to the cross-section of the sample, since the assumption of one-dimensional transport is fulfilled best in this case. Cylindrical glass sensors with a radius of 6 mm are used in the present set-up. They possess the same dimensions and shape as the metal stamps used for fabricating the samples by hot compression moulding. However, there might be small deviations from the optimum sample geometry due to thermal expansion inside the moulding form resulting in a deviation of the sample radius from the ideal radius. Thus, the magnitude of this effect on the measurement results needs to be discussed.

If the sample has a larger radius than the sensors, two limiting cases need to be considered in terms of sample length. In case of a very short sample the transport path does not widen from the heat flux sensor to the sample radius before leaving the sample again (Fig. 3.30a). If the sample is very long compared with the width difference between heat flux sensor and sample, the portion of the sample in which the transport is not one-dimensional can be neglected (Fig. 3.30b). In the former case the measurement results will not be influenced by the sample width whereas in the latter case the thermal conductivity will have to be corrected by using the cross-sectional areas of the two cylinders. In real measurements these extreme cases will not occur and a correction of the obtained values for κ and $c\rho$ is fairly complicated and preferably avoided. Furthermore, if a broader sample has a much larger thermal conductivity than the sensors, the transport inside the heat flux sensors themselves is not one-dimensional anymore. This is also the case for samples with a much smaller radius than the sensors (Fig. 3.30c). As a consequence the heat flux in the sensors can strongly deviate from being one-dimensional and in most of these cases the deviations from the one-dimensional numerical model are too large for the fit algorithm to find a minimum of χ^2.

To further investigate the problem a set of two-dimensional, transient FEM simulations was performed. Different sample thicknesses, lengths and thermal conductivities were used and a sinusoidal excitation waveform has been chosen. The rotational symmetry of the cylinders representing the sample and the heat flux sensors permits the reduction of the dimensionality of the model from three to two dimensions. The temperature data of the FEM model was then fitted using the one-dimensional finite difference model and the parameters κ and $c\rho$ of the sample structure were extracted.

In figure 3.31a the obtained values for κ are plotted against the sample length for different sample radii. If the sample radius is identical to the sensor radius of $r_0 = 6\,\mathrm{mm}$, the correct results for κ are obtained. For very short samples and sample radii larger than the sensor radius the results also agree quite well with the nominal values and are only slightly overestimated. This changes for longer samples with larger radii than the heat flux sensors. Here the heat current in the samples

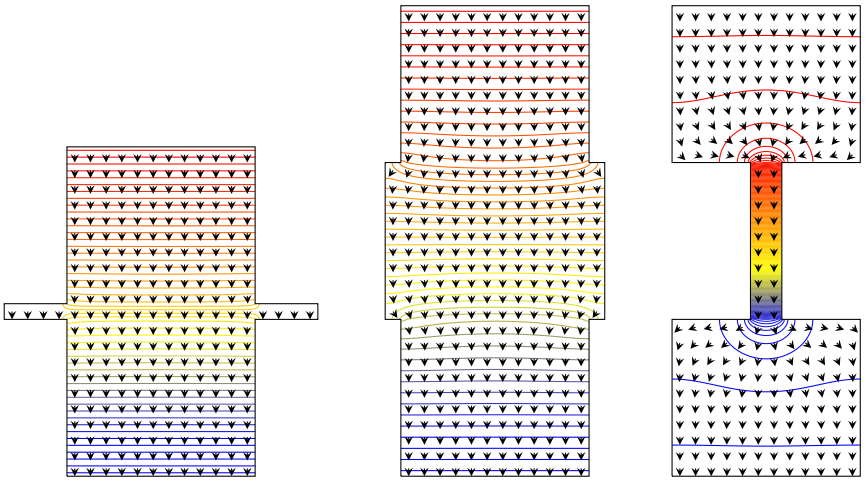

(a) (b) (c)

Figure 3.30: Examples of steady-state temperature distributions, shown by isothermal lines, and heat-flow directions (black arrows) for sample geometries where the sample width is not equal to the width of the heat flux sensors. As the numerical model used for the fits handles the heat transport only in one dimension, the fit-results are very sensitive to deviations from the optimum geometries.

spreads perpendicular to the measurement direction leading to higher values of κ than expected.

However, if the sample radius is smaller than the radius of the sensors, the transport inside the sensors deviates strongly from the one-dimensional model and cannot be fitted anymore. Only for $r = 5\,\mathrm{mm}$ the fit routine converged and the corresponding results for κ deviate from the original values for all sample lengths.

Figure 3.31b shows the same results corrected for the true sample cross-section. The geometry correction $\kappa_{\mathrm{corrected}} = \frac{r_0^2}{r^2}\kappa$ is valid only for samples which are much longer than wide. Consequently, the values converge to the correct value with increasing length. However, in a real measurement case using the current set-up the samples cannot be long enough for this model to be valid.

The fit-results for the $c\rho$ parameters are found in figure 3.31c and the ones corrected for the cross-section in figure 3.31d. In the latter figure a correction for the cross-section $c\rho_{\mathrm{corrected}} = \frac{r_0^2}{r^2}c\rho$ was used. For small deviations of the radius in both directions the corrected values are in good agreement with the nominal value. In all investigated cases the relative deviation for the corrected $c\rho$ is much smaller than the corresponding average relative deviation of κ. The explanation for this finding is that the periodic portion of the thermal transport does not have a forced direction and the waves propagate in all directions. This is in direct contrast to the stationary portion of the transport taking place between the heater 1 and heater 2. Due to

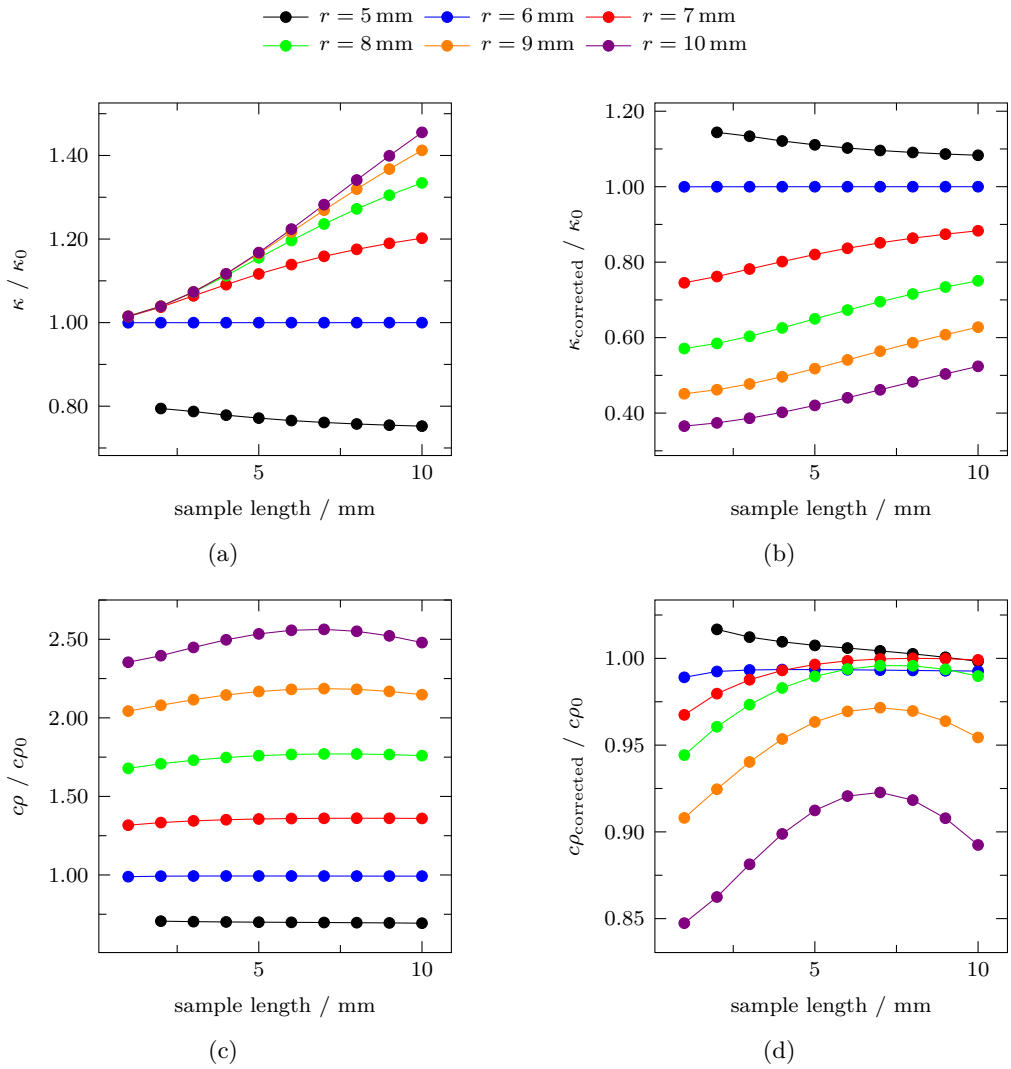

Figure 3.31: Fit-results of the numerical transient model for cylindrical samples of different widths and lengths. The results without geometry correction on the left-hand side diverge from the correct values for longer samples. On the right-hand side the same fit-results were corrected for geometry using a simple model. While the results for $\kappa_{\text{corrected}}$ are converging for longer samples, some of the $c\rho_{\text{corrected}}$-curves show a minimal deviation at a certain length. The diameter of the heat flux sensor was set to 6 mm in all calculations.

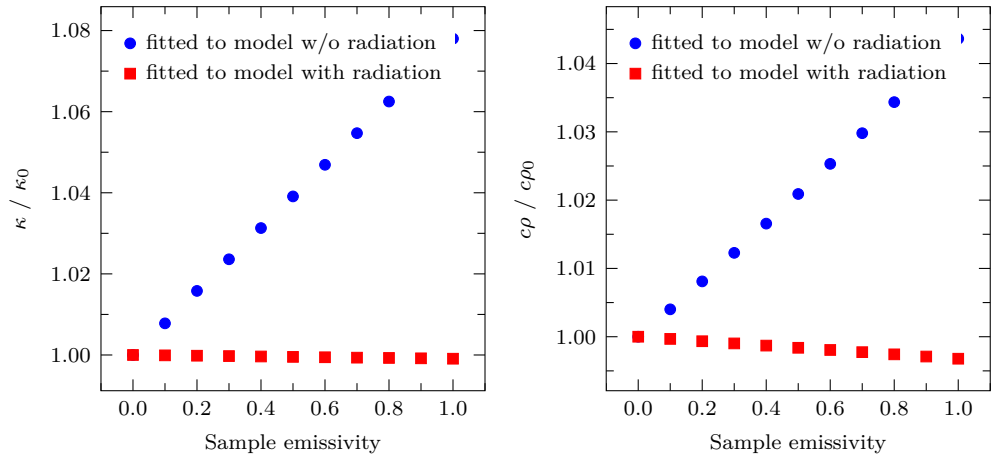

Figure 3.32: The fit-results of κ and $c\rho$ to a two-dimensional Comsol model with activated ambient radiation show good results when fitted to a model with the one-dimensional radiation approximation. Only for large sample emissivities the values for $c\rho$ are slightly underestimated. As waveform for the heat flux a sine input has been used.

the isotropic propagation of the heat waves more heat flows perpendicular to the regular transport direction and the measurement can be considered one-dimensional for shorter samples than it is the case for the stationary heat transport.

3.6.9 Effect of heat radiation on the measurement

It was proven that Ångströms method is mostly insensitive to radiation towards the ambient. To show that this is also the case for the presented numerical evaluation method heat radiation effects were also implemented into the model for the transient heat equation using Eq. (3.25). However, the exact emissivities of the sample and the sensors are often unknown. The implemented model is strictly one-dimensional and neglects the width of the sample. For a good estimation of the radiation effects they are being investigated in the following. A two-dimensional Comsol simulation with heat radiation between the boundaries of the sample and the ambient at a temperature of 273 K was used to generate temperature data. This was evaluated with the fit tool including heat radiation as proposed in Eq. (3.25) and with treating ϵ as a fit parameter. The results in figure 3.32 show large deviations of nearly 8 % for the obtained value of κ if the effect of heat radiation is not implemented in the fit model. The results for the fit-model with radiation are in much better agreement with the correct values, but underestimate the values for $c\rho$ as well as κ for larger ϵ slightly. This is due to the implementation in one transport direction only and the resulting negligence of the sample thickness, which would otherwise result in

a smaller radiative current. The cost of the additional fit parameter ϵ is that the uncertainty of κ in an additional Monte-Carlo simulation was found to be about 10 % larger for all ϵ. However, at the same time $\Delta c\rho$ decreased linearly with ϵ and ended up at a value of 14 % for $\epsilon = 1$.

3.6.10 Influence of the thermal contact resistance on the measurement

The thermal contact resistance between the heat flux sensors and the sample directly influences the measurement results of the ZT-meter. This could be circumvented by using thermometers inside the sample itself, as it is done in the Ångström method. Another possibility to eliminate the effect of the boundary resistances is to measure the surface temperatures of the sample e.g. with an IR camera, a method used in some laser flash analysis set-ups. However, for this approach the sample has to be coated to ensure that the emissivity coefficient is known and that the radiative power density can be converted into a temperature.

Since the thermocouples used in the ZT-meter are not inserted into the sample itself, the measured thermal resistance R_{thermal} includes the thermal interface resistance. R_{thermal} can be calculated from the thermal conductivity of the sample κ_{sample}, the total interface resistivity $\rho_{\text{interfaces}}$, the sample length l and the cross-section of the sample A:

$$R_{\text{thermal}} = \frac{l}{\kappa_{\text{sample}} A} + \frac{\rho_{\text{interfaces}}}{A} = \frac{l}{\kappa_{\text{measured}} A}. \tag{3.35}$$

On the other hand, the determined values for $c\rho$ are mostly independent of the interface resistances. The determination of $c\rho$ depends on the difference of the measured heat fluxes into and out of the sample as well as the corresponding temperature changes. These mechanisms are not directly influenced by the interface resistances. However, the total thermal diffusivity increases due to the interface resistances and the measurement uncertainty can increase as a result. Figure 3.33 shows a corresponding simulation of a transient measurement with a periodic input for varying interface resistivities $\rho_{\text{interfaces}}$. The obtained values for κ agree with those obtained with Eq. (3.35), while the values of $c\rho$ are nearly constant.

If the thermal conductivity of the sample or the thermal interface resistances are known, the fit-program can be used to determine the other value. However, for small interface resistances the current implementation with the FTCS scheme requires small time steps, otherwise oscillations will occur. Figure 3.34 shows a series of fits to the same sets of input data as before, but with a fixed value for κ. Instead, $\rho_{\text{interfaces}}$ and $c\rho$ were used as fit parameters. For very small values of $\rho_{\text{interfaces}}$ the fit did not converge towards the original value, as the FTCS implementation became

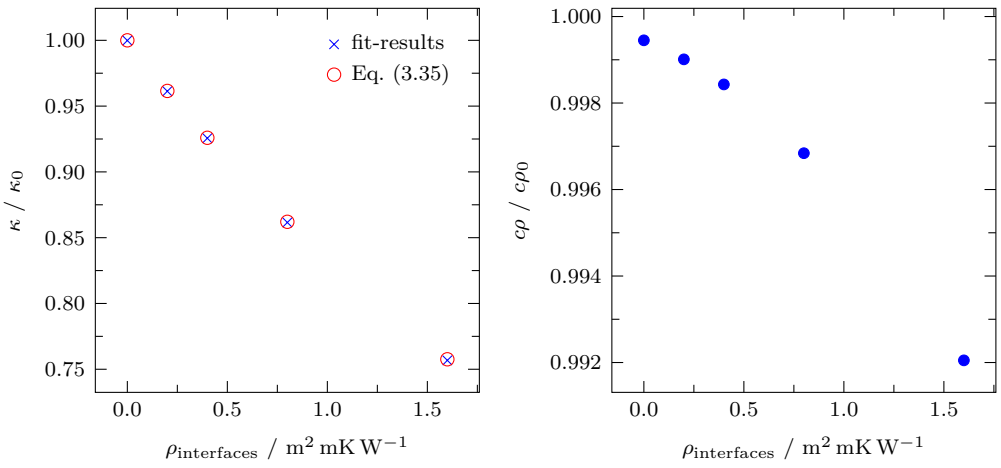

Figure 3.33: Fit-results of a simulation series with varying interface resistances $\rho_{\text{interfaces}}$ show that the ZT-meter measures too low values for κ if interface resistances are present. However, the determination of $c\rho$ is barely influenced in this case.

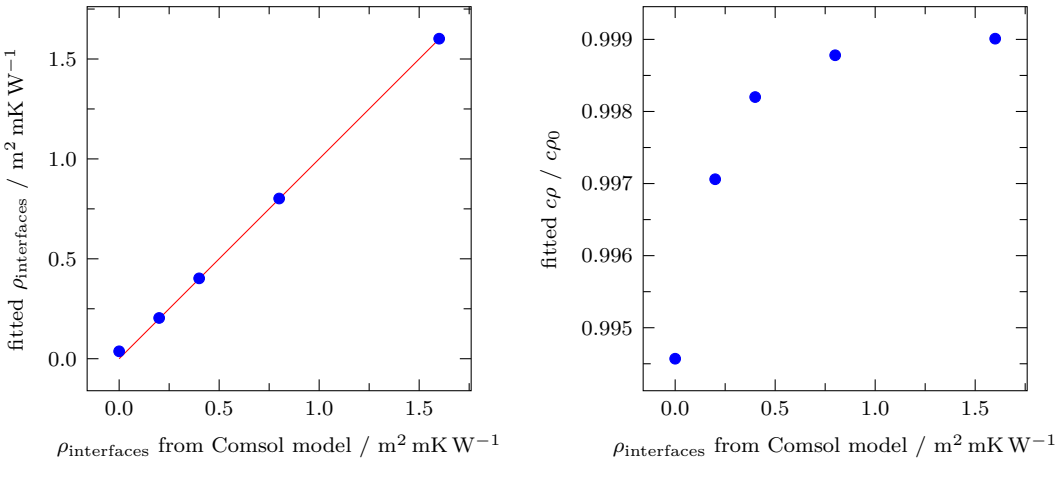

Figure 3.34: Fit of the numerical model with implemented interface resistances to the Comsol simulations: the interface resistance values (a) are in good agreement except for the simulation with the interface resistance being zero. The results for the $c\rho$ parameter are nearly constant. The current finite difference implementation with the FTCS scheme becomes unstable for small $\rho_{\text{interfaces}}$. Since the numerical errors are getting larger for decreasing $\rho_{\text{interfaces}}$, the deviations from $c\rho_0$ grow in this case.

numerically unstable. Also, the $c\rho$ values show a growing deviation from the original values $c\rho_0$ when the interface resistances decrease.

3.6.11 Transient measurements over large temperature ranges

The transient measurement mode has the potential to dramatically reduce the measurement times compared with common steady-state modes. However, in the cases shown before, either a steady-state at the beginning of the measurement has to be reached or the measurement has to be paused until all temperatures vary periodically. In the following an approach to avoid these waiting times is presented. Instead of increasing the base temperature step-wise, it is increased continuously. Thus, the material parameters κ and $c\rho$ of the heat flux sensors and the sample are always a function of temperature. In the other methods those parameters could be approximated as being constant during the periods of constant base temperatures. The implementation of the numerical model supports the use of temperature dependent parameters. However, the complete fitting of a measurement over a large temperature range in a single run of the current fitting procedure raises two problems. Since the overall measurement time is probably longer than the time needed for a single measurement step at a constant base temperature, the computation time for a single calculation of χ^2 rises, since more measurement time has to be covered. Moreover, if the thermal properties of the sample are described by a piecewise interpolation between several nodes, the number of fit parameters increases and, thus, the number of simulations needed to complete the fit procedure also increases. Therefore, a fit of the complete measurement is too complex from a computational point of view. Moreover, it also would not be very efficient since the respective values of κ and $c\rho$ are valid for a certain temperature range only.

Figure 3.35 describes an evaluation process which can be used instead and should yield better results. In a first step the input data is divided into several intervals p_n. For each interval the average sample temperature T_n is calculated. In a next step each interval is fitted to the numerical model assuming that κ and $c\rho$ of the sample are temperature independent. As a starting point for the simulations succeeding the first interval, the last temperature distribution of the simulation of the preceding interval is used. As a result, values for κ_n and $c\rho_n$ are obtained, each approximately valid in their respective interval p_n. The values might show a larger error due to the crude assumption of a constant κ and $c\rho$. Thus, in a third step each interval p_n is fitted again, now using temperature dependent values for κ an $c\rho$, which are piecewise linearly interpolated between κ_{n-1},κ_n, κ_{n+1} and $c\rho_{n-1}$,$c\rho_n$, $c\rho_{n+1}$ respectively. In this step only the values for κ_n and $c\rho_n$ are varied, while the neighbouring values remain fixed. This third step is executed several times until the resulting parameters converge self-consistently. The resulting curves can eventually be refined by adding intermediate grid points into the piecewise interpolation of κ and $c\rho$. However, if the number of grid points becomes too large, deviations due to uncertainties may be enlarged, since the number of measured temperatures for each κ or $c\rho$ point is too

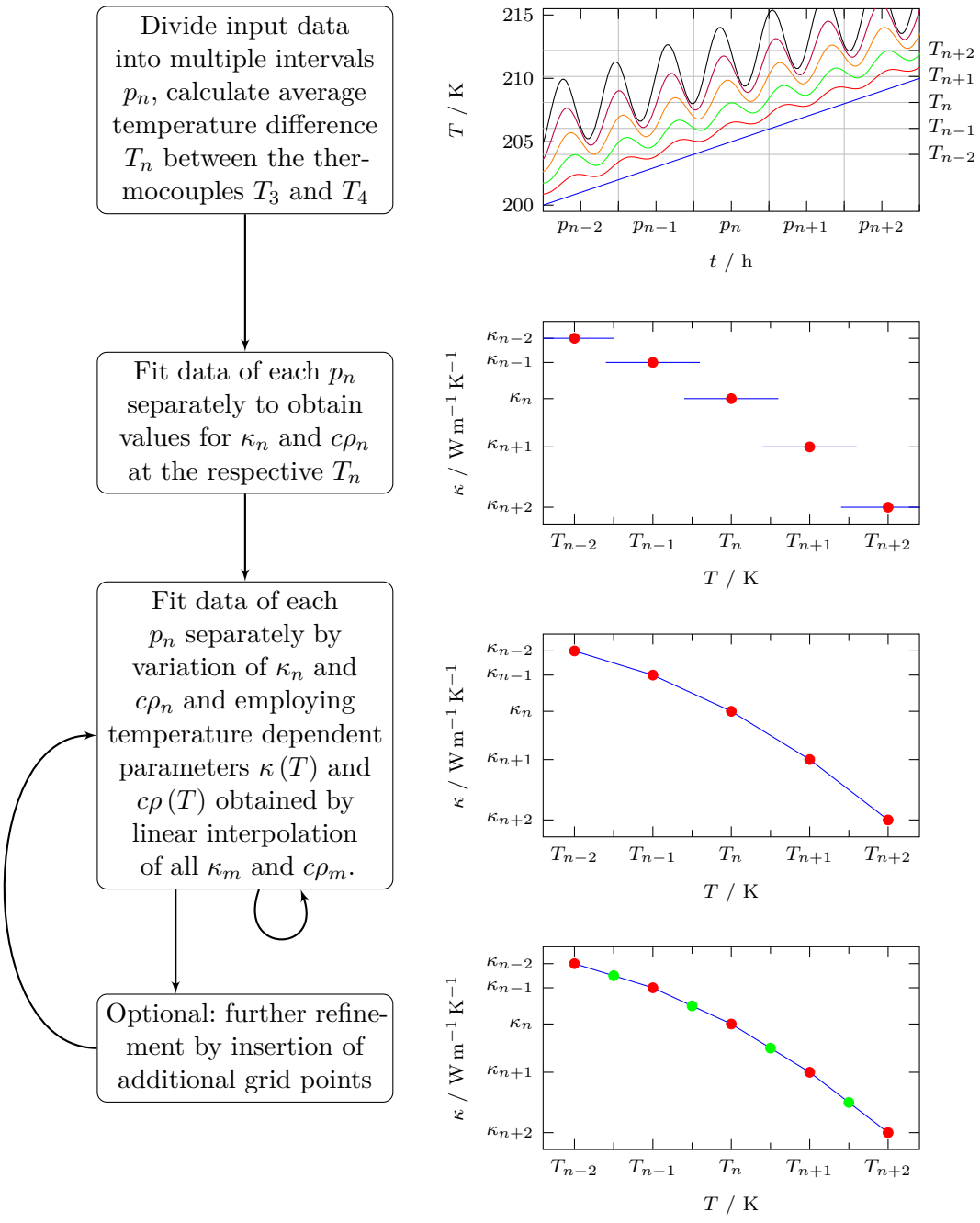

Figure 3.35: Flow-chart for the evaluation process for measurements over a large temperature range with temperature dependent thermal properties of the sample and heat flux sensor material.

low. After the insertion of additional grid points, the third step has to be executed again.

Figure 3.36 depicts the results of an evaluation process as it is described above. The input data has been generated using Comsol, with temperature dependent thermal properties of the sample and of the heat flux sensors. The thermal parameters of the sensors where presumed to be known in the evaluation. To improve the sensitivity towards the $c\rho$ parameter, a sinusoidal heater power was applied with heater 1. The base temperature was increased linearly from 100 K to 300 K. In figure 3.36a the temperatures of the six thermocouples are shown as a function of time. Figures 3.36b and 3.36c depict the fit-results for κ and $c\rho$, respectively, at different stages of the evaluation process. The results after the first fitting step, in which temperature independent κ and $c\rho$ were used show deviations from the original values k_0 and $c\rho_0$. In the following steps (step 2 – step 4), both parameters converge towards the original values.

The approach renders large savings in time possible since most waiting times are omitted and data are taken during the entire temperature sweep. An idea of the gain in speed of the measurement using the novel approach can be obtained by considering typical waiting times in the measurements discussed previously. In the steady-state measurements of this work 5 hours of waiting time were needed at each base temperature for the system to equilibrate, prior to actually taking data. In the transient measurement with sinusoidal heat excitation the waiting time, prior to taking data, at each base temperature was reduced to 3 hours. With the novel approach it can be entirely omitted. Furthermore, the continuous measurement allows for a finer temperature resolution without the necessity of additional waiting times.

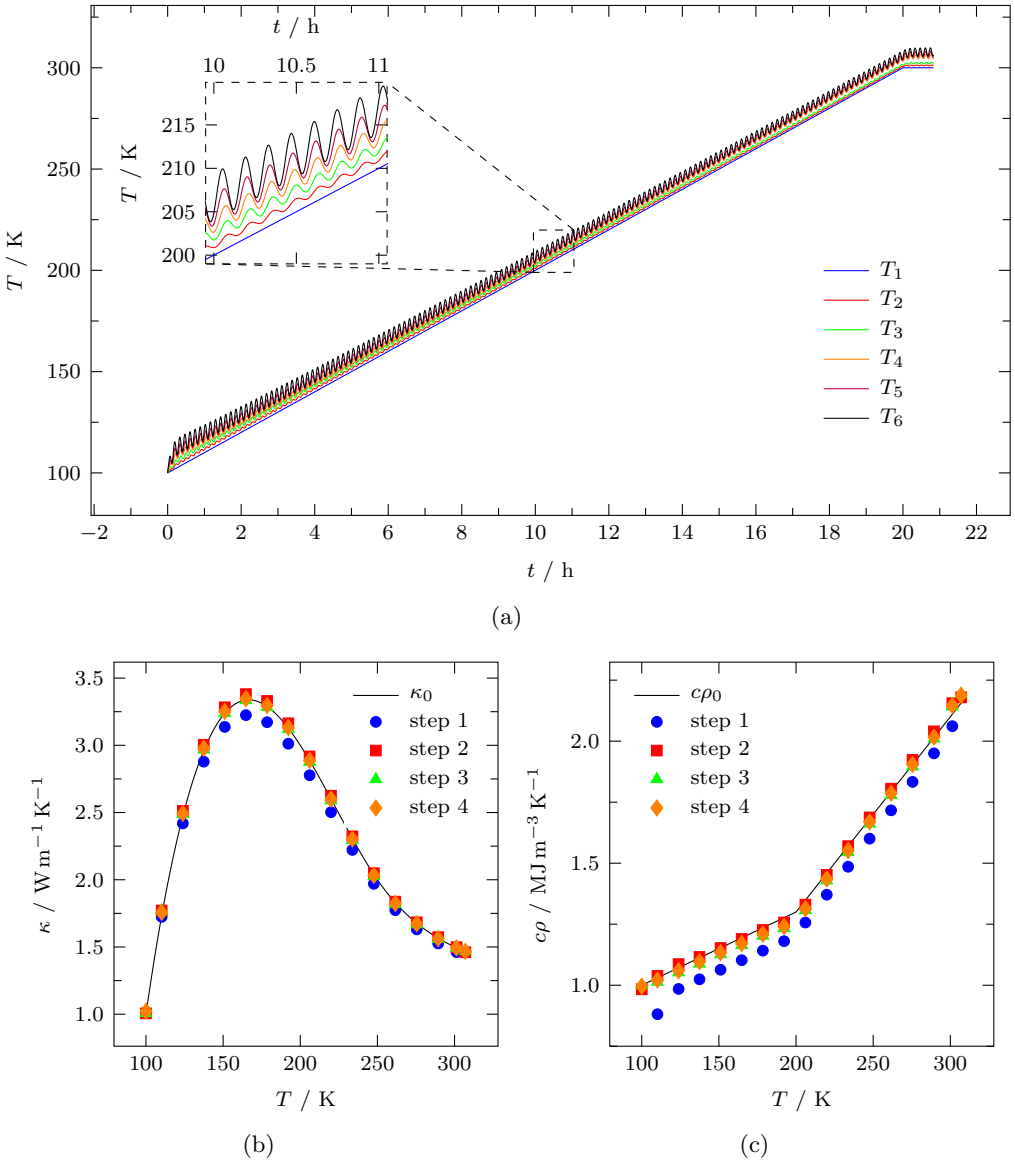

Figure 3.36: In (a) the simulated temperatures for a measurement without a constant base temperature are shown. (b) and (c) depict the corresponding results for κ and $c\rho$ of the sample obtained with the evaluation method shown in figure 3.35.

4 Calibration and first measurements

4.1 Thermocouples

Since the material composition of the wires used in thermocouples is subject to small variations, the measured thermovoltages can deviate slightly from the standard calibration curves for thermocouples found, for example, in Ref. 63. Thus, the thermocouples in the set-up need to be calibrated to enable precise measurements.

Several measurements without a sample, in which the temperature of the base plate was held at different temperatures for several hours, were conducted. The control mechanism for the guard-heater minimized the heat flux through the guard and consequently the heat flux through the heat flux sensors. Without a heat flux applied, the temperature differences between the thermocouples inside the heat flux sensors can be assumed to be zero. Of course, radiation effects and parasitic currents may cause deviations, but these are small, since all parts of the set-up are nearly at the same temperature. The temperatures for all thermocouples in the heat flux sensors where calculated for different temperatures of the base plate according to the tables found in Ref. 63. The average temperature was then used as reference value in the calibration of the different thermocouples.

To calculate a conversion function $U(T)$ from the thermovoltage U_{measured} to the temperature T_{sensor}, which is independent of the prevailing temperature in the laboratory, the temperature of the reference-point $T_{\text{reference point}}$ has to be considered. Eq. (2.3) directly leads to:

$$U(T_{\text{sensor}}) = U_{\text{measured}} + U(T_{\text{reference point}}). \tag{4.1}$$

The function $U(T)$ for a thermocouple is determined iteratively, by making a guess for $U(T_{\text{reference point}})$ and fitting the right side of Eq. (4.1) to a polynomial. This is repeated by using the obtained polynomial for the value of $U(T_{\text{reference point}})$, until $U(T)$ is not changed anymore. The order of the polynomial was four and has been chosen such that the function is well fit and no oscillations occur. To account for smaller local deviations in the thermovoltage, the difference between the measured

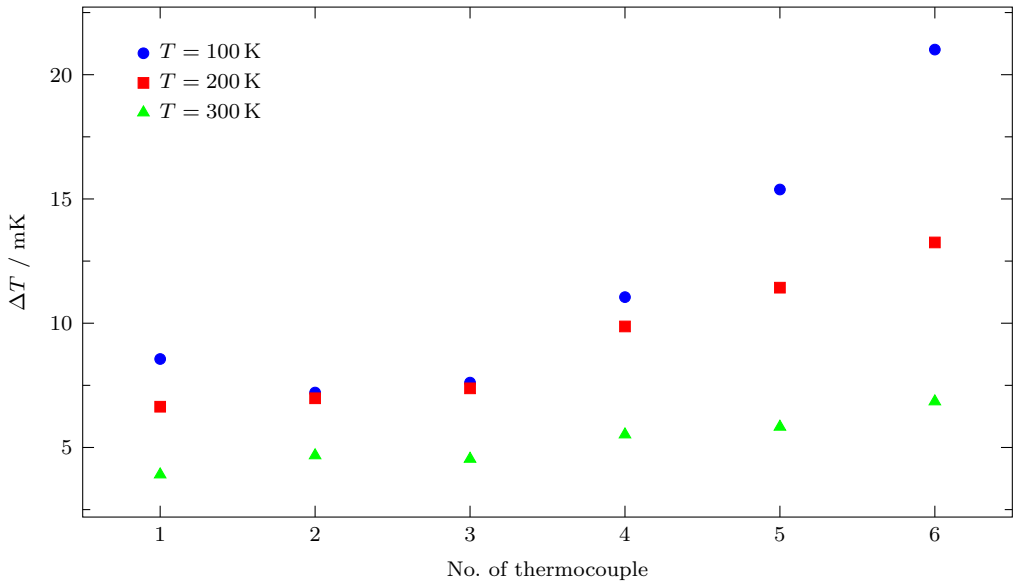

Figure 4.1: The figure depicts the noise of the thermocouples used in the set-up at different temperatures. It is larger for the outermost sensors, since they are, from a thermal point of view, closest to the temperature oscillations at the cold finger.

voltage and the respective data of the polynomial has been interpolated and added to the calibration table. Repeated calibrations showed a repetitive error of about 0.15 K. This can be mainly attributed to unstable temperature conditions in the laboratory, leading to temperature fluctuations of the reference point and along the thermowires outside the cryostat.

Figure 4.1 depicts the standard deviation of the temperature measured by the six thermocouples during a measurement. T_6 being next to the base plate shows the highest fluctuations. As stated before, boiling effects of the coolant lead to temperature oscillations at the base plate. Those have a larger impact at low temperatures, since, in this case, the heat capacities of the materials used are usually smaller, and the oscillations are less filtered by the copper. The temperatures at T_1 are also influenced, as the thermal waves are transported via the copper shield to the heat flux sensor. Inside the sample the temperature fluctuations are damped further and smaller standard deviations are observed. Due to the implementation of the automatic coolant valve the noise could be reduced. A larger thermal mass at the base plate could be used to achieve a further reduction at the cost of a slower controllability of the base temperature.

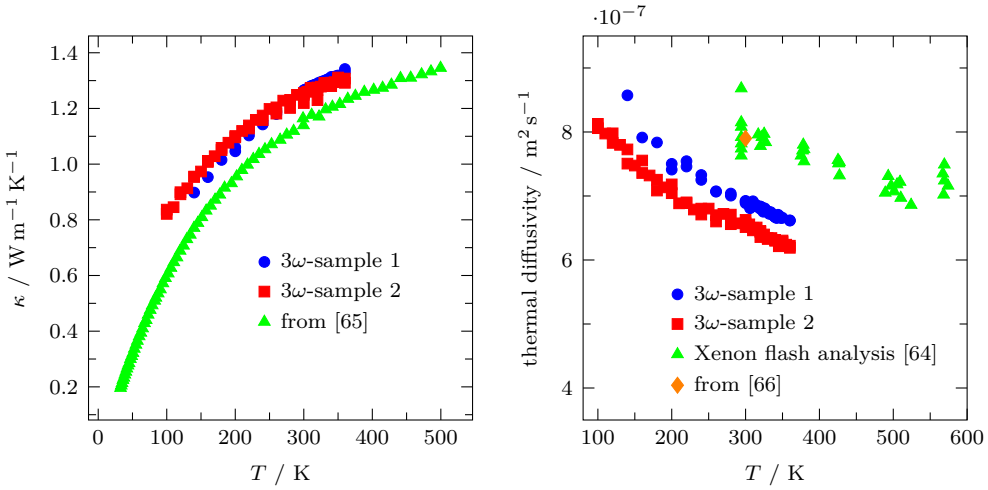

(a) thermal conductivity

(b) thermal diffusivity

Figure 4.2: Thermal properties of the borosilicate glass 3.3 which was used in the two heat flux sensors, measured using 3ω-method and Xenon flash analysis. The thermal conductivity values are needed in the evaluation of the comparative measurements of the ZT-meter.

4.2 Heat flux sensors

For the determination of κ with the comparative method the thermal conductivity of the heat flux sensors has to be known. This knowledge can either be obtained by employing the guarded heater mode of the ZT-meter to measure κ of the heat flux sensors directly, or by using another method to determine κ of the glass material used for the sensors. To allow for a comparison between the guarded heater mode and the comparative method, the latter approach has been chosen and κ of the glass has been determined by the 3ω-method.

The thermal conductivity of the glass was determined using a self-built 3ω-set-up. For the evaluation the method presented in section 2.3.2 was employed. Further investigations of the thermal diffusivity of the heat flux sensor material have been conducted with the Xenon flash analysis method [64]. The results for κ and D are shown in figure 4.2.

A comparison with values for borosilicate glasses from the literature [65, 66] shows that κ is likely to be overestimated while the values for thermal diffusivity are somewhat smaller. However, there are different types of Pyrex glasses and the sources are unclear about which kind was used exactly for the measurement.

The thermocouples for the heat flux measurement where inserted into holes with a distance of about 4 mm and a diameter of 0.8 mm, which were drilled by a CNC drilling machine. Their positions are assumed to be exact. As the thermocouples

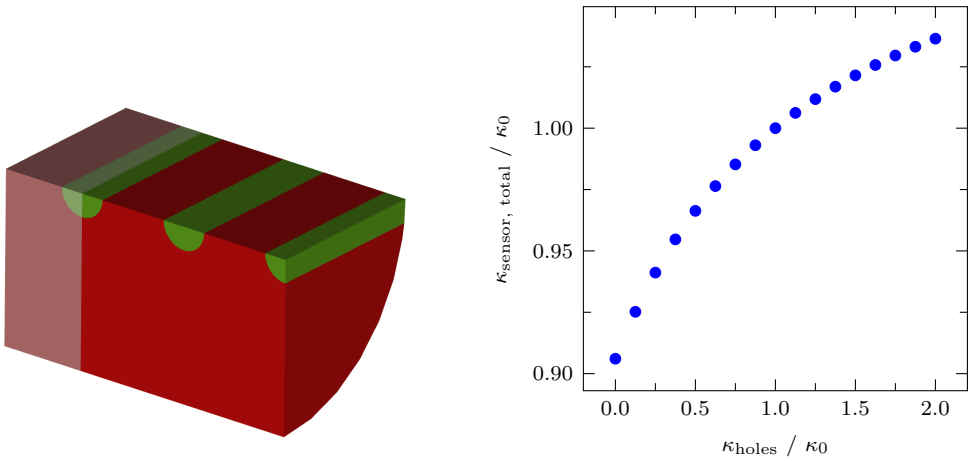

(a) (b)

Figure 4.3: (a) Geometry used for the simulation of the thermal conductivity of the heat flux sensors with filled holes. The glass material is shown in red, the holes for the thermocouples are depicted in green. (b) The thermal conductivity of the heat flux sensors $\kappa_{\text{sensor, total}}$ for different thermal conductivities of the fill material κ_{holes}.

had a diameter of about 0.5 mm at the junction, the position uncertainty of the junctions is about 0.3 mm. After the assembly, the positions of the junctions were determined using a Vernier calliper with an uncertainty of about 0.1 mm.

The holes inside the glass cylinders lead to a change of the total thermal resistance of the heat flux-sensors. Unfortunately the thermal conductivity of the mix between heat transfer paste and thermocouple cannot be determined accurately. A 3-dimensional FEM simulation has been conducted to estimate the impact of the holes on the thermal conductivity measured by the three thermocouples inside each heat flux sensor. Figure 4.3 depicts the geometry used in the model and the corresponding values of $\kappa_{\text{sensor, total}}$ for various values of κ_{holes}, the thermal conductivity of the fill material. For κ_{holes} being zero, κ of the sensors is at about 90 % of its original value, while for an infinite large κ_{holes}, it is at 112 %. With the exact value for κ_{holes} being unknown, an exact correction factor cannot be determined. Thus, for the evaluation of the measurement data it has been assumed that the fill material has the same κ as its surroundings.

4.3 Seebeck coefficients of the measurement wires

For the measurement of the absolute Seebeck coefficient using the method presented in section 3.3 the Seebeck coefficients of each of the two materials of a thermocouple needs to be known. In the current set-up a type K thermocouple consisting of chromel and alumel was used. Unfortunately the precise material composition

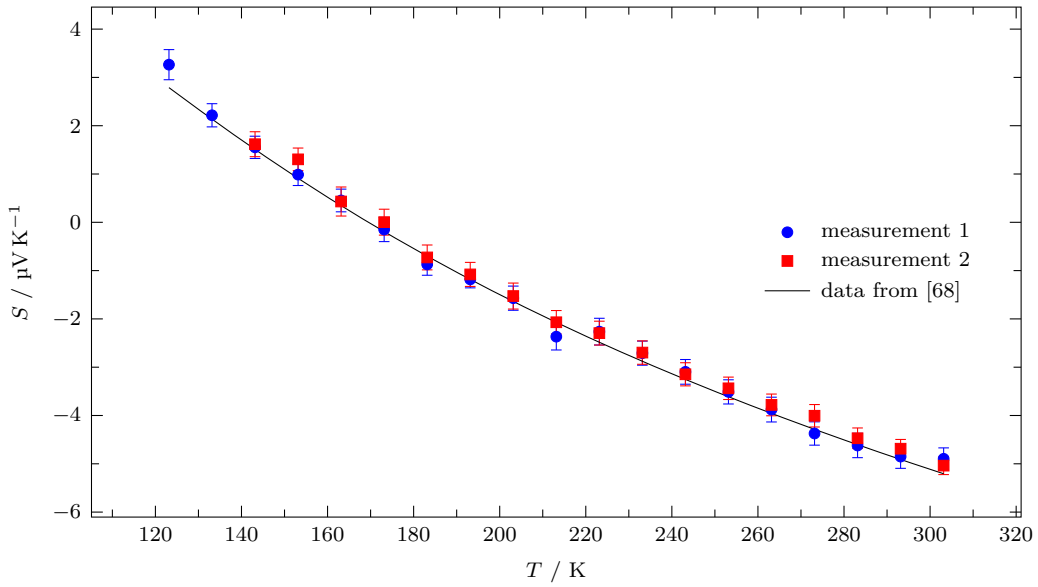

Figure 4.4: Measurements on pure platinum using an existing Seebeck measurement system fit well to values from the literature.

of thermocouples is not standardized and depends on the manufacturer. Only the resulting thermovoltages of the whole pair can be obtained using tables e.g. from Ref. 63. To obtain the thermopower of alumel and chromel independently of each other an existing measurement system for low temperature measurements of the Seebeck coefficient was used [67]. Its accuracy has been confirmed using measurements on a pure platinum sample. The obtained values are in good agreement with values of the absolute Seebeck coefficients found in the literature [68] and are plotted in figure 4.4. They show the reliability of the set-up used.

In a next step the Seebeck coefficient S of the two wire types was determined. For both measurement series material from the same coil as used in the ZT-meter set-up was taken, in order to minimize the impact of property changes due to production fluctuations. The wires were suspended on a glass substrate during the measurement to obtain stable temperature gradients. The results are shown in figure 4.5 and were fitted to a polynomial of second order.

As a test the thermovoltage of a thermocouple made of alumel and chromel was calculated by the thermovoltages from 0 °C to the respective temperature and subtracting both integrals. Figure 4.6 shows that these values agree very well with the voltages of a standard type K couple.

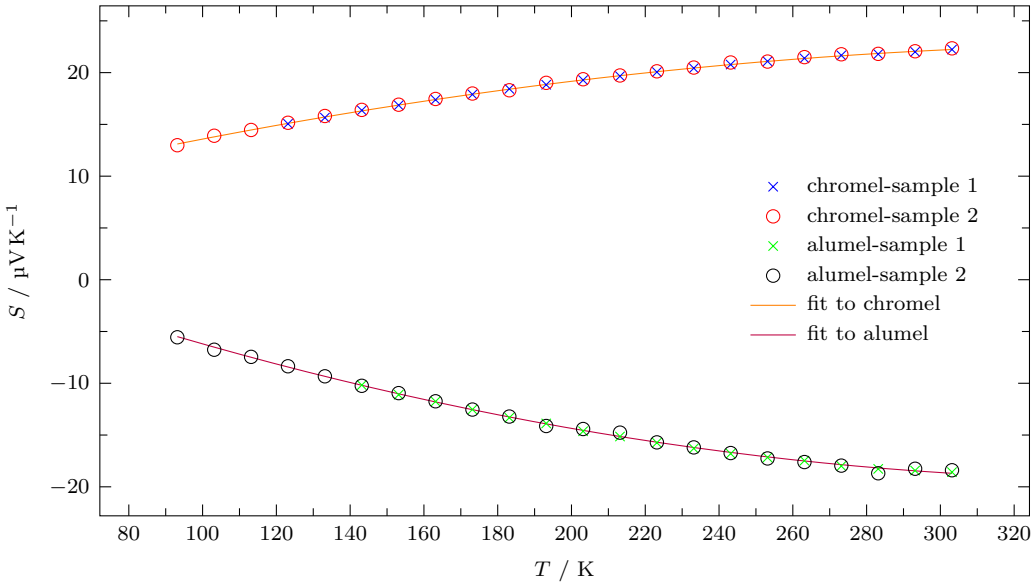

Figure 4.5: Measurements of the absolute Seebeck coefficients for the materials of a type K thermocouple chromel and alumel. The two respective measurements using different applied temperature gradients and samples agree very well and are fitted to a polynomial of second order.

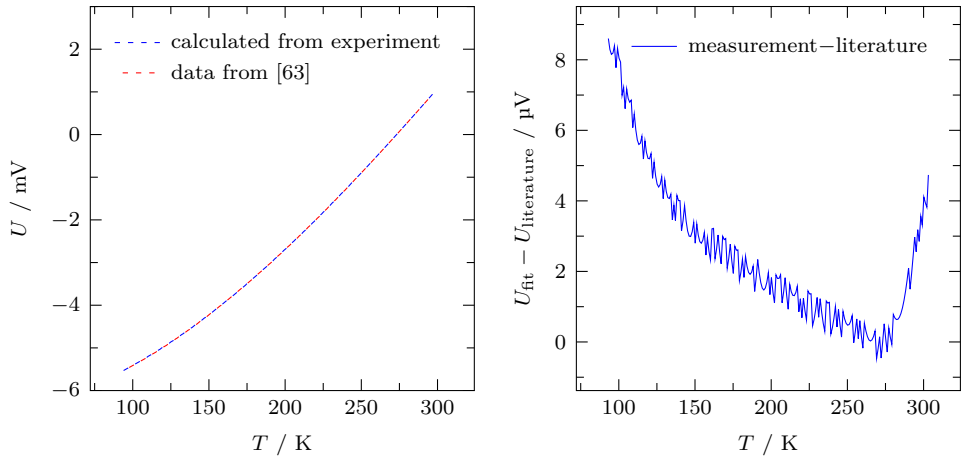

(a) (b)

Figure 4.6: The thermovoltages calculated from the measurements of the Seebeck coefficient of each material are in good agreement with the expected values of a type K thermocouple.

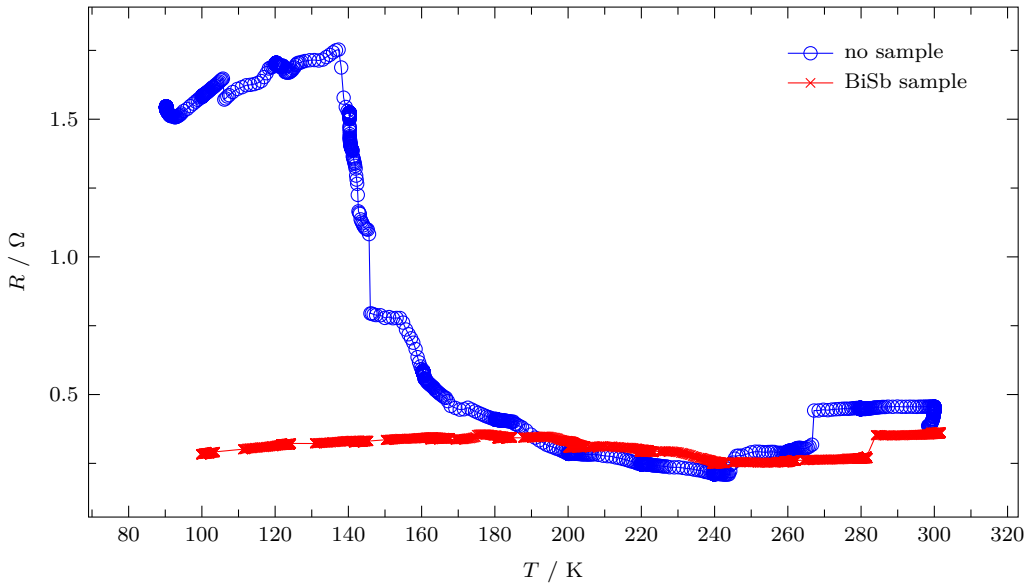

Figure 4.7: The measurement of the electric resistance between the two thermocouples in direct contact and the measurement with a sample in between both of them show that for well conducting samples the interface resistance is larger than the resistance of the sample. Furthermore, the interface resistance cannot be subtracted from the measurement results, as it changes when the samples are exchanged.

4.4 Measurements of the electric conductivity

First tests of the electric conductivity mode of the ZT-meter showed that the interface resistance, which cannot be neglected in the current quasi 4-contact measurement method, is larger than expected and temperature dependent. Furthermore, it cannot be reproduced in different measurements, since the exact impact of the Galinstan solder is different each time the Galinstan is reapplied. Thus, a simple correction by using the interface resistance as an offset is not a valid option. Figure 4.7 shows two measurements, one with no sample in between the two contacts and the other one with a well conducting BiSb sample. The resistance values without the sample are mostly larger than those with the sample, illustrating the issue that the interface resistance cannot be reproduced, since it should be the other way around. As a result, only samples with low electric conductivities can be measured, since here the interface resistance plays a minor role. For well conducting samples the electric conductance measurement of the ZT-meter has to be fundamentally redesigned to achieve a true 4-contact measurement.

4.5 First κ measurements on glass samples

The first thermal conduction measurements were performed on glass samples, cut from the same glass as that used for the sensors. This allows one to estimate the thermal interface resistances, since κ of the heat flux sensors can be directly compared with the measured κ of the sample and the interfaces. Additionally, measurements without a sample have been carried out.

Figure 4.8 shows the results for the comparative approach (a) and the guarded heater method (b). For the comparative method the κ-values were determined with both heat flux sensors and are plotted separately. Those two values, $\kappa_{\mathrm{sample},1}$ and $\kappa_{\mathrm{sample},2}$ are mostly in good agreement. This shows that the heat flux sensors detect the same flux before and after the sample. Heat radiation from the sample as well as parasitic currents from the two thermocouples T_3 and T_4 would lead to a difference in the flux and thus are supposed to be small. The plot for the comparative mode also depicts the assumed value for the thermal conductivities $\kappa_{\mathrm{sensor},1}$ and $\kappa_{\mathrm{sensor},2}$ of the respective heat flux sensors. $\kappa_{\mathrm{sample},1}$ and $\kappa_{\mathrm{sample},2}$ show large deviations from $\kappa_{\mathrm{sensor},1}$ and $\kappa_{\mathrm{sensor},2}$ at low temperatures. This is mainly attributed to a thermal interface resistance, but can also be a result of an uncertainty in the temperature measurements. It was observed that the Galinstan, used for a better thermal contact at the interfaces, is squeezed out of the gaps, possibly due to thermal expansion effects. At larger temperatures the Galinstan melts and the interface resistance is supposed to be smaller as possible gaps get closed. Here $\kappa_{\mathrm{sample},1}$ and $\kappa_{\mathrm{sample},2}$ even become larger than $\kappa_{\mathrm{sensor},1}$ and $\kappa_{\mathrm{sensor},2}$. This can be explained with the previously mentioned change of the thermal resistance of the heat flux sensors due to the drilled holes inside the heat flux sensors, which is probably towards larger resistances than that of a pure glass cylinder. The κ-values for the sample with 9.5 mm length are higher than those of the 7.3 mm sample. As the thermal interface resistance is included into the conductivity value of the sample, shorter samples will show lower conductivities if the interface resistance is equal for both samples. Nevertheless, an estimation of the interface resistance was not possible as either the assumption of a constant value does not hold or the measurement errors are too large.

In figure 4.8b the results for the guarded heater mode are depicted. Similarly to the results of the comparative measurements, again the 9.3 mm sample shows a larger thermal conductivity. In the guarded heater mode, the magnitude of the values is larger compared with those obtained with the comparative mode, especially at higher temperatures. One possible explanation is that the radiation losses at the heater become larger, despite the use of the guard heater. Also, the assumed κ-values for the glass of the heat flux sensors, which were derived with the 3ω-method might be too low.

Not only the thermal conductivity of the sample is determined during a guarded heater measurement but also that of the two heat flux sensors. Figure 4.9 shows the results for the measurements with the two glass samples and the measurement

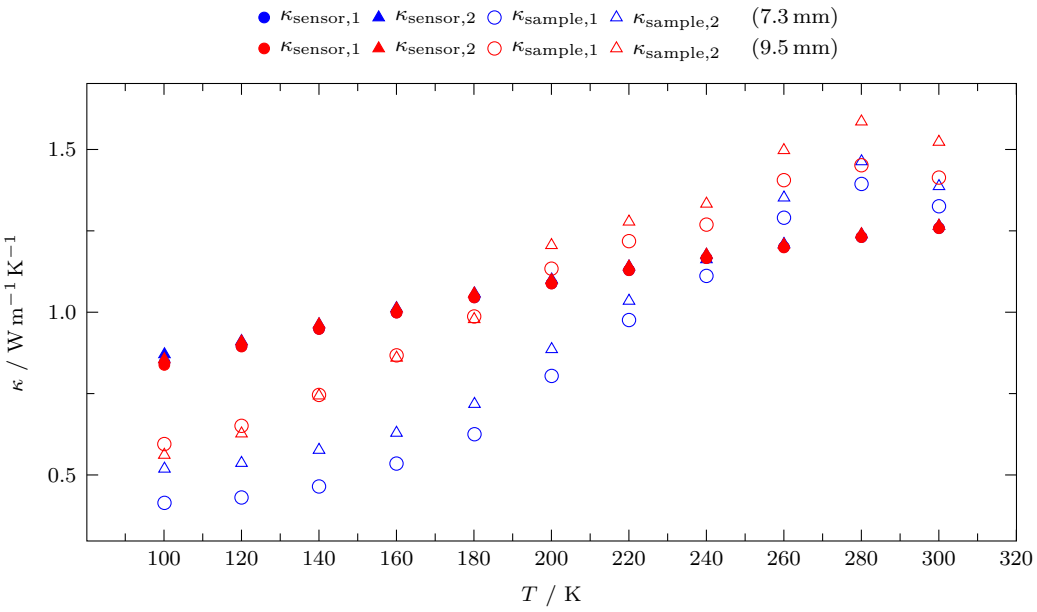

(a)

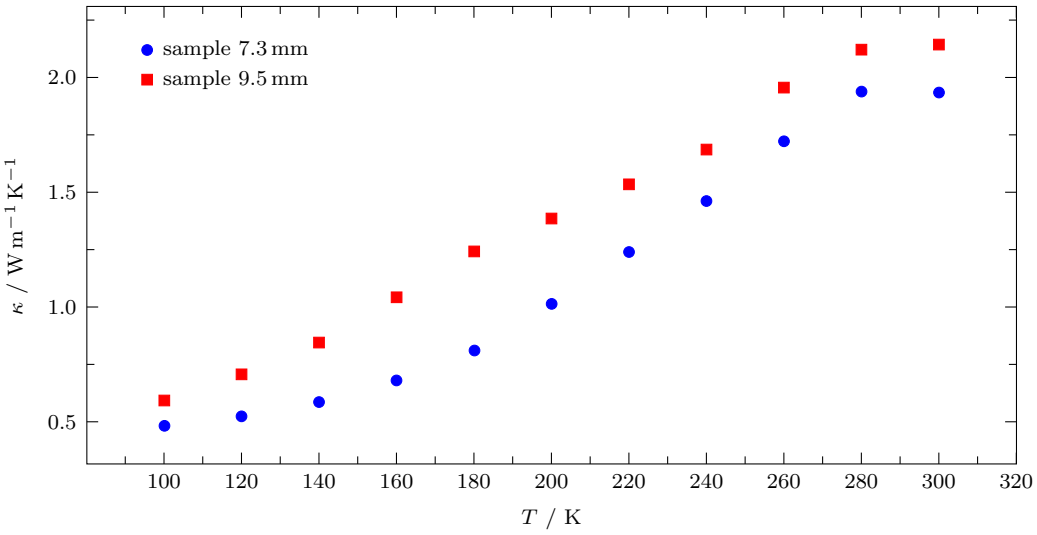

(b)

Figure 4.8: Thermal conductivities of two glass samples with 7.3 mm and 9.5 mm length in the comparative mode (a) and the guarded heater mode (b). For the comparative mode two values ($\kappa_{\text{sample},1}$ and $\kappa_{\text{sample},2}$) are shown for each sample, each calculated from the heat flux determined with one of the two heat flux sensors. The plot also depicts the assumed thermal conductivities for the heat flux sensor $\kappa_{\text{sensor},1}$ and $\kappa_{\text{sensor},2}$. The results obtained by the guarded heater method are higher, especially at higher temperatures, possibly due to radiation errors, or due to the application of too low thermal conductivities for the heat flux sensors in the evaluation.

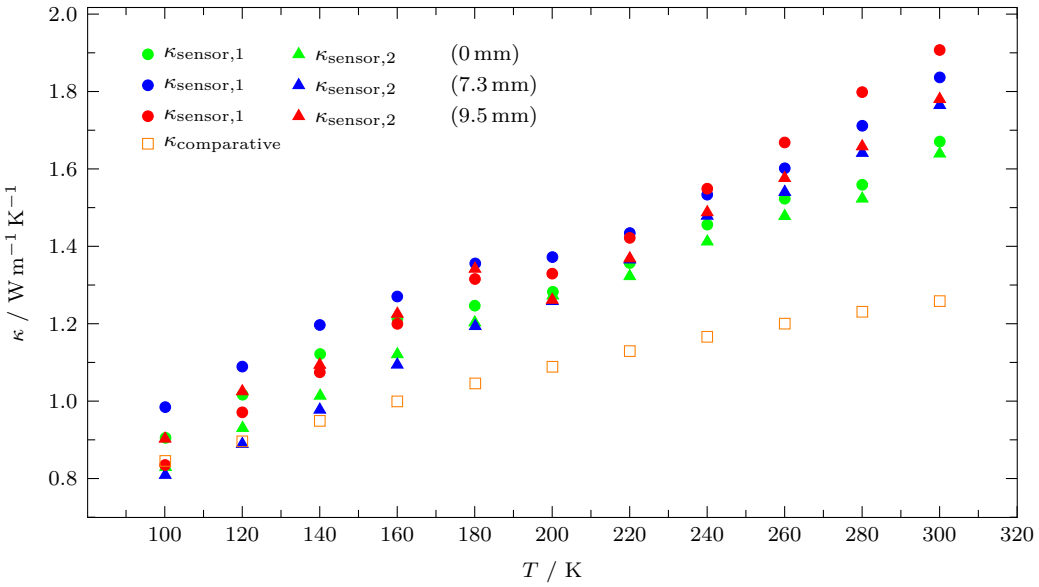

Figure 4.9: Thermal conductivity of the two heat flux sensors obtained with guarded heater measurements of glass samples with 7.3 mm and 9.5 mm lengths. Additionally, a measurement without a sample is shown. The orange squares show the thermal conductivities used in the evaluation of the comparative mode, being smaller over the whole temperature range.

without any sample. Additionally, the calibration curve of the glass material is shown. The six curves corresponding to the three measurements are in good agreement with each other. The calibration curve differs from the measurement results at higher temperatures, which has also been observed in the results shown previously.

In another guarded heater measurement a test without a sample has been conducted. At a constant base temperature of 280 K the heater power has been varied from zero to 70 mW. Figure 4.10a shows that the measured thermal conductivity of the heat flux sensors remains constant for heater powers larger than zero. The temperature difference at the interface between the two temperature sensors T_3 and T_4, which if neither a sample nor a thermal interface resistance is present should equal zero is shown in figure 4.10b. At low heater powers the difference is positive, meaning that the heated side is warmer than the cooled side. At higher temperatures the difference becomes negative. However, these deviations from zero are well within the error limits for temperature difference measurements of ±0.3 K, derived from the previously stated error limits of ±0.15 K for single temperature measurements.

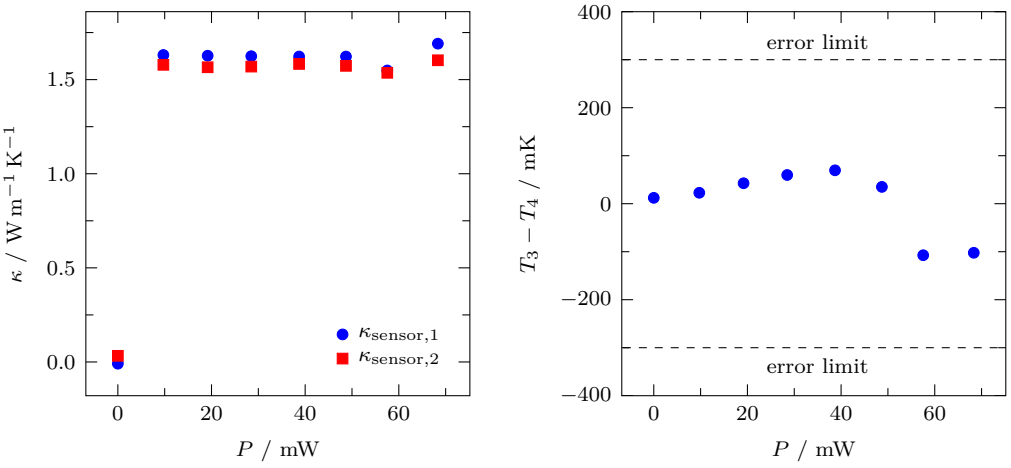

Figure 4.10: The thermal conductivity of the heat flux sensors at 280 K for various heater powers is nearly constant (a). The temperature difference between T_3 and T_4 is shown in (b) and is zero within the error limits for the measurement of a temperature difference of ± 0.3 K which is twice the margin of error of a single temperature measurement.

4.5.1 Transient measurements

Figure 4.11 shows the temperatures of the thermocouples during transient measurements of the 7.3 mm glass sample. The respective simulated results are shown in red. For the simulation, it was assumed that the heat flux sensors have the same material properties as the sample and that thermal interfaces between the glass cylinders exist. As a sinusoidal heat excitation was used, the temperatures of the outermost thermocouples, which are used as input parameters for the simulation, were fitted to a sine function. The simulated temperatures exhibit offsets from the measured ones, but the fit routine still manages to obtain the correct phasing and oscillation amplitudes. The direct comparison between the measurement at 100 K and the measurement at 300 K shows that the temperature difference along the sample is smaller in relation to the total temperature difference. This implies that the interface resistances are getting smaller. Furthermore, the damping of the thermal wave, related to the thermal diffusivity is visible.

The values for $c\rho$ and the thermal diffusivity D were extracted from the simulation and plotted in figure 4.12. The results for D are slightly lower than those obtained from the 3ω-method, probably due to the existence of thermal interface resistances. However, the decreasing behaviour of D towards higher temperatures coincides with that of the 3ω-results.

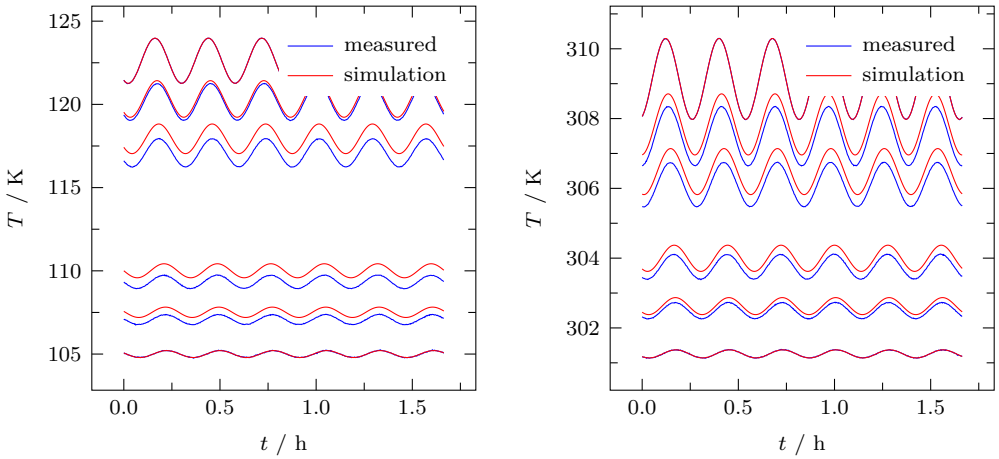

Figure 4.11: Measured (blue) and simulated (red) temperatures of the thermocouples during a transient measurement of a glass sample with a periodic excitation at 100 K (a) and 300 K (b).

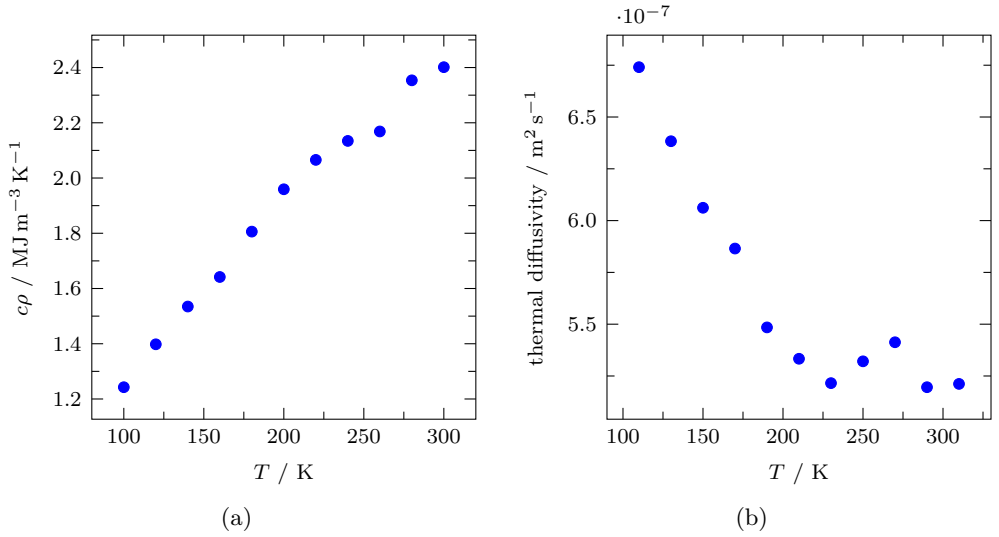

Figure 4.12: $c\rho$ (a) and the corresponding thermal diffusivity (b) obtained during a transient measurement of a glass sample.

4.6 Measurements on a BiSb sample

As a further test, the thermal properties of a BiSb sample with an antimony content of 20 % have been investigated. Results of all measurement modes for the thermal conductivity are shown in figure 4.13a. At larger temperatures, again the κ values obtained with the guarded heater method are larger than those obtained with the other methods. The difference between the results obtained with the two heat flux sensors in the comparative mode is larger compared to previous measurements.

The measured volumetric heat capacity $c\rho$ of the BiSb sample is depicted in figure 4.13b. It is nearly constant over a wide temperature range and shows an outlier at 280 K. The values increase slightly towards higher temperatures. Figure 4.13c depicts the thermal diffusivity, obtained with the transient mode and laser flash analysis measurements on a similar sample at higher temperatures. The results at room temperature, where the temperature ranges of both measurements overlap, match well with each other.

During the transient measurement of the BiSB sample also measurements of the Seebeck coefficient were conducted. As described previously, this was done during the increases of the base temperature. The results were evaluated using the voltages from the two wire branches separately. Also, the alternative approach, using the wires of both material types simultaneously has been realized. The values, plotted in figure 4.13d, show only small deviations from each other for the three evaluation types. Another BiSb sample with the same material composition but prepared in a different production run has been investigated using a different measurement set-up for the Seebeck coefficient. Its results are in good agreement with those obtained with the ZT-meter, the deviations are inside the production tolerance of the sample.

4.7 Measurements on a POM sample

Measurements on a polyoxymethylene (POM) sample have been conducted to test the set-up with a sample having a low thermal conductivity. In the case of such a sample, the temperature gradient along the sample is larger compared with those along the heat flux sensors and the determination of the heat flux has a larger uncertainty. Additionally, parasitic heat currents are more likely due to the larger thermal resistance of the sample. Thus, the guarded heater mode, which is especially sensitive to such parasitic currents, can show large deviations, especially at higher temperatures. Furthermore, since only small heater powers are used to define the required temperature gradient, the impact of small offsets in the power determination is higher. The measurement results of the POM sample are depicted in 4.14.

The values for κ from the two sensors in the comparative mode and the fit-results for κ from the transient approach are in good agreement with each other. However,

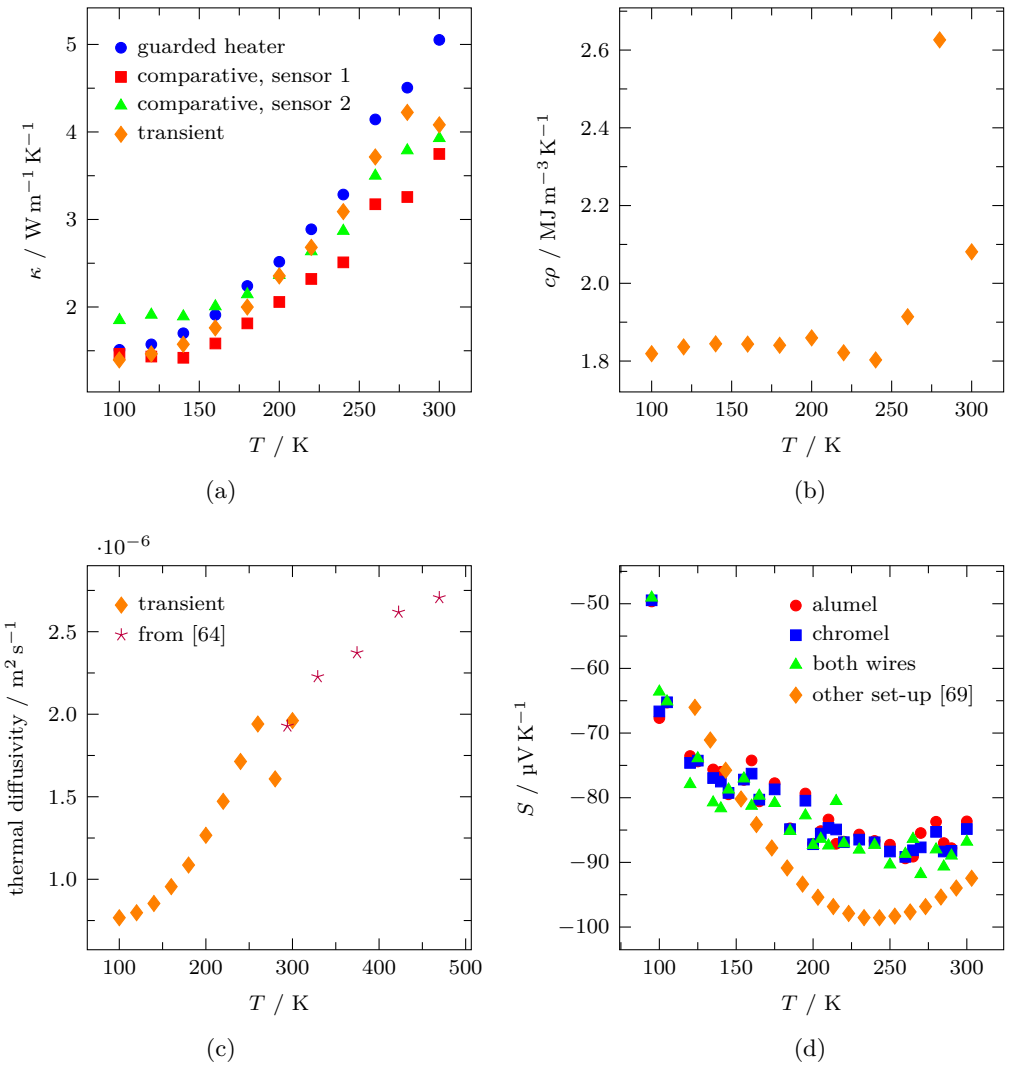

Figure 4.13: (a) Thermal conductivity measured on a BiSb sample with the guarded heater mode, the comparative mode and the transient mode. (b) Volumetric heat capacity of the BiSb sample, obtained by measurements in the transient mode of the ZT-meter. (c) Thermal diffusivity obtained with the transient measurement mode and by laser flash analysis measurements on a similar sample. (d) The Seebeck coefficient of the BiSb sample evaluated using the alumel wires, the chromel wires and both wires at the same time, employing the methods presented in section 3.3.

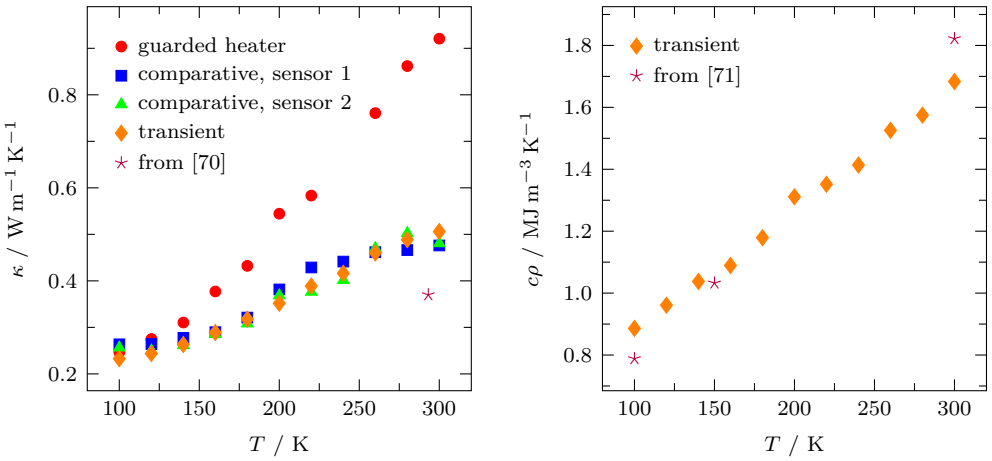

(a) (b)

Figure 4.14: The measurements of the thermal properties of the POM sample show that the results for κ of guarded heater measurement mode deviates strongly from the results of the other modes, probably due to radiative heat losses. On the right side the thermal heat capacity is shown which increases linearly with the temperature.

the values from the guarded heater mode deviate strongly for higher temperatures, probably due to parasitic currents. The literature value at room temperature is slightly beneath the values obtained with the comparative method, which is due to the overestimation of the thermal conductivity of the heat flux sensors. However, the values for $c\rho$, obtained with the transient approach, are in good agreement with the literature values for all temperatures. This is unexpected, since the $c\rho$ value indirectly also depends on the calibration of the heat flux sensors.

In addition, an example for the temperature distribution in the set-up during the steady-state measurement of the POM sample at 300 K is shown in figure 4.15. The three thermocouples in each of the two heat flux sensors show a temperature being proportional to its position. Both heat flux sensors measure nearly the same heat flux, since their $\partial T/\partial x$ values match.

4.8 Sources of measurement error

In the following the sources of measurement error of the ZT-meter are discussed and possible countermeasures are suggested and explained. The most obvious source error is to be found in the voltage measurements with the data-logger system, which can have voltage offsets or scaling errors, originating from the instrument itself or from unwanted thermovoltages. Offsets originating from the instrument itself are handled by carrying out a reference measurement at the beginning and the end of each measurement on a separate input channel which has been short-circuited. The

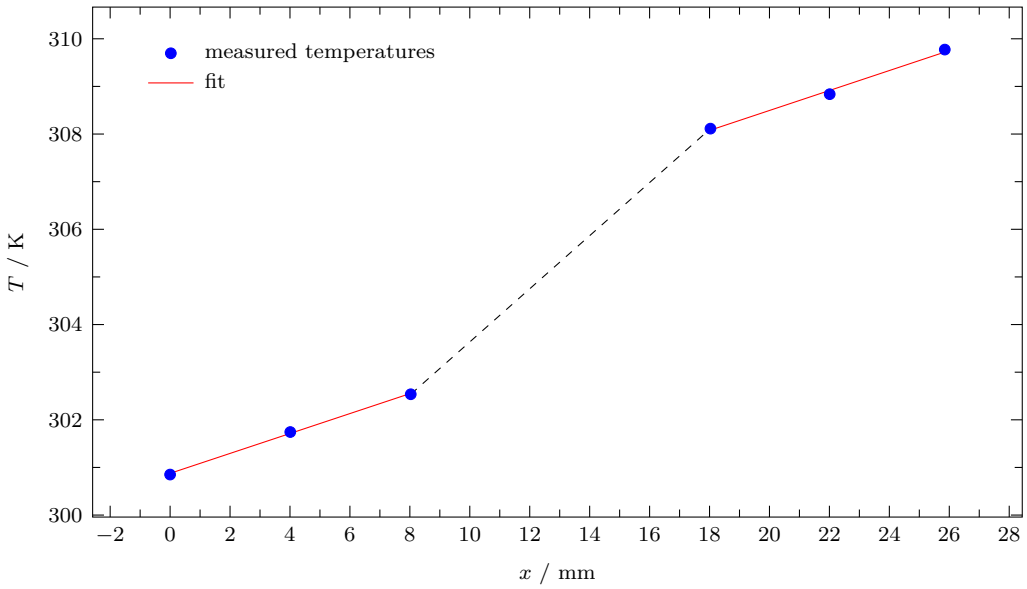

Figure 4.15: Measured temperatures as function of position during a steady state measurement of a POM sample at 300 K.

resulting offset voltage is then subtracted from each voltage measurement. Additional thermovoltages might have their origin in the coils of the relays, used for the input signal switching, causing non-symmetrical heating. In the self-designed circuits this problem was avoided by paying attention to a strictly symmetrical design and a symmetrical driving of the relays. Another possible source of thermovoltages are material variations in the measurement wires, leading to different Seebeck coefficients inside a wire pair, and, thus, decrease the accuracy of the temperature measurements.

The bouncing of the relays can lead to uncertainties in the voltage measurement, so an appropriate waiting time between the measurements of two signal channels has to be established. Also, if an auto-ranging function of the instrument is used, the waiting time has to be long enough to ensure that the auto-ranging is complete. This, however, can be abbreviated by presorting the channels by their expected signal sizes and thus avoid measuring a small Seebeck voltage directly after the considerably higher driving voltage of a heater.

Imprecise voltage or resistance measurements of the instrument influence the measurement in several ways. First of all, the sample and the heat flux sensor temperatures are evaluated by voltage measurements and by the determination of the resistance of a Pt100 resistor inside the reference block. A constant and equal voltage offset on all channels creates a temperature offset nearly equal for all sensors and should hardly influence the results of the thermal conductivity measurements in the comparative or transient mode. Also, the Seebeck coefficient measurements are designed to handle such an offset by performing several measurements at different temperature gradients along the sample. The voltage offset can then be eliminated by using

Eq. (3.8) or Eq. (3.9). However, if varying offsets occur, this would not be accounted for. A constant offset in the voltage measurement also greatly reduces the accuracy of the guarded heater method for determining κ, as the power of the heater cannot be determined correctly. Also, the shunt resistor for the heater current measurement has to be known very precisely and should not exhibit a temperature dependence for the same reasons.

Another issue leading to errors in the determination of the temperatures and Seebeck coefficients are inhomogeneities or contaminations of the thermowires. The two innermost thermocouples are connected to the sample by using Galinstan for a better thermal and electric contact. Unfortunately Galinstan is known to be aggressive towards some metals and could corrode the wires materials, though, this effect was not observed during the investigations. Replacing the thermocouples by a resistive measurement method might be an option. However, the thermal masses of the resistors would probably be larger than the thermal masses of the thermocouples, leading to unwanted phase shifts.

In the case of the steady-state measurement method for the thermal conductivities other sources of systematic errors are also of relevance. Here especially unwanted heat flows, like heat conduction along the heater wires or the thermocouples should be kept small, which can be achieved by using longer, thinner wirings and also keeping them in good thermal contact with the guard. Another problem is heat radiation, especially at higher temperatures. It leads to heat fluxes from the heaters to the shield or to the sample, or from the sample to the shield. For the steady-state mode this cannot be accounted for in the evaluation. In particular the radiation from the heater, being the hottest point in the measurement system, poses a problem. An estimation of this error turns out to be rather complex as the amount of radiation depends on many unknown parameters. Thus, only the error due to heat radiation of the sample and the sensors to the ambient, which also play a role in the other measurement modes, will be treated in the following elaboration. In order to estimate the error due to heat radiation it is best to compare the heat conductance of the sample and the sensors G to the radiative conductance $G_{\text{radiative}}$. The heat conductance G is defined as:

$$G = \frac{P}{\Delta T} = \frac{\pi r^2 \kappa}{l}, \tag{4.2}$$

where P denotes the power to the heated side of the sample, r is the sample radius and l the sample length. For two nested cylinders the radiative conductance under the assumption of a constant ambient temperature and by neglecting the view-factors (which are 1 for specular surface radiation) is given by:

$$G_{\text{radiative}} = \Sigma \epsilon 2\pi r \int_0^l T\,(z)^4 - T_{\text{ambient}}^4 dz, \tag{4.3}$$

where Σ is the Stefan-Bolzmann constant and ϵ the material's emissivity. By assuming a linear $T(z)$ dependence and that $\Delta T << T$ one obtains:

$$\frac{G_{\text{radiative}}}{G} \approx \frac{4\epsilon\Sigma l^2 T_{\text{ambient}}^3}{r\kappa}. \tag{4.4}$$

This result shows that the length of the sample and the sensors must not become too large, otherwise the heat transport by radiation becomes dominant. However, the formula shows the worst case scenario, as it neglects the gradient of the inner heat shield. If the temperature gradient from the sample and the sensors is mirrored by the shield perfectly, no net radiation flux can occur except from the lower and upper end of the measurement system.

The contact between the heat flux sensors and the sample is important, not only for the measurements of κ, but also for the determination of the electric conductivity σ. Galinstan with its good wetting properties and good thermal and electric properties is used to reduce the thermal and electric contact resistances at the interfaces. Unfortunately, in addition to possible corrosion effects of the sample and the thermocouples, Galinstan undergoes a solid-liquid phase transition during the temperature cycles, thereby the interface properties are altered. Also, due to the thermal expansion of the measurement bar, the Galinstan may flow out of the gap and thus has to be renewed after one temperature cycle. As the measurement of the electric conductance is carried out with the wires of the two thermocouples, a 4-contact measurement mode, where the contact resistances are cancelled out, is not possible. Since voltage and current contacts either side of the sample are in the same place, the contacts between the junction and the sample influence the results. For samples with a high electric conductivity the interface resistance may be larger than the sample resistance which makes a measurement unreasonable and other methods need to be employed. The situation is somewhat similar in case of the thermal conductivity measurements of good heat conductors. However, as most good thermoelectric materials are poor conductors of heat, this problem is considered to be small. The imperfect contacts between the sample and the thermocouples also influence the error for the Seebeck coefficients, as the temperature gradients cannot be measured exactly. In addition, Galinstan may add a small thermovoltage since it is also subject to a small temperature difference. As the difference should be very small compared with the difference of the sample, this effect should be negligible.

Interfaces also play a role in the temperature measurements inside the heat flux sensors. First of all, the drilles holes inside the glass cylinders change the thermal mass and resistance of the sensors, and thus should be kept very small. The impact of this effect has been calculated above and is in the range of $\pm 12\,\%$ deviation for the thermal conductivity of the heat flux sensor, depending on the filling material.

Furthermore, the contact between glass and thermocouple introduces errors. As the junctions of the thermocouples are surrounded by the glass, they should be approximately at the same temperature as the glass, thus, this temperature offset is negligible. However, the contact resistance and the thermal mass of the filling material introduce a temporal lag, which influences the phase information in transient measurements. The problem itself cannot be avoided completely, but by making the

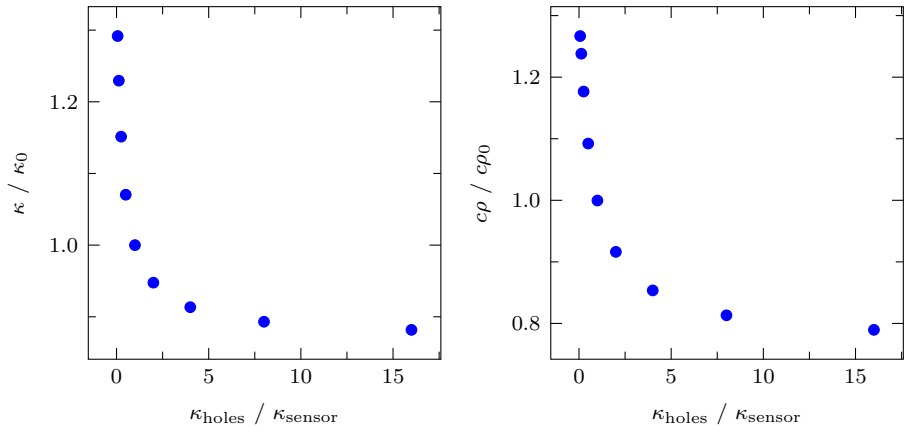

Figure 4.16: Results for κ and $c\rho$ from a fit to a three-dimensional FEM simulation which takes the thermal conductivity of filling material of the drilled holes inside the glass cylinders into account. The increase in both values can be explained with the lower values of κ_{holes}. The effect of the temporal lag of the temperatures has only a small impact in this configuration due to the high symmetry of the delay.

bondings of the thermocouples as identical as possible, the phase shift should be equal for all temperature sensors and will cancel out in the transient evaluation.

A three-dimensional FEM simulation was employed to further evaluate the problem of the temporal lag in transient measurements. The geometry used for the heat flux sensors was similar to the one shown in figure 4.3. Figure 4.16 depicts the corresponding fit-results after fitting the FEM data to the one-dimensional model. For a low conducting filling material, κ gets overestimated. Furthermore, as the heat flux sensors measure a heat flux which is higher than the correct value, the value for $c\rho$ is too high. If the filling material has a higher thermal conductivity, the κ of the sample, as well as $c\rho$ is underestimated.

As the relative deviations for both quantities are almost the same, the predicted effect of the temporal lag is rather small. The values of $(c\rho/c\rho_0)/(\kappa/\kappa_0)$ are in the range of $1 \pm 4\,\%$ for the investigated case. The small impact is probably a result of the nearly symmetric arrangement of the holes in the glass cylinders. Furthermore, the values indicate that if the sensor material and the filling material have a mismatch of their κ values by a factor smaller than two, the measurement values deviate by less than $10\,\%$ for a symmetric arrangement. Of course this number changes for different material parameters than those chosen for the simulation but are a good starting point for an error estimation.

source of error	Δ of input parameter	$\Delta\kappa_{\text{comparative}}$ $\mathrm{W\,m^{-1}\,K^{-1}}$	$\Delta\kappa_{\text{guarded heater}}$ $\mathrm{W\,m^{-1}\,K^{-1}}$
T-measurement	0.15 K	0.30	0.31
position of TCs	0.1 mm	0.06	0.03
κ_{sensor}	$0.2\,\mathrm{W\,m^{-1}\,K^{-1}}$	0.23	0
heater power ($\pm 5\,\%$)	5.4 mW	0	0.15
measurement results		1.46	2.14

Figure 4.17: Maximum error margins during a steady-state measurement of a glass sample of 9.5 mm length at 300 K with a difference of 10 K between the minimum and the maximum temperature along the measurement bar.

4.8.1 Estimation of the error limits for selected error sources

In the comparative mode, the value for κ_{sample} is determined by performing a least-squares fit on the data from one of the heat flux sensors versus the positions and inserting the resulting heat flux as well as the temperature difference κ_{sensor} along the sample into Fourier's law. With the temperatures of the thermocouples inside the sensor being T_1, T_2 and T_3 and x_1, x_2 and x_3 being the respective positions, κ_{sample} is given by:

$$\kappa_{\text{sample}} = -\frac{\kappa_{\text{sensor}} l_{\text{sample}}}{2\Delta T_{\text{sample}}} \cdot \frac{T_1\,(x_2 + x_3 - 2x_1)\,T_2\,(x_1 + x_3 - 2x_2)\,T_3\,(x_1 + x_2 - 2x_3)}{x_1^2 + x_2^2 + x_3^2 - x_1x_2 - x_2x_3 - x_1x_3}. \tag{4.5}$$

In the guarded heater mode, κ_{sample} is determined directly by Fourier's law:

$$\kappa_{\text{sample}} = \frac{P \cdot l_{\text{sample}}}{A \cdot \Delta T_{\text{sample}}}, \tag{4.6}$$

where A is the cross-section of the sample and P is the heater power.

Eqs. (4.5) and (4.6) can be used to estimate the error limits for the values by means of error propagation. A list of the influence of the estimated errors in the measurement of position, temperature or power on the final results is shown exemplarily for the measurement of the 9.5 mm glass sample in table 4.17. The temperature difference applied to the heat flux sensors was approximately 10 K and the measurement was done at 300 K. The table suggests that the two largest portions of the error budget are the temperature measurement and the calibration of the heat flux sensor.

Of course other sources of error, like parasitic heat currents due to improper guarding and thermal interface resistance also increase the error, but a proper estimation of those effects is hardly possible.

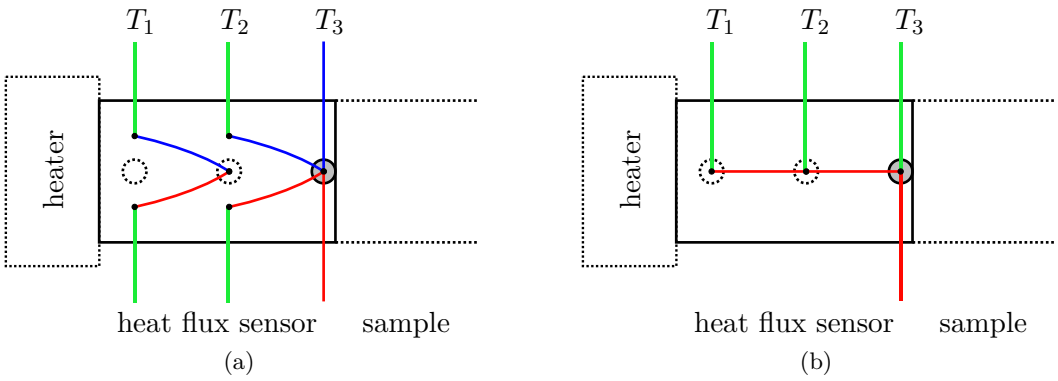

Figure 4.18: The temperature measurement inside the heat flux sensors can be improved by implementing differential measurements using thermocouples. Blue and red wires depict two different materials for a thermocouple and the green wires are made of a material with a low Seebeck coefficient, preferably metallic.

4.8.2 Strategies to enhance the measurement accuracy of the *ZT*-meter

In the previous section the different sources of error were identified and for some of them the impact on the measurement result was quantified. The most important error source is the temperature measurement inside the heat flux sensors. Unfortunately it is very difficult to obtain more precise temperatures with thermocouples in the current configuration of the set-up. A change of the material from type K to type E which has a $\approx 58\,\%$ higher thermovoltage output may reduce the errors. However, this is still not sufficient to obtain reliable measurements of κ. A large uncertainty is introduced into the temperature measurement by the use of long wires to the reference point, where material inhomogeneities can occur. The solution to this problem could be to implement a differential temperature measurement, like it is done for the determination of the temperature difference between heater and guard. Figure 4.18 depicts possible implementations of such a method.

The direct conversion of the principle which was already used for the guard is shown on the left and will be rather complicated to apply due to the possible crossings of the wires. On the right-hand side, a more advanced method is shown, which reduces the number of required wires to four and still enables one to perform an absolute temperature measurement at one boundary. With this method the glass could even be replaced by a thermoelectric material. The functionality of the wires in the direction parallel to the cylinder axis is then established by the heat flux sensor material itself. Thus, also materials with larger thermal conductivities could be employed as heat flux sensors, which would increase the measurement range of the *ZT*-meter. It is also possible to embed the wirings directly at the time of synthesis of the sensor material which would improve the thermal contact to the wirings. Both

methods still require a temperature reference for the measurement of the absolute temperature at T_3 and T_4 in the second heat flux sensor. To avoid the summation of the error due to material inhomogeneities along a long thermowire and over a large temperature difference it is advisable to move the reference into the vacuum chamber itself. The measurement of the temperature gradient along the sample, which poses another important contribution to the error, could greatly benefit from this redesign. In addition, the electric contact to the sample will probably be improved, too, when the heat flux sensor material is electrically conducting. The quasi-4-contact configuration, used for the electric measurements, as well as the measurements of the Seebeck coefficients is still possible without changes to the wiring.

The measurement of the electric conductivity is strongly influenced by the quality of the electric interface between the thermocouples and the sample. Unfortunately, if the interface resistance is larger than the sample resistance, the measurement mode is not applicable to electrically well conducting samples. In addition, the interface resistance changes with temperature probably due to mechanical stress and the phase change of the Galinstan solder. To improve the reliability of the electric conductance measurements the solder might be replaced. Also, multiple contacts at each side can be used to establish a real 4-contact measurement. However, geometry corrections for the cylindrical shapes would be needed and a possible anisotropy of the sample conductivities would render the evaluation process difficult in that case.

5 Conclusions

In this work an apparatus for the determination of the thermoelectric properties κ, S and σ of bulk samples has been designed and built. Hereby the focus was on the determination of the thermal conductivity. In order to achieve this the set-up uses two well known approaches, the guarded heater method and the comparative mode. Based on the latter, a new transient mode has been developed, which reduces measurement time, and allows one to determine the thermal diffusivity of the sample in addition to its thermal conductivity. It relies on a variable heater power during the measurement and on a one-dimensional numerical model of the heat flux sensors and the sample to extract the measurement parameters. The transient mode can be implemented in most existing set-ups relying on heat flux sensors for the determination of the heat flux through the sample. In contrast to other transient methods like the Ångström method, this approach yields κ directly without the need for an additional measurement of the heat capacity of the sample. Also, the requirements to the sample geometry are not as strict as in the Ångström method, since the numerical model can be applied for various types of boundary conditions.

The new transient approach has been investigated using a FEM-model to generate temperature data and fitting this to a numerical model which also has been implemented. Knowledge of the information content of single data-points could be obtained by employing Monte-Carlo simulations. Different parameters for the measurement, such as sampling rate, excitation waveform and frequency, have been tested with respect to their impact on the informative value of the measurements. It was shown that a sinusoidal heating is preferable, as here the most information from each data-point can be retrieved. Also, the impact of the measurement geometry and interfaces between sample and heat flux sensors has been investigated. The effect of heat radiation on the measurement results was discussed and it was demonstrated that it can be partially eliminated in the evaluation process.

A new transient measurement mode was presented, where a steady state needs to be approached only at the beginning of the measurement. After that the base temperature is changed step-wise or continuously and the data is taken in the entire temperature range of interest. Eventually the fit-algorithm tunes interpolation functions instead of constant values as thermal properties to achieve the best fit to the data. The advantage over the commonly used steady-state methods is a greatly reduced measurement time, as the waiting times for the steady state are omitted.

The set-up, which has been built, may be employed not only for measuring κ and D, but also for determining the electric transport properties, i.e. Seebeck coefficient and electric conductivity, of the sample. A relay switching system allows one to use the thermocouples next to the sample as electric leads for resistance and voltage measurements. An additional current source enables one to measure C-V-curves.

For the actual measurements, the sensors inside set-up had to be calibrated. The $U(T)$-functions for the thermocouples were determined and 3ω-measurements were conducted on the material of the heat flux sensors to obtain their thermal conductivity and thermal diffusivity. Additional measurements of the Seebeck coefficient of the thermocouple materials were performed with another set-up.

First tests of the ZT-meter were carried out on a set of samples and showed that the new transient approach is working properly. Moreover, the other modes of the ZT-meter provide good results, except for the determination of the electric conductivity, which has to be redesigned to enable a true 4-contact measurement. However, for the implementation of the two measurement methods for κ, the guarded heater mode and the comparative mode, into the device, compromises had to be found. The heat flux sensor between guarded heater and the sample increases the thermal resistance of this heat path. Thus, the accuracy of the guarded heater mode is reduced, since the portion of parasitic heat currents is larger. On the other hand, the large thermal resistance between the guarded heater and the shield, results in a bad coupling to the coolant. This is intended in case of the guarded heater mode, but reduces the controllability of the temperature in the comparative mode. Other issues which are decreasing the accuracy of the results are the inaccuracy of the thermocouples and the thermal and electric interface resistances between heat flux sensors and the sample. A solution to the first issue could be another temperature measurement method, such as a resistive approach or a method with differential thermocouples. The problem of interface resistances may probably be overcome by replacing the used Galinstan solder by another solder, more suitable for low temperatures.

In the final section the different error sources leading to measurement inaccuracies in the set-up were discussed and quantified. Strategies for the improvement of the set-up concerning the precision and measurement speed were also presented. Apart from improvements of the set-up itself, also the control and the evaluation processes can lead to more accurate and faster results. The Crank-Nicholson scheme can be implemented into the numerical model, allowing larger time steps and thus a faster computation of the simulation. By performing the numerical simulation in the frequency domain, instead of the time domain, the evaluation of measurements with sinusoidal excitation could be sped up enormously, as the elaborate computation of the settlement phase is not needed.

A faster numerical simulation could be used in a model predictive controlling (MPC) approach to enable a better temperature control inside the set-up during the measurements. Also, a direct error estimation using Monte-Carlo simulations during the measurement can be used to limit the measurement time needed for achieving a given precision goal to the minimum.

Bibliography

[1] Seebeck, T. J. Magnetische Polarisation der Metalle durch Temperatur-Differenz. *Abhandlungen der königlichen Akademie der Wissenschaften zu Berlin* (1825), 265–373.

[2] Seebeck, T. J. Ueber die magnetische Polarisation der Metalle und Erze durch Temperaturdifferenz. *Annalen der Physik* 82, 1,2,3 (1826), 1–20, 133–160, 253–286.

[3] Øersted Notiz von neuen electrisch-magnetischen Versuchen des Herrn Seebeck in Berlin. *Annalen der Physik* 73, 4 (1823), 430–432. doi: 10.1002/andp.18230730410.

[4] Fourier, J. B. J., and Øersted Sur quelques nouvelles expériences thermo-électriques faites par M. le baron Fourier et M. Øersted. *Annales de chimie et de physique.* 22 (1823), 375–389.

[5] Ohm, G. S. Bestimmung des Gesetzes, nach welchem Metalle die Contactelektricität leiten, nebst einem Entwurfe zur Theorie des Voltaischen Apparates und des Schweiggerschen Multiplikators. *Journal für Chemie und Physik* 46 (1826), 137–166.

[6] Becquerel, A. C. On a method of measuring high temperatures. *Edinburgh Journal of Science* 5, 9 (1826), 316–318.

[7] Lenz, E. Über einige Versuche im Gebiete der Galvanismus. *Bulletin scientifique publié par l'Académie impériale des sciences de St.-Pétersbourg* 3, 21 (1838), 321–326.

[8] Joule, J. P. On the heat evolved by metallic conductors of electricity, and in the cells of a battery during electrolysis. *Philosophical Magazine Series 3* 19, 124 (1841), 260–277. doi: 10.1080/14786444108650416.

[9] Thomson, W. On a mechanical theory of thermoelectric currents. *Proceedings of the Royal Society of Edinburgh* 3 (1851), 91–98.

[10] Magnus, G. Über thermoelektrische Ströme. *Annalen der Physik und Chemie* 83, 8 (1851), 469–504.

[11] Altenkirch, E. Über den Nutzeffekt der Thermosäule. *Physikalische Zeitschrift* 10 (1909), 560.

[12] Altenkirch, E. Elektrothermische Kälteerzeugung und reversible elektrische Heizung. *Physikalische Zeitschrift* 12 (1911), 920–924.

[13] Goupil, C., Seifert, W., Zabrocki, K., Müller, E., and Snyder, G. J. Thermodynamics of thermoelectric phenomena and applications. *Entropy* 13, 8 (2011), 1481–1517. doi: 10.3390/e13081481.

[14] Ioffe, A. F. *Semiconductor Thermoelements and Thermoelectric Cooling.* Infosearch Ltd. London, 1957.

[15] Ioffe, A. F., Airapetiants, S. V., Ioffe, A. V., Kolomoets, N. V., and Stil'Bans, L. S. On Increasing the Efficiency of Semiconductor Thermocouples. *Soviet Physics Doklady* 1 (1956), 132.

[16] Goldsmid, J. *Thermoelectric Refrigeration.* Temple Press Books LTD, London, 1964.

[17] Hicks, L. D., and Dresselhaus, M. S. Effect of quantum-well structures on the thermoelectric figure of merit. *Phys. Rev. B* 47 (19 May 1993), 12727–12731. doi: 10.1103/PhysRevB.47.12727.

[18] Hicks, L. D., and Dresselhaus, M. S. Thermoelectric figure of merit of a one-dimensional conductor. *Phys. Rev. B* 47 (24 June 1993), 16631–16634. doi: 10.1103/PhysRevB.47.16631.

[19] Sommerlatte, J., Nielsch, K., and Boettner, H. Thermoelektrische Multitalente. *Physik Journal 6* 5 (2007), 35–41.

[20] Newton, I. Scala Graduum Caloris. Calorum Descriptiones & Figna. *Philosophical Transactions* 22 (1701), 824–829.

[21] Richmann, G. W. De argento vivo calorem celerius recipiente et celerius perdente, quam multa fluida leviora, experimenta et cogitationes. *Novi commentarii Academiae Scientiarvm Imperialis Petropolitanae* 3 (1750-1751), 309–339.

[22] Lambert, J. H. *Pyrometrie oder vom Maaße des Feuers und der Wärme.* Haude & Spener, 1779.

[23] Ingenhousz, J. Lettre de M. Ingen-Housz à M. de la Métherie sur les métaux comme conducteurs de la chaleur. *Observations sur la physique, sur l'histoire naturelle et sur les arts* 34 (1789), 68–69.

[24] Poisson, S. D. *Théorie mathématique de la chaleur.* Bachelier, 1835.

[25] Fourier, J. B. J. Mémoire sur la propagation de la chaleur dans les corps solides. *Nouveau Bulletin des sciences par la Société philomatique de Paris* 6 (1808), 112–116.

[26] Fourier, J. B. J. *Théorie analytique de la chaleur.* Chez Firmin Didot, père et fils, 1822.

[27] Péclet, J. C. Sur la détermination des ccoefficients de conductibilité des métaux par la chaleur. *Annales de chimie et de physique* 3, 2 (1841), 107–115.

[28] Forbes, J. D. Experimental Inquiry into the Laws of the Conduction of Heat in Bars, and into the Conducting Power of Wrought Iron. *Earth and Environmental Science Transactions of the Royal Society of Edinburgh* 23 (01 Jan. 1862), 133–146. doi: 10.1017/S0080456800018494.

[29] Forbes, J. D. Account of some Experiments on the Temperature of the Earth at different Depths, and in different Soils, near Edinburgh. *Transactions of the Royal Society of Edinburgh* 16 (1846), 189–236.

[30] Thomson, W. On the Reduction of Observations of Underground Temperature; with Application to Professor Forbes Edinburgh Observations, and the continued Calton Hill Series. *Transactions of the Royal Society of Edinburgh* 22 (1860), 405–427.

[31] Ångström, A. J. New method of determining the thermal conductibility of bodies. *Philosophical Magazine* 25 (1863), 130–142.

[32] Ångström, A. J. Neue Methode, das Wärmeleitungsvermögen der Körper zu bestimmen. *Annalen der Physik* 190, 12 (1861), 513–530.

[33] Lees, C. H. On the Thermal Conductivities of Single and Mixed Solids and Liquids and their Variation with Temperature. *Phil. Trans. R. Soc. Lond. A* 191 (1898), 399–440. doi: 10.1098/rsta.1898.0010.

[34] Cannon, J. R. *The One-Dimensional Heat Equation*. Cambridge University Press, 1984.

[35] Parker, W. J., Jenkins, R. J., Butler, C. P., and Abbott, G. L. Flash Method of Determining Thermal Diffusivity, Heat Capacity, and Thermal Conductivity. *Journal of Applied Physics* 32, 9 (1961), 1679–1684. doi: 10.1063/1.1728417.

[36] Cape, J. A., and Lehman, G. W. Temperature and Finite Pulse-Time Effects in the Flash Method for Measuring Thermal Diffusivity. *Journal of Applied Physics* 34, 7 (1963), 1909–1913. doi: 10.1063/1.1729711.

[37] Cahill, D. G., and Pohl, R. O. Thermal conductivity of amorphous solids above the plateau. *Physical Review B* 35, 8 (Mar. 1987), 4067–4073. doi: 10.1103/PhysRevB.35.4067.

[38] Cahill, D. G. Thermal conductivity measurement from 30 to 750 K: the 3 omega method. *Review of Scientific Instruments* 61, 2 (1990), 802–808. doi: 10.1063/1.1141498.

[39] Cahill, D. G., Katiyar, M., and Abelson, J. R. Thermal conductivity of a-Si:H thin films. *Physical Review B* 50, 9 (Sept. 1994), 6077–6081. doi: 10.1103/PhysRevB.50.6077.

[40] Stranz, A., Waag, A., and Peiner, E. Thermal characterization of vertical silicon nanowires. *Journal of Materials Research* 26, 15 (2011), 1958. doi: 10.1557/jmr.2011.60.

[41] Lefèvre, S., and Volz, S. 3ω-scanning thermal microscope. *Review of Scientific Instruments* 76, 3, 033701 (2005). doi: 10.1063/1.1857151.

[42] Raudzis, C. E. *Anwendung und Erweiterung der 3ω Methode zur Charakterisierung komplexer Mehrschichtsysteme in der Mikrosystemtechnik.* Der Andere Verlag, 2006.

[43] Sidles, P., and Danielson, G. Thermal diffusivity of metals at high temperatures. *Journal of Applied Physics* 25, 1 (1954), 58–66.

[44] King, R. W. A method of measuring heat conductivities. *Physical Review* 6, 6 (1915), 437.

[45] Starr, C. An Improved Method for the Determination of Thermal Diffusivities. *Review of Scientific Instruments* 8, 2 (1937), 61–64. doi: 10.1063/1.1752237.

[46] Abeles, B., Cody, G. D., and Beers, D. S. Apparatus for the Measurement of the Thermal Diffusivity of Solids at High Temperatures. *Journal of Applied Physics* 31, 9 (1960), 1585–1592. doi: 10.1063/1.1735897.

[47] Belling, J. M., and Unsworth, J. Modified Angström's method for measurement of thermal diffusivity of materials with low conductivity. *Review of Scientific Instruments* 58, 6 (1987), 997–1002. doi: 10.1063/1.1139589.

[48] Muscio, A. Measurement of thermal diffusivity by a modification of the Angstroem's method using thermally short specimens. *9th International Conference on Quantitative InfraRed Thermography* (2008).

[49] Boor, J. de, and Müller, E. Data analysis for Seebeck coefficient measurements. *Review of Scientific Instruments* 84, 6, 065102 (2013). doi: 10.1063/1.4807697.

[50] Cengel, Y. A. *Heat Transfer: A Practical Approach, Second Edition.* Mcgraw-Hill, 2002.

[51] Crank, J., and Nicolson, P. A practical method for numerical evaluation of solutions of partial differential equations of the heat-conduction type. *Mathematical Proceedings of the Cambridge Philosophical Society* 43, 01 (1947), 50–67.

[52] Hoffman, J. D., and Frankel, S. *Numerical methods for engineers and scientists.* CRC press, 2001.

[53] Heun, K. Neue Methode zur approximativen Integration der Differentialgleichungen einer unabhängigen Veränderlichen. *Zeitschrift für Mathematik und Physik* 45, 1 (1900), 23–38.

[54] Süli, E., and Mayers, D. F. *An introduction to numerical analysis.* Cambridge University Press, 2003.

[55] Welty, J. R., Wicks, C. E., Rorrer, G., and Wilson, R. *Fundamentals of momentum, heat, and mass transfer.* Danver, MA: Wiley; 5th ed., 2008.

[56] Press, W. H., Teukolsky, S. A., Vetterling, W. T., and Flannery, B. P. *Numerical Recipes in C (2Nd Ed.): The Art of Scientific Computing*. Cambridge University Press, New York, NY, USA, 1992.

[57] Powell, M. J. D. An efficient method for finding the minimum of a function of several variables without calculating derivatives. *Computer Journal* 7, 2 (1964), 155–162.

[58] Brent, R. P. *Algorithms for minimization without derivatives*. Prentice Hall, Englewood Cliffs, 1973.

[59] Gegenfurtner, K. *PRAXIS*. July 1987. url: http://archives.math.utk.edu/software/msdos/numerical.analysis/praxis/.html.

[60] Marsaglia, G., and Tsang, W. W. The Ziggurat Method for Generating Random Variables. *Journal of Statistical Software* 5, 8 (2000), 1–7.

[61] Leong, P., Zhang, G., Lee, D.-U., Luk, W., and Villasenor, J. A comment on the implementation of the ziggurat method. *Journal of Statistical Software* 12, 7 (Feb. 2005), 1–4.

[62] Burkardt, J., Marsaglia, G., and Tsang, W. W. *Ziggurat Random Number Generator (RNG)*. Oct. 2013. url: http://people.sc.fsu.edu/~jburkardt/c_src/ziggurat/ziggurat.html.

[63] *NIST ITS-90 Thermocouple Database*. url: http://srdata.nist.gov/its90/main/.

[64] Güneş, E. private communication.

[65] Cahill, D. *Thermal conductivity data and analysis software by Prof. David G. Cahill, University of Illinois at Urbana-Champaign*. url: http://users.mrl.illinois.edu/cahill/tcdata/tcdata.html.

[66] Yang, G., Migone, A., and Johnson, K. Heat capacity and thermal diffusivity of a glass sample. *Physical Review B* 45, 1 (1992), 157. doi: 10.1103/PhysRevB.45.157.

[67] Homm, G., Piechotka, M., Kronenberger, A., Laufer, A., Gather, F., Hartung, D., Heiliger, C., Meyer, B. K., Klar, P. J., Steinmüller, S. O., and Janek, J. Thermoelectric Measurements on Sputtered ZnO/ZnS Multilayers. *Journal of Electronic Materials* 39, 9 (2010), 1504–1509. doi: 10.1007/s11664-010-1293-2.

[68] Moore, J. P., and Graves, R. S. Absolute Seebeck coefficient of platinum from 80 to 340 K and the thermal and electrical conductivities of lead from 80 to 400 K. *Journal of Applied Physics* 44, 3 (1973), 1174–1178. doi: 10.1063/1.1662324.

[69] Hartung, D. private communication.

[70] www.hpceurope.com *Datasheet: Properties of delrin 150 (polyoxymethylene)*. url: http://www.hpceurope.com/docFichesTechniques/TechnicalFilesHPCIntroduction.pdf.

[71] Lüftl, S., P. M., V., and Chandran, S. *Polyoxymethylene Handbook: Structure, Properties, Applications and their Nanocomposites.* John Wiley & Sons, 2014.

Appendix

A Solution of the heat equation for oscillating boundary conditions

In the following the one-dimensional heat-conduction equation for isotropic materials will be solved for a periodic temperature excitation on one of the boundaries. At the other boundary three different types of boundary conditions will be applied: a constant temperature, perfect thermal insulation, and the assumption of the medium being semi-infinite. The heat equation, which is a parabolic partial differential equation can be written as:

$$\frac{\partial T}{\partial t} = D\frac{\partial^2 T}{\partial x^2}. \tag{A.1}$$

An often used method to solve this type of equation is the separation of variables, also known as Fourier method. By assuming that the solution $T(x,t)$ can be written as:

$$T(x,t) = F(t) \cdot G(x), \tag{A.2}$$

the partial differential equation can be transformed into:

$$\frac{1}{F(t)}\frac{\partial F(t)}{\partial t} = \xi = \frac{D}{G(x)}\frac{\partial G(x)^2}{\partial x^2}, \tag{A.3}$$

with ξ being a constant value. Both sides can now be solved separately. The solutions for $F(t)$ and $G(x)$ are:

$$F(t) = \alpha e^{\xi t} \tag{A.4}$$

and

$$G(x) = \beta_1 e^{x\sqrt{\xi/D}} + \beta_2 e^{-x\sqrt{\xi/D}}. \tag{A.5}$$

Reinserting the solutions back into Eq. (A.2) leads to:

$$T(x,t) = \alpha e^{\xi t}\beta_1 e^{x\sqrt{\xi/D}} + \alpha e^{\xi t}\beta_2 e^{-x\sqrt{\xi/D}}. \tag{A.6}$$

The coefficients α, β_1, β_2 and ξ can now be determined using the boundary conditions. First the periodic temperature excitation at $x = 0$ is written as a Fourier series:

$$T(0,t) = \sum_{n=-N}^{N} A_n e^{in\omega t}. \tag{A.7}$$

In a first step only one single summand of the series is compared with the solution in Eq. (A.6) at $T(0,t)$:

$$A_n e^{in\omega t} = \alpha(\beta_1 + \beta_2)e^{\xi t}. \tag{A.8}$$

This leads to

$$\xi = in\omega \tag{A.9}$$

and

$$A_n = \alpha(\beta_1 + \beta_2). \tag{A.10}$$

As the heat-equation is linear the principle of superposition holds and $T(x,t)$ can be written for all n as:

$$T(x,t) = \sum_{n=-N}^{N} \frac{A_n}{\beta_1 + \beta_2} e^{in\omega t}\left[\beta_1 e^{x\sqrt{in\omega/D}} + \beta_2 e^{-x\sqrt{in\omega/D}}\right]. \tag{A.11}$$

Furthermore, the substitution $\gamma = \frac{\beta_1}{\beta_1+\beta_2}$ leads to:

$$T(x,t) = \sum_{n=-N}^{N} A_n e^{in\omega t}\left[\gamma e^{x\sqrt{in\omega/D}} + (1-\gamma)e^{-x\sqrt{in\omega/D}}\right]. \tag{A.12}$$

The boundary condition for the semi-infinite medium is given by:

$$\lim_{x\to\infty} T(x,t) = 0, \tag{A.13}$$

which leads directly to

$$\gamma = 0. \tag{A.14}$$

When the excitation temperature at $x = 0$ is chosen to be $T(0,t) = \cos(\omega t)$, the corresponding Fourier coefficients are given by:

$$A_{-1} = A_1 = \frac{1}{2}. \tag{A.15}$$

By inserting this into Eq. (A.12) one obtains finally:

$$T(x,t) = e^{-x\sqrt{\frac{\omega}{2D}}} \cos\left(\omega t - x\sqrt{\frac{\omega}{2D}}\right). \tag{A.16}$$

In the case of a medium with a finite length l and the Dirichlet boundary condition of $T(l,t) = 0$, one obtains for γ:

$$\gamma = \left(1 - e^{2l\sqrt{in\omega/D}}\right)^{-1}. \tag{A.17}$$

With the temperature excitation of $T(0,t) = \cos(\omega t)$ this leads to the following expression for the temperature distribution:

$$\begin{aligned} T(x,t) = \frac{1}{4}e^{it\omega}\left(\coth\left(l\sqrt{\frac{i\omega}{D}}\right) - 1\right)\left(e^{\sqrt{\frac{i\omega}{D}}(2l-x)} - e^{x\sqrt{\frac{i\omega}{D}}}\right) \\ + \frac{1}{4}e^{-it\omega}\left(\coth\left(l\sqrt{-\frac{i\omega}{D}}\right) - 1\right)\left(e^{\sqrt{-\frac{i\omega}{D}}(2l-x)} - e^{x\sqrt{-\frac{i\omega}{D}}}\right). \end{aligned} \tag{A.18}$$

For medium of finite length l and perfect isolation at the boundary $x = l$ the temperature gradient at the boundary has to be zero:

$$\frac{\partial T}{\partial x}\Big|_{x=l} = 0. \tag{A.19}$$

This leads to the following condition for γ:

$$\gamma = \left(1 + e^{2l\sqrt{in\omega/D}}\right)^{-1}. \tag{A.20}$$

By inserting this into Eq. (A.11) and using the excitation of $T(0,t) = \cos(\omega t)$ again, one obtains:

$$\begin{aligned} T(x,t) = -\frac{1}{2}e^{it\omega}\mathrm{sech}\left(l\sqrt{\frac{i\omega}{D}}\right)\sinh\left(\sqrt{\frac{i\omega}{D}}(l-z)\right) \\ -\frac{1}{2}e^{-it\omega}\mathrm{sech}\left(l\sqrt{-\frac{i\omega}{D}}\right)\sinh\left(\sqrt{-\frac{i\omega}{D}}(l-z)\right). \end{aligned} \tag{A.21}$$

B Parameters used in the numerical simulations

parameter	value
κ_{sensor}	$2\,\mathrm{W\,m^{-1}\,K^{-1}}$
κ_{sample}	$1\,\mathrm{W\,m^{-1}\,K^{-1}}$
$c\rho_{\text{sensor}}$	$2\,\mathrm{MJ\,K^{-1}\,m^{-3}}$
$c\rho_{\text{sample}}$	$2\,\mathrm{MJ\,K^{-1}\,m^{-3}}$
sensor length	$10\,\mathrm{mm}$
sample length	$10\,\mathrm{mm}$
sensor radius	$6\,\mathrm{mm}$
sample radius	$6\,\mathrm{mm}$
timeframe	$10,000\,\mathrm{s}$

Table B.1: Simulation parameters used in the Comsol simulations unless stated otherwise in the corresponding section.

List of publications

[1] Homm, G., Piechotka, M., Kronenberger, A., Laufer, A., Gather, F., Hartung, D., Heiliger, C., Meyer, B. K., Klar, P. J., Steinmüller, S. O., et al. Thermoelectric Measurements on Sputtered ZnO/ZnS Multilayers. *Journal of electronic materials* 39, 9 (2010), 1504–1509.

[2] Gather, F., Heiliger, C., and Klar, P. J. Modeling of interface roughness in thermoelectric composite materials. *Journal of Physics: Condensed Matter* 23, 33 (2011), 335301.

[3] Gather, F., Heiliger, C., and Klar, P. J. NeMo: A network model program for analyzing the thermoelectric properties of meso and nanostructured composite materials. *Progress in Solid State Chemistry* 39, 3 (2011), 97–107.

[4] Homm, G., Petznick, S., Gather, F., Henning, T., Heiliger, C., Meyer, B. K., and Klar, P. J. Effect of interface regions on the thermoelectric properties of alternating ZnO/ZnO: Al stripe structures. *Journal of electronic materials* 40, 5 (2011), 801–806.

[5] Hartung, D., Gather, F., and Klar, P. J. Comparison of different methods for measuring thermal conductivities. In: *9TH EUROPEAN CONFERENCE ON THERMOELECTRICS: ECT2011*. Vol. 1449. 1. AIP Publishing. 2012, 381–384.

[6] Homm, G., Gather, F., Kronenberger, A., Becker, M., Meyer, B. K., Klar, P. J., Ziolkowski, P., and Müller, E. Correlation of local and global thermoelectric properties in laterally structured thermoelectric materials. In: *9TH EUROPEAN CONFERENCE ON THERMOELECTRICS: ECT2011*. Vol. 1449. 1. AIP Publishing. 2012, 389–392.

[7] Gather, F., Kronenberger, A., Hartung, D., Becker, M., Polity, A., Klar, P. J., and Meyer, B. K. Possibility of enhancing the thermoelectric figure of merit of ZnO by sulfur incorporation. *Applied Physics Letters* 103, 8 (2013), 082115.

[8] Homm, G., Gather, F., Kronenberger, A., Petznick, S., Henning, T., Eickhoff, M., Meyer, B. K., Heiliger, C., and Klar, P. J. Effects of interface geometry on the thermoelectric properties of laterally microstructured ZnO-based thin films. *physica status solidi (a)* 210, 1 (2013), 119–124.

Danksagung

Ich möchte allen Personen danken, die bei der Erstellung dieser Arbeit mitgewirkt haben. Ein besonderer Dank geht an:

- meinen Betreuer Prof. Dr. Peter Klar, in dessen Arbeitsgruppe ich bereits seit meiner Bachelorarbeit tätig war und der mich in das Themengebiet der Thermoelektrik gebracht hat, insbesondere auch für die Geduld bei der kritischen Auseinandersetzung mit dieser Arbeit,
- Prof. Dr. Wolf-Eckhard Müller, für das Schreiben des Gutachtens und für die Thermoelektrikvorlesung, bei der viele interessante und auch nützliche Dinge vermittelt wurden,
- die (ehemaligen) Thermoelektriker der Arbeitsgruppe Klar, insbesondere Gert Homm, David Hartung und Tobias Lind, für die tolle Zusammenarbeit,
- Andreas Rühl für das unermüdliche Korrekturlesen,
- Ekrem Güneş für die Hilfe bei der Planung des Aufbaus,
- meine Bürokollegen Sabrina Darmawi, Christian Reindl und Florian Kuhl für die gute Stimmung im Büro,
- Markus Piechotka und Martin Fischer für die vielen Gespräche, bei denen oft gute Ideen heraussprangen,
- die gesamte Arbeitsgruppe Klar für die schöne Zeit.

Besonders danken möchte ich auch meiner Familie, die mich während meines gesamten Studiums unterstützt hat, und meiner Frau Hanna und meinem Sohn Benjamin dafür, dass Sie mir immer wieder gezeigt haben, was wirklich wichtig im Leben ist.

Erklärung

Ich erkläre: Ich habe die vorgelegte Dissertation selbständig und ohne unerlaubte fremde Hilfe und nur mit den Hilfen angefertigt, die ich in der Dissertation angegeben habe. Alle Textstellen, die wörtlich oder sinngemäß aus veröffentlichten Schriften entnommen sind, und alle Angaben, die auf mündlichen Auskünften beruhen, sind als solche kenntlich gemacht. Bei den von mir durchgeführten und in der Dissertation erwähnten Untersuchungen habe ich die Grundsätze guter wissenschaftlicher Praxis, wie sie in der „Satzung der Justus-Liebig-Universität Gießen zur Sicherung guter wissenschaftlicher Praxis“ niedergelegt sind, eingehalten.

Moosinning, im Mai 2015 Florian Gather